CONF-7810113--1

MASTER

SOME ASPECTS OF HEAVY-ION SCATTERING*

G. R. Satchler**

Oak Ridge National Laboratory†
Oak Ridge, TN 37830 U.S.A.

NOTICE
This report was prepared as an account of work sponsored by the United States Government. Neither the United States nor the United States Department of Energy, nor any of their employees, nor any of their contractors, subcontractors, or their employees, makes any warranty, express or implied, or assumes any legal liability or responsibility for the accuracy, completeness or usefulness of any information, apparatus, product or process disclosed, or represents that its use would not infringe privately owned rights.

DISTRIBUTION OF THIS DOCUMENT IS UNLIMITED

*Lectures to be presented to the Sixth INS Summer School on Nuclear Physics, Dogashima, Japan, Oct. 30 - Nov. 2, 1978.

**Supported by a Research Fellowship of the Japan Society for the Promotion of Science.

†Research sponsored by the Division of Physical Research, U.S. Department of Energy, under contract W-7405-eng-26 with the Union Carbide Corporation.

By acceptance of this article, the publisher or recipient acknowledges the U.S. Government's right to retain a non-exclusive, royalty-free license in and to any copyright covering the article.

Some Aspects of Heavy-Ion Scattering

G. R. Satchler

Table of Contents

1. Introduction
   1.1. Characteristics of heavy-ion scattering
   1.2. Semi-classical descriptions
   1.3. Strong absorption
   1.4. Parameterized S-matrices
   1.5. Typical angular distributions
   1.6. Rainbow or Fresnel?
   1.7. What do we learn from heavy-ion scattering?
      1.7.1. Strong absorption radii
      1.7.2. The nucleus-nucleus potential

2. Nucleus-Nucleus Optical Potentials
   2.1. Definition
   2.2. Relation to other potentials
   2.3. Proximity potentials
   2.4. Fusion barrier

3. Deep or Shallow Potentials?
   3.1. Light systems
   3.2. The system $^{16}O + ^{28}Si$
   3.3. Barrier penetration and reflection; $\alpha + ^{40}Ca$
   3.4. The systems $^{12}C + ^{12}C$ and $^{6}Li + ^{40}Ca$
   3.5. Summary

4. Folded Potentials for Heavy- (and Light-) Ion Scattering
   4.1. Definition of folded potentials
   4.2. Single-folded potentials
   4.3. The interaction v
      4.3.1. Effective interactions
      4.3.2. Spin- and isospin-dependence
      4.3.3. Rôle of the long-range OPEP
      4.3.4. The M3Y interaction

4.4. Exchange

4.5. Nuclear densities

4.6. Applications to scattering data

4.6.1. Nucleons

4.6.2. Alphas

4.6.3. The Li ions

4.6.4. Heavier ions

4.7. Summary

Appendix: Barrier Penetration and Reflection Effects

References

Table 1

Figure Captions

SOME ASPECTS OF HEAVY-ION SCATTERING*

G. R. Satchler**

Oak Ridge National Laboratory†
Oak Ridge, TN 37830 U.S.A.

*Lectures to be presented to the Sixth INS Summer School on Nuclear Physics, Dogashima, Japan, Oct. 30 - Nov. 2, 1978.

**Supported by a Research Fellowship of the Japan Society for the Promotion of Science.

†Research sponsored by the Division of Physical Research, U.S. Department of Energy, under contract W-7405-eng-26 with the Union Carbide Corporation.

1. Introduction

1.1. Characteristics of heavy-ion scattering

We shall be concerned here with the elastic (or quasi-elastic) scattering of two heavy ions at low or medium energies (mainly projectiles with $\lesssim$ 20 MeV per nucleon). Normally, the term 'heavy ion' means a composite nucleus of mass A > 4. However for our purpose, it is convenient to include alpha particles also since in many respects the scattering of alphas resembles that of heavier nuclei, both of them exhibiting strong absorption. (Often, also, more complete data are available for alpha scattering.)

Heavy-ion scattering is distinguished by (a) short wavelengths, (b) strong Coulomb interactions and (c) strong absorption. The wavelengths are short because of the large masses and because of the high energies usually required to surmount the large Coulomb repulsions. Two nuclei, with mass numbers A_1 and A_2 and center-of-mass energy E_{cm}(MeV), have a reduced wavelength of

$$\lambda\!\!\!^{-} \equiv \frac{\lambda}{2\pi} \equiv \frac{1}{k} \approx \sqrt{\frac{21\ (A_1+A_2)}{A_1 A_2\ E_{cm}}}\ \text{fm}. \tag{1}$$

For ^{16}O on ^{208}Pb with E_{lab} = 150 MeV this gives $\lambda\!\!\!^{-}$ = 0.10 fm, while for ^{136}Xe on ^{209}Bi with E_{lab} = 1130 MeV we have $\lambda\!\!\!^{-}$ = 0.019 fm. (Note that these are quite 'low' energies, less than 10 MeV per projectile nucleon.) These wavelengths remain short even when we take the Coulomb repulsion into account. When the nuclear centers are separated by $r_o(A_1^{1/3} + A_2^{1/3})$ fm, the Coulomb barrier is

$$U_c \approx \frac{1.44\ Z_1 Z_2}{r_o\ (A_1^{1/3} + A_2^{1/3})}\ \text{MeV}. \tag{2}$$

With r_o = 1.4 fm, this repulsion only increases the values of $\lambda\!\!\!^{-}$ to 0.15 fm and 0.031 fm, respectively, in the two cases just cited.

These small values of $\lambda\!\!\!^{-}$ (large values of k) also imply that large angular momenta L are involved. Typically, we need partial waves up to and somewhat beyond the grazing value

$$L_{gr} \approx k\ (R_1 + R_2) = kr_o\ (A_1^{1/3} + A_2^{1/3}); \tag{3}$$

e.g. for the $^{136}Xe + ^{209}Bi$ case we have $L_{gr} \approx 500$ if $r_o = 1.4$ fm. This means that calculations using partial-wave expansions will often be time consuming since they will involve evaluating many terms.

There are several approaches to describing and understanding this scattering and we briefly review them.

1.2. Semiclassical descriptions

The first two properties (a) and (b) mentioned above suggest the use of classical mechanics or the developments known as semi-classical theories [1,2]* which take into account such quantal effects as the superposition and interference of contributions from different classical trajectories. The basic idea here is that $\lambda\!\!\!^{-}$ is small compared to other dimensions in the problem such as the sizes of the nuclei and distances over which the interaction potential changes significantly. Then locally at some position x where the potential is U(x), we can approximate the wavefunction of relative motion by a plane wave with a wavelength determined by the local kinetic energy,

$$\psi(x) \approx e^{ik(x)x}$$

with

$$k(x) = \sqrt{2\mu[E-U(x)]/\hbar^2}. \tag{4}$$

This leads to the WKB approximation which is the basis of theories which reduce a full quantal (wave) treatment to one of geometrical or ray optics. The partial wave sum is converted into an integral and the saddle point or stationary phase approximation is used to evaluate the scattering amplitude. This amplitude then appears as a coherent superposition of the contributions from all the classical orbits which result in the same scattering angle. In this way we take into account the refractive effects due to the nuclear potential acting between the two nuclei, as well as the resulting interference effects which are essential quantal corrections.

We note that we have only referred to the relative motion of the two nuclei. This is sufficient to determine the elastic scattering, but it does imply that the full many-body problem of two interacting composite nuclei has

*Rather than attempt a complete bibliography, I refer mostly to recent papers which include references to earlier work.

been replaced by a two-body problem by the introduction of an effective or 'optical' potential. This potential depends only upon the separation of the two nuclei (together with, in a few cases, some simple collective variables such as shape deformations) but does not refer explicitly to the many internal degrees of freedom. The presence of these other degrees of freedom means that the nuclei can be internally excited. In fact, this is by far the most likely event when two composite nuclei make 'contact'. Since this removes flux from the elastic channel being considered, it is equivalent to absorption in this channel. In potential terms this is represented by an imaginary potential. Heavy ions (and alphas) are characterised by strong absorption; that is to say, the scattering matrix elements S_L are approximately zero for small angular momenta $L \lesssim k(R_1 + R_2)$ and contribute essentially no outgoing, scattered waves.

1.3. Strong absorption

This property, namely strong absorption, introduces complications for semiclassical theories. Weak absorption could be taken into account in a perturbative way, essentially by a damping of the amplitude as the system progresses along its classical path. However, strong absorption introduces essentially quantal (i.e. wave) effects such as diffraction (by which is meant the propagation of waves into classically forbidden or shadow regions). One response to this problem has been to generalize the semiclassical theories [3-6] to include complex trajectories, with complex angular momenta and complex turning points. The use of a complex angular momentum, for example, may be thought of as a way of replacing a single (real) angular momentum L associated with a given orbit by a packet of angular momenta centered on L but with a width given by the imaginary part of the angular momentum. This spreading is introduced by diffraction at the edge of the 'black', absorptive region. These matters have been discussed in detail elsewhere [3-6]. Unfortunately, the need to use these complex quantities somewhat obscures the physical insight which could be obtained in cases of weak absorption with the descriptions based upon real orbits.

1.4. Parameterized S-matrices

An alternative approach [7,8] makes use of the simple structure of the scattering or S-matrix elements for strongly absorbing systems and parametrizes it directly. The crudest version of this is the sharp cut-off model,

$$S_L = 0 \quad , \quad L < L_c ,$$
$$S_L = 1 \quad , \quad L > L_c , \tag{5}$$

where $L_c \approx k(R_1 + R_2)$ is a critical angular momentum corresponding to a peripheral or grazing collision. This was generalized to functional forms of S(L) with smooth cut-offs, and a nuclear phase-shift was also introduced. Such forms are either phenomenological or, more recently [9], have been related to particular assumptions about the nuclear potential. Closed forms have been obtained for the partial-wave sums and the wave optics implied have been examined in detail. In certain limits, the results can be reduced to Fresnel and Fraunhofer diffraction scattering.

We note that, in general, this approach does not involve any assumptions about reducing a complicated many-body problem to an equivalent two-body one by the introduction of an effective or optical (complex) potential. It simply makes use of simple, plausible, properties of an S-matrix for strongly absorbing scattering which involves many partial waves. Herein lies both its strength and its 'weakness'. It is able to correlate large amounts of (elastic and inelastic) data. Indeed, even what I chose to call its 'weakness' is overcome by recent work [9] which rather directly relates the S-matrix behaviour to an underlying interaction potential.

1.5. Typical angular distributions

Figure 1 shows some 'typical' angular distributions for strong absorption scattering. Figure 1(a) shows a diffraction-like structure [10] which is usually referred to as Fraunhofer diffraction. This occurs for energies well above the Coulomb barrier (which is only about 10 MeV for the case shown). On the other hand, at energies closer to the Coulomb barrier, we see patterns like Fig. 1(b) [11] where, after some oscillation about the Rutherford value, the ratio of the cross section to the Rutherford value falls roughly exponentially (by four orders of magnitude in the case shown). This is referred to variously as Fresnel or (Coulomb) rainbow scattering depending upon the author's point of view (see below).

Figure 1(c) shows results [12] for 140 MeV alphas scattering from various targets. The forward angles show (after the initial 'Coulomb rainbow') the 'Fraunhofer' diffraction pattern, customary for strongly absorbed particles, whose oscillations have a period

$$\Delta\theta \approx \frac{\pi}{L_{gr}} \approx \frac{\pi}{k(R_1 + R_2)} \tag{6}$$

which is characteristic of peripheral scattering. Howe er, at larger angles, this pattern is damped out and then followed by a smooth, exponential-like fall-off. This 'shadow' has been interpreted [13] in terms of a further refractive effect which has been called a 'nuclear rainbow'. We return to this phenomena later, but we note that the rainbow explanation is an example of something that may be readily and intuitively understood in classical terms but which is much less clear in the language of partial waves (since many partial waves may be involved in a correlated way). Such a nuclear rainbow has not yet been identified for the scattering of heavier ions; (although the data shown in Fig. 1(a) might appear to suggest the onset of such a rainbow for $\theta \gtrsim 50°$, it seems in fact that the absorption in this case is still too strong for it to be fully developed). Although the alpha-nucleus interaction is characterised by 'strong absorption', it appears that it is not quite as complete in some respects as for the heavier ions.

1.6. Rainbow or Fresnel?

The differential cross sections shown in Fig. 1(b) are typical of heavy-ion scattering which is dominated by the Coulomb field, namely some oscillation about the Rutherford value followed by a shadow, a rapid decrease in cross section. One question that does not seem to be completely resolved is whether such a pattern is due to the refractive effects of the real nuclear potential (i.e., whether it should be called rainbow scattering) or whether it is diffractive (i.e., whether it should be called Fresnel scattering) due to the sudden onset of strong absorption at the nuclear surface. The refractive interpretation [4] says that the Coulomb orbits that would have been scattered into the shadow region encounter the attractive (real) nuclear potential and are pulled forward. A concentration of such rays results in a rainbow peak which is identified with the largest and last rise above the Rutherford value and has been called "the Coulomb rainbow". The diffractive interpretation [7,8] implies that the would-be rainbow orbits encounter strong absorption and thus the rainbow effect is strongly damped or completely absent. Rather, the shadow is due to absorption of the particles on the Coulomb orbits which would have scattered into this region and the peak structure is due to Fresnel diffraction at the edge of the black, absorbing sphere.

It is very unlikely that these two processes could be directly distinguished experimentally [6]. Indeed, it is possible that neither extreme interpretation is appropriate [6]. It certainly is true that in practical cases the cross section in the vicinity of the 'Fresnel' peak is sensitive to the real nuclear potential and hence to refractive effects, even though that potential is typically of order -1 MeV and very much less than the Coulomb potential in the same region. The observed angular distributions cannot be reproduced by a purely imaginary (absorptive) potential. Indeed the magnitude of the oscillations about the Rutherford cross section is a sensitive indicator of the relative strengths of the real and imaginary potentials at the surface, indicating that both absorptive and refractive processes play important rôles. (Typically, the ratio of imaginary to real potential ranges from $\sim \frac{1}{3}$ at low energies increasing to unity as the energy increases.) First, we see from Fig. 1(b) that the imaginary potential alone does not produce enough 'shadow'; the attractive real potential is necessary to pull the peripheral orbits into the absorptive region. (This interpretation is justified by examining the corresponding scattering matrix elements.) Further, on the one hand Fig. 2(a) shows [10] that the magnitude of the oscillation about the Rutherford value is sensitive to the amount of absorption (for a fixed real, refractive, potential) while, on the other hand, Fig. 2(b) shows [14] that these oscillations are not independent of the strength of the real potential (for a fixed imaginary, absorptive, potential). Consequently, it appears that the detailed shape of this kind of scattering pattern is dependent upon both absorptive (diffractive) and refractive effects.

For convenience, we shall continue to refer to this kind of scattering pattern as 'Fresnel'-like.

1.7. What do we learn from heavy-ion scattering?

1.7.1. Strong absorption radii

Some brief remarks on the physical quantities about which we may obtain information from heavy-ion scattering. First, of course, we learn something about the appropriate 'size' of the two interacting nuclei. This appears in the form of some strong absorption radius, R_{SA}, which characterises the separation of the two nuclear centers when they begin to interact strongly. There is not a unique definition of this distance, although the

different prescriptions in use give values which differ usually by only a few times 0.1 fm. The simplest and most empirical is the quarter-point prescription, based upon Fresnel diffraction ideas, which is applicable to angular distributions like those shown in Fig. 1(b). Here R_{SA} is taken to be the distance of closest approach, $D_{1/4}$ say, of that Rutherford orbit whose scattering angle equals the angle $\theta_{1/4}$ at which the measured cross section has fallen to $\frac{1}{4}$ of the Rutherford value, $d\sigma(\theta_{1/4})/d\sigma_R = \frac{1}{4}$. This may be converted to a reaction or absorption cross section σ_A by assuming complete absorption for all orbits which approach more closely than $D_{1/4}$ and no absorption for the others [15]. Let L be the angular momentum quantum number corresponding to a distance of closest approach D and scattering angle θ (so that the actual angular momentum is $(L + \frac{1}{2})\hbar$, semiclassically). These are related for Rutherford orbits by

$$(L + \tfrac{1}{2}) = n \cot(\tfrac{1}{2}\theta)$$

or

$$(L + \tfrac{1}{2}) = k\, D\, (kD-2n), \tag{7}$$

where k is the wavenumber and n is the Sommerfeld or Coulomb parameter,

$$n \approx 0.16\, Z_1 Z_2 \sqrt{\frac{A_1}{E_{lab}(\mathrm{MeV})}} \tag{8}$$

if A_1 is the projectile mass number. Then the absorption cross section is given by

$$\sigma_A \approx \pi k^2 \sum_{L=0}^{L_{1/4}} (2L+1) = \pi k^2 (L_{1/4}+1)^2, \tag{9}$$

if $L = L_{1/4}$ corresponds to $\theta = \theta_{1/4}$, etc. This procedure has been useful for deducing qualitatively reliable values (to $\lesssim$ 20%, say) of σ_A from elastic scattering measurements, although the accuracy in any given case may be difficult to assess without further work.

The parameterized S-matrix and optical model approaches may be used to analyse elastic scattering data of either the 'Fresnel' or 'Fraunhofer' type and automatically give a complete S-matrix which allows a precise prediction for σ_A (within the accuracy of the data and of the fit to it). However, there is not complete agreement on what is the most useful quantity to

designate as the strong absorption radius. A popular prescription is to take for R_{SA} the distance of closest approach $D_{1/2}$ of the Rutherford orbit with that angular momentum $L_{1/2}$ for which the analysis indicates a 50% probability of absorption, or a transmission (or penetration) coefficient

$$T_{L_{1/2}} = 1 - \left|S_{L_{1/2}}\right|^2 = \tfrac{1}{2}, \tag{10}$$

so that

$$\left|S_{L_{1/2}}\right| = \sqrt{\tfrac{1}{2}}.$$

The value of $D_{1/2}$ is obtained from $L_{1/2}$ through the classical relation (7) above. Another popular choice [8] is to take the L value for which $|S_L| = \frac{1}{2}$ while more recently reasons have been given [9] for choosing the L for which $d|S_L|/dL$ has its maximum. The latter prescription generally results in slighter smaller values of L, but all the choices give radii R_{SA} which are fairly close. (We have to remember that, although it has considerable intuitive value, R_{SA} does not have any absolute significance except within the context of some theoretical framework.) Further, those who favour a refractive interpretation rather than one based upon Fresnel diffraction emphasise the distance of closest approach of the 'rainbow orbit' [16]. Again, one arrives at critical radii with values rather similar to the values of R_{SA} obtained in the other ways.

Typically, the values of R_{SA} obtained are given approximately by

$$R_{SA} \approx 1.5\ (A_1^{1/3} + A_2^{1/3})\ \text{fm}. \tag{11}$$

Physically, the variation is perhaps better represented by [15]

$$R_{SA} \approx 1.1\ (A_1^{1/3} + A_2^{1/3}) + 3\ \text{fm}, \tag{12}$$

which represents a roughly constant separation between the half-density points of the density distributions of the two nuclei. A collection of values of critical radii based upon rainbow scattering ideas has been published [16] and follows these trends also.

These values of R_{SA} are <u>large</u>. The half-density points of the two nuclei are separated by roughly 3 fm. This corresponds to a very small overlap of the two density distributions (see Fig. 3). Typically, the two densities

overlap at a point where they are between 5 and 10% of their central values.

1.7.2. The nucleus-nucleus potential

One of the quantities of most interest that we might hope to extract from elastic scattering measurements is the potential of interaction between the two nuclei. This is usually expressed in terms of a complex effective or optical potential U(r), depending only upon the separation r of their centers-of-mass; we return to this later.

Learning about this interaction potential is of fundamental importance. It enters into the description of any heavy-ion collision. It embodies the initial reaction of the two nuclei to each other as they approach. It is needed, for example, in descriptions (such as DWBA and coupled-channels) of direct, peripheral reactions. Elastic scattering is also a doorway through which the system must go before proceeding to deep inelastic scattering. Further, this potential is a quantity of interest in itself which we may attempt to understand from more basic principles. (The folded potential to be discussed later is one such attempt.)

In practice, we find that in most cases the observed scattering determines the potential only in the surface or extreme tail. Typically, the values of the real and imaginary parts of the potential U are determined, often quite accurately, in the vicinity of the strong absorption radius. In particular, the ratio of imaginary to real (i.e., the 'phase' of the potential) can be determined with some precision with data like those shown in Fig. 2. For many systems with ~ 10 MeV per nucleon bombarding energy, this ratio is found to be close to unity, but it appears to be smaller as the energy is reduced and approaches the Coulomb barrier. The value of the real nuclear potential near the strong absorption radius is typically of order -1 MeV, which is much less than the repulsive Coulomb potential in the same region.

Further, with data that are reasonably precise and complete, constraints can be put upon the values of the slopes Re dU/dr and Im dU/dr in the same region. For example, the data of Fig. 1(b) were shown [10] to place a lower limit on Re dU/dr (which ruled out a certain kind of folded potential). In many cases of Fresnel-like scattering such as Fig. 1(b) it is possible to use Re U and Im U with the same slope in the surface (e.g., a Woods-Saxon potential with $a_R = a_I$). However, in other cases improvements in fit can be obtained with different slopes; the tendency is for $|\mathrm{Im}\ dU/dr| > |\mathrm{Re}\ dU/dr|$.

At higher energies, when Fraunhofer characteristics are becoming manifest, it is seldom adequate to have Re U and Im U with the same shape (unless the data available to be fitted are very limited in angle).

The real potentials obtained from a considerable number of analyses of elastic heavy-ion scattering have been summarized by Christensen and Winther [16] in terms of an exponential potential (appropriate for the surface region of $r \sim R_{SA}$),

$$\mathrm{Re}\ U_N(r) = -\ 50\ \frac{R_1 R_2}{R_1+R_2}\ e^{-\left(\frac{r-R_1-R_2}{\alpha}\right)}\ \mathrm{MeV} \tag{13}$$

where $$R_i = 1.233\ A_i^{1/3} - 0.978\ A_i^{-1/3}\ \mathrm{fm}$$

and $\alpha = 0.63$ fm. This gives a good account of the average behaviour of potentials which fit observed scattering, although minor fluctuations in the values will be found in individual cases.

In almost all cases of heavy-ion scattering, the fits to the data are very (or completely) insensitive to the potential at separations smaller than the strong absorption radius; compare Figs. 1(b) and 3(b), for example. (This is true also for alpha scattering at 'lower' energies and/or when the angular range is limited to forward scattering. However, data such as those shown in Fig. 1(c) are indeed sensitive to the potential over a wider range of radii, sufficiently so that one may determine unambiguously the parameters of a particular model potential such as the Woods-Saxon one or even deduce evidence for different shapes of potential, such as the square of a Woods-Saxon one [11,13,17].) Partial exceptions occur for heavy ions at higher energies, when in some cases at least it appears that the scattering is sensitive to the potential over a range of distances which may extend inside the strong absorption radius. Even here, ambiguities may exist [18].

There are a few cases, which appear to be quite exceptional, where the scattering may be sensitive to the potential U(r) for quite small separations, $r \simeq 0$. This enables us to raise the question "deep or shallow potentials?". We return to this later.

When the scattering is sensitive only to the potential in the surface, there are severe 'ambiguities' in the potential that can be extracted from the data. A very well-known one is the Igo ambiguity. This may be expressed

in terms of the Woods-Saxon potential,

$$\mathrm{Re}\ U = -\frac{V}{1+\exp\left(\frac{r-R_R}{a_R}\right)}, \quad \mathrm{Im}\ U = -\frac{W}{1+\exp\left(\frac{r-R_I}{a_I}\right)}. \tag{14}$$

At 'large' distances like $r \approx R_{SA}$, this becomes

$$\mathrm{Re}\ U \approx -\left(Ve\frac{R_R}{a_R}\right) e^{-\frac{r}{a_R}}, \quad \mathrm{Im}\ U \approx -\left(We\frac{R_I}{a_I}\right) e^{-\frac{r}{a_I}}. \tag{15}$$

Clearly, if a_R, a_I are fixed, any combinations of V and R_R, and W and R_I, which keep the combinations $\left(V \exp \frac{R_R}{a_R}\right)$ and $\left(W \exp \frac{R_I}{a_I}\right)$ constant will give the same scattering. Indeed, in this situation the parameters V and R_R, for example, have no separate significance. Exploring this ambiguity is a pointless exercise. Far better, for example, to simply quote the values of U (and dU/dr if they can be determined) at some suitable strong absorption radius. (Since it is often convenient to use the Woods-Saxon form, one may fix either V or R_R and either W or R_I at some reasonable value.)

Often the slopes dU/dr are not precisely determined; potentials U with somewhat different slopes (different values of 'a' in a Woods-Saxon parameterization) may give equally good fits to the data. But then it is usually found that these potentials will all cross at almost the same radius ([19]; see also [20] for recent examples); this radius will be found to be close to the strong absorption radii defined earlier. Then the data may be said to have determined the potential at this radius.

Finally, a word of caution. Since such ambiguities exist, it is very misleading when fitting data to vary more parameters than the data are capable of determining. Only too often, independent values of all six Woods-Saxon parameters are quoted as being 'derived' from fitting the data when in fact only, say, four are required (such as the values of Re U, Im U and their slopes at the strong absorption radius. Indeed, if different slopes are not required, only 3 quantities are determined). This entails fixing two or more of the parameters at reasonable values, as suggested above. Such a procedure not only avoids redundancies, it also makes it much easier to compare results for different energies or different targets. (Another way of attempting to

avoid redundancies is to use theoretically pre-determined forms such as the proximity potential [21] or the folding models [19] discussed later.)

2. Nucleus-Nucleus Optical Potentials

Potentials appropriate for the elastic scattering of two heavy ions have been discussed by various authors (see, for example, Schroder and Huizenga [15], Brink [22] DeVries [23] and Mosel [70], where other references may be found).

2.1. Definition

We have spoken so far as though the inter-nucleus potential was defined uniquely. This is not so; there are various ways in which we may reduce the complicated $(A_1 + A_2)$-body scattering problem to an effective two-body problem. Failure to remember this has sometimes led to confusion. A conventional optical model potential U(R) for two nuclei A_1, A_2 is one which appears in a one-body Schrödinger equation

$$\left[- \frac{\hbar^2}{2\mu_\alpha} \nabla^2 + U(R) \right] X(\underset{\sim}{R}) = E\, X(\underset{\sim}{R}), \tag{16}$$

where μ_α is the reduced mass of the pair, $\underset{\sim}{R}$ is the separation of their centers of mass and E is the CMS energy of relative motion. The solution $X(\underset{\sim}{R})$ with the appropriate boundary conditions describes the elastic scattering of $A_1 + A_2$. Usually U(R) is assumed to be local (although its parameter values may vary with bombarding energy) and to have a smooth, simple functional form, like that of the Woods-Saxon shape (14). Occasionally some L-dependence is introduced, but only if one is forced to consider such a generalization by some intractable data. The primary consideration is simplicity.

How do we justify the use of an equation like Eq. (16) which makes no reference to the many internal degrees of freedom and the corresponding non-elastic channels? One standard way to make it plausible that such an equation may adequately describe elastic scattering is to use the projection operator formalism of Feshbach [24].

Suppose that the complete Hamiltonian for the colliding pair is given by

$$H = H_1 + H_2 + T + V \tag{17}$$

where H_1 and H_2 denote the internal Hamiltonians for the isolated nuclei, T is the kinetic energy of relative motion in the center-of-mass system and V is the coupling interaction between the ions. At this point, we ignore any explicit reference to antisymmetrization between nucleons in different ions, although we assume that the wavefunctions for the internal states of the individual nuclei are antisymmetric. We denote a complete set of states for the internal Hamiltonians of nuclei A_1 and A_2 by ψ_i and ϕ_j respectively, where

$$(H_1 - \varepsilon_{1i})\ \psi_i = 0, \qquad (H_2 - \varepsilon_{2j})\ \phi_j = 0. \tag{18}$$

If the complete wavefunction is denoted by $\Psi^{(+)}$, we note that measurements of elastic or inelastic scattering provide us with information about the projection of the complete wavefunction onto the channel subspace defined by the particular measurement. We denote these $\underset{\sim}{R}$-dependent projections (amplitudes) by

$$\chi_{ij}(\underset{\sim}{R}) \equiv \langle\psi_i\phi_j|\Psi^{(+)}\rangle, \tag{19}$$

which means that we can express the total wavefunction as

$$\Psi^{(+)} = \sum_{i,j} \chi_{ij}(\underset{\sim}{R})\psi_i\phi_j. \tag{20}$$

A set of coupled equations governing the $\chi_{ij}(\underset{\sim}{R})$ can be found by inserting the above expansion into the complete Schrödinger equation

$$(H-E)\ \Psi^{(+)} = 0. \tag{21}$$

This yields

$$[T + (\psi_i\phi_j|V|\psi_i\phi_j) - E_{ij}]\ \chi_{ij}(\underset{\sim}{R}) = -\sum_{[k,\ell\neq i,j]} (\psi_i\phi_j|V|\psi_k\phi_\ell)\ \chi_{k\ell}(\underset{\sim}{R}). \tag{22}$$

$$\text{where} \quad E_{ij} = E - \varepsilon_{1i} - \varepsilon_{2j} \quad \text{and} \quad (i,j=0\ldots\infty).$$

The rounded brackets denote integration over the internal coordinates of the two nuclei and serve to remind us that the matrix elements remain a function of $\underset{\sim}{R}$.

Now Eqs. (22) represent an infinite set of coupled equations which, although complete, are not very useful. Practical calculations require a severe truncation of these to a small set of equations coupling a few states of

particular interest. The use of an equation like Eq. (16) in fact involves truncation to just that one associated with the ground states, $i = j = 0$. The price we pay for this is that the interaction V becomes replaced by an effective interaction. This becomes clear in Feshbach's formalism [24] in which all explicit couplings to channels other than the one of interest are eliminated. For that channel in which both nuclei remain in their ground states this procedure results in a one-body Schrödinger equation for the $\chi_{oo}(\underset{\sim}{R})$,

$$[T + U_{op} - E]\, \chi_{oo} = 0 \tag{23}$$

with the optical potential operator U_{op} given by

$$U_{op} = (\psi_o\phi_o|V|\psi_o\phi_o) + (\psi_o\phi_o|VQ\,\frac{1}{E-H_{QQ}+i\varepsilon}\,QV|\psi_o\phi_o) \tag{24}$$

$$= U_F + \Delta U.$$

U_F is defined as the first term in Eq. (24)

$$U_F = (\psi_o\phi_o|V|\psi_o\phi_o), \tag{25}$$

and is called the folded potential for elastic scattering. (Note that this same folded potential and its generalization to excited states and off-diagonal couplings also appears in Eqs. (22).) Q is the operator which projects off the ground states of the two nuclei. By its construction, the exact elastic scattering amplitude may be obtained from χ_{oo} as $R \to \infty$.

The folded potential U_F is real (provided that V is real). The remaining term ΔU, which we may refer to as a dynamic polarization potential, arises from coupling to all the other states, is much more difficult to calculate, and, in general, is complex, non-local, energy- and angular-momentum dependent. (In practice, because of the strong short-range repulsion in the bare nucleon-nucleon interaction, the V itself will be an effective interaction or G-matrix which itself includes some 'polarization' corrections, primarily those associated with the short-range correlation between the interacting nucleons.)

In phenomenological approaches it is this object U_{op} which is approximated by a local, complex model potential U(R), for example of the

Woods-Saxon form, as in Eq. (16). However, although this formalism provides us with the form of the optical model Eq. (16), it does not guarantee that any given simple representation of U_{op} will be adequate. This question may be explored both empirically (is a given model successful in fitting data?) and by studying the structure of ΔU. For example, we know that in many cases a non-local potential may be replaced by a local one that is equivalent to it in some specified sense.

2.2. Relation to other potentials

A particular point that I wish to stress is that with the potential U_{op} (and by implication an equivalent model potential U) defined in this way, the solution $X(R)$ of Eq. (16) represents $X_{oo}(R)$ of Eqs. (22), (23) and describes the relative motion of the two nuclei while they both remain in their respective ground states. This may be a very small component of the total wavefunction in that region of space where the two nuclei overlap appreciably; in that case, the strong absorption into other channels manifests itself through $X_{oo}(R)$ becoming very small for $R \lesssim R_1 + R_2$.

This is to be contrasted with most of the potentials calculated microscopically for heavy-ion collisions ([15,22,23]; see also, for example, [25]). These calculations may use the energy-density approach, the Thomas-Fermi approximation, the liquid-drop model, etc., etc., but they all attempt to follow to a greater or lesser degree the readjustments that the two nuclei must make as they begin to interact and overlap; distortion of the nuclear shapes, reaction to the Pauli principle, effects of the saturating nature of the nuclear forces, etc. Such a potential energy function is not relevant just to the X_{oo} component of the wavefunction (20) but is to be used in a description of the motion of a wave packet which includes a wide range of excited states of the separated systems. It is not to be identified with U_{op} of Eq. (24), and in principle it should not be used in an equation like Eq. (16) without at least allowing for the corresponding changes in the kinetic energy term resulting from the changes in the inertial properties [26]. As soon as we allow the system to be in eigenstates other than their ground states ($i,j \neq 0$), then in general the motion cannot be described simply in terms of the separation R of the centers-of-mass of the pair; other coordinates are needed. Further, there is an infinite number of such potential functions, each one corresponding to one or both of the nuclei in excited

states when widely separated. Transitions between these potentials result in non-elastic scattering and hence absorption from the elastic channel. However, most of these calculations of potentials are performed in the adiabatic limit so that such transitions do not occur and their absorptive and other effects are ignored; static polarization is included but not dynamic effects. Although I prefer to define the potential so that it reproduces the specific component χ_{oo} through Eq. (23), I freely admit that the physical processes just discussed still manifest themselves through the dynamic polarization term ΔU. This term certainly gives rise to the imaginary, absorptive potential that represents the implied scattering into non-elastic channels and, in principle, it also contributes to the real part.

Later we shall consider to what extent the first, 'folded' term U_F is a good approximation to the real part of the nucleus-nucleus potential. First we should remark briefly on the potentials produced by the other techniques [22] (but which, I stress again, are not designed to simply describe the evolution of $\chi_{oo}(R)$ alone). Although initially the polarization of the nuclear shapes in their mutual field will be equivalent to an attractive potential [27], the net effect of the various physical processes which occur when the two nuclei begin to overlap tend to be repulsive; for example, when there is total overlap, we would have a region with nuclear matter at roughly twice its normal density unless we allow relaxation. Consequently, while the simple folded potential $U_F(R)$ is very deep (of the order of 60 A_1 MeV deep at $R \approx 0$ if $A_1 << A_2$), these other calculations result in much shallower potentials, often with a repulsive 'core'. The precise form of these potentials depends upon the content of the calculations; whether a 'sudden' or an 'adiabatic' assumption is made, whether self-consistency (in the Hartree-Fock sense) is demanded, etc., etc.

The energy-density approaches [28] result in potentials similar to the proximity form to be discussed below. These take the potential of interaction to be the energy H of the combined system less the energies of the two separated nuclei, H_1 and H_2,

$$U(R) = \int [H(\rho) - H(\rho_1) - H(\rho_2)]\, d\underset{\sim}{r} \tag{26}$$

where $\rho(\underset{\sim}{r})$ is the density of the overlapping system and $\rho_1(\underset{\sim}{r})$, $\rho_2(\underset{\sim}{r})$ are the densities of the isolated nuclei. $H(\rho)$ is the energy functional for nuclear

matter at density ρ. If we take $\rho = \rho_1 + \rho_2$ [28], i.e. if we simply superpose the undistorted densities, this method takes account of the Pauli exclusion principle (increase of kinetic energy) and the saturation property of nuclear forces (density-dependence of effective interaction; e.g., Skyrme), but does not allow for readjustment of the densities (sudden approximation). As the nuclei first make contact, the attractive nuclear forces provide an overall attraction, but as the nuclei overlap more, the saturation and Pauli effects provide ever increasing repulsion (see Fig. 4). Allowing for readjustment of the densities reduces this repulsion; the degree of reduction will depend upon the speed of the collision. In the limit of large separations R, these U(R) will tend to the folding potential U_F (provided the finite range of the forces is taken into account properly). These effects have been discussed by Mosel (see [29], for example).

2.3. Proximity potentials

As an example of other nuclear potential functions, we consider a popular and rather general potential based upon the idea of proximity forces and developed by the Berkeley group [21]. This proximity potential has the form

$$U(r) = -V\, f(\zeta), \quad \zeta = (r-C_1-C_2)/b, \tag{27}$$

where

$$V = 2\pi b(y_1 + y_2)\,\frac{C_1C_2}{C_1+C_2}, \tag{28}$$

$$f(\zeta) = \begin{cases} 0.5(\zeta-2.54)^2 + 0.0852(\zeta-2.54)^3, & \zeta < 1.2511 \\ 3.437\,\exp(-\zeta/0.75), & \zeta > 1.2511. \end{cases} \tag{29}$$

Here C_i is the half-density matter radius of the ith nucleus and y_i its surface energy, $y_i \approx 1\ \mathrm{MeV\cdot fm^{-2}}$;

$$C_i \approx R_i\left[1 - \left(\frac{b}{R}\right)^2\right], \quad R_i \approx 1.28\,A_i^{1/3} - 0.76 + 0.8\,A^{-1/3}. \tag{30}$$

Also, b is a surface thickness parameter, $b \approx 1$ fm. We note that this has an exponential form at large r values like the empirical potential of Eq. (13), but that the slope is less. The recommended [21] value of $b \approx 1$ fm corresponds to $\alpha \approx 0.75$ fm in that equation instead of the empirical $\alpha \approx 0.63$ fm.

Equivalently, $\alpha = 0.63$ fm implies $b \approx 0.84$ fm. Further, the strength of the exponential, 3.437 V, has a dependence on the nuclear masses similar to the empirical one of Eq. (13), although the precise numerical definition of the radii is slightly different. Ignoring this last feature, the recommended values [21] of $b \approx \gamma \approx 1$ give a numerical coefficient of about 43 MeV fm^{-1} instead of the value 50 shown in Eq. (13). (However, when comparing these numbers, the different values of the slopes must also be taken into account. Although this difference appears small, it results in the exponential terms alone differing by a factor of 2 when $r-C_1-C_2 \approx 3$ fm.)

The proximity form (29) has a minimum at $\zeta = -1.37$ with a depth of -2.55 V, goes through zero at $\zeta = -3.33$ and is repulsive for smaller radii. At $r = 0$ it has the value

$$U(0) = 3.437 \text{ V} \exp\left(\frac{C_1+C_2}{0.75b}\right). \tag{31}$$

As an example, for $^{16}O + {}^{28}Si$ we have $V \approx 20$ MeV, the minimum occurs at $r \approx 4.5$ fm with a depth of about -50 MeV, U goes through zero at $r \approx 2.5$ fm and it has the value of about $+200$ MeV at $r = 0$. On the other hand, the system $^{136}Xe + {}^{209}Bi$ is predicted to have $V \approx 40$ MeV, with a minimum in U of about -150 MeV at $r \approx 11.4$ fm and a repulsion of about $+7500$ MeV at $r = 0$.

2.4. Fusion barriers

Before two nuclei can fuse, they must surmount the potential barrier U_B (repulsive Coulomb U_C plus attractive nuclear U_N), between them. Hence, one might expect to be able to deduce further information about the nuclear potential by studying fusion cross sections. Indeed, the simple semiclassical ideas behind Eqs. (7), (9) give an expression for the fusion cross section

$$\sigma_{fus} = \pi R_B^2 \left[1 - \frac{U_B}{E_{cm}}\right] \tag{32}$$

where $r = R_B$ is the position of the barrier and U_B is its height,

$$U_B = U_C(R_B) + U_N(R_B). \tag{33}$$

Values of $U_N(R_B)$ obtained in this way [21,30] are in general agreement with, for example, the proximity potential.

The particular interest here is that the barrier position R_B is significantly smaller than the strong absorption radii R_{SA} to which the elastic scattering is sensitive, typically by about 1 fm. Analyses [31] of fusion excitation functions which take detailed account of the quantal transmission across the potential barrier give information on the slope of U_N, as well as its value, at the barrier position. Such analyses have resulted in slopes considerably less than those extrapolated from the many analyses of elastic scattering. Using an exponential form like Eq. (13), Bass [31] (but see [70]) obtained $\alpha \approx 1.35$ fm rather than the 0.63 fm suggested by scattering data. Using a Woods-Saxon form, the Wilczynskis [31] obtain fits with diffuseness parameters suggested by their liquid-drop model,

$$a \approx \frac{17(C_1+C_2)}{16\pi\gamma C_1 C_2}\left[A_1^{2/3} + A_2^{2/3} - (A_1 + A_2)^{2/3}\right] \text{ fm}, \tag{34}$$

where the parameters are as defined above for the proximity potential. This gives values of 'a' of ~ 1 fm or greater.

I interpret this change in slope as due to the onset of repulsion as the two nuclear densities begin to overlap. However, this potential is not necessarily the same object (except asymptotically [70]) as the U_{op} needed to describe elastic scattering. There is no reason why fusion should only occur directly from the elastic channel; some prior non-elastic scattering may happen, for fusion can take place equally well from these quasi-elastic channels. Introducing these excitations is just another way of describing the friction and polarization (shape adjustments such as neck formation, etc.) experienced when the two nuclei begin to overlap. Various aspects of these changes are included in the types of potential calculations mentioned earlier, so that it may be more appropriate to use these for understanding fusion cross sections than it is for elastic scattering. The definition (24) seems more appropriate for describing elastic scattering; at least it is unambiguous!

Another criticism [32] is that a one-dimensional description of the motion in terms of the separation r of centers-of-mass becomes inadequate when excitation and polarization effects are important. The potential function U(r) becomes a potential surface; other coordinates are needed and the dynamical path over this surface must be studied. Simple expressions like Eq. (32) and their generalizations [31] may then be misleading.

3. Deep or Shallow Potentials?

3.1. Light systems

As we have stressed, in most cases heavy-ion scattering data determine only the tail of the nucleus-nucleus potential, so that it is meaningless to ask whether the potential in the interior is deep or shallow. However, there are some exceptional cases where it might be possible to learn about the potential at smaller radii. Clearly, these must be associated with (relatively) weak absorption, in some sense, so that the wavefunction penetrates to smaller radii and 'feels' the potential there.

Systematic deviations from strong absorption have been found in the scattering of 'light' heavy ions from light targets [33]. The effects are most pronounced for $^{16}O + ^{16}O$. They manifest themselves in the S-matrix elements no longer varying smoothly with L. Figure 5 shows an example for $^{16}O + ^{18}O$; the smooth dashed curves are for a typical strongly absorbing potential, while the full curves which show structure are for a shallow, weakly absorbing Woods-Saxon potential. The parameters of the latter were

$$\begin{aligned} V &= 12 + 0.25\, E_{cm} \quad \text{MeV} \\ W &= 0.9 + 0.0063\, E_{cm}^2 \quad \text{MeV} \end{aligned} \tag{35}$$

with R = 6.94 fm, a = 0.49 fm. The structure seen in Fig. 5 is explained as a ('surface transparency'); the surface waves are relatively weakly absorbed so that there is interference between the waves reflected from the surface or outer potential barrier and those reflected from the interior, centrifugal, barrier. I stress the word 'relatively' because it is clear that the lowest partial waves are almost completely absorbed and even the surface ones only show fluctuations about an average strong-absorption behaviour. (This is to be contrasted with the scattering of protons say, for which $|S_L| \approx 0.2 - 0.3$, typically, for the low partial waves.) In this particular case the surface transparency effects occurred for a potential whose real and imaginary parts had the same shape. It is possible to damp out the low partial waves even further without affecting the surface ones by adopting a deeper imaginary potential but with a smaller radial extent. This has been called a surface transparent potential. Similar results can be achieved by making the absorptive potential L-dependent so that it is weaker for the surface L-values.

These effects make the scattering more sensitive to the potential, and it has been concluded [33], in the context of using Woods-Saxon shapes, that shallow potentials similar to Eq. (35) are required to fit the data for these light systems and at these moderately low energies. However, only the surface waves are involved; the low L-waves are still strongly absorbed. Hence, we are learning about the potential inside the strong absorption radius but still in the 'surface' or grazing region. Another interesting feature of these results is the strong energy dependence; both V and W increase as E increases.

3.2. The system $^{16}O + ^{28}Si$

Another system that has been studied in detail is $^{16}O + ^{28}Si$. Extensive data are available (see [23], for example). One attempt [34] made a simultaneous analysis of differential cross sections at 11 bombarding energies from 33 to 215 MeV. It was found that there was a unique potential if one used the Woods-Saxon form (14) and demanded parameters which did not vary with energy. This potential was shallow with $V \approx 10$ MeV; the imaginary part was deeper ($W \approx 23$ MeV) but with a smaller radial extent so that it was 'surface transparent' to some extent. However, it was later found [35] that equally good fits could be obtained with deep real potentials (including a very deep folded potential) provided the demand for energy-independence was relaxed to the extent of allowing the diffuseness of the imaginary potential to vary with energy. Figure 6 compares the fits with the original shallow Woods-Saxon and the deep folded potentials. (Comparable fits were also obtained with a proximity potential of the form (27) which has a repulsive core).

At 215 MeV the strong absorption radius is about 8.2 fm but it was shown that the scattering was sensitive to the potential into about 6 fm. Nonetheless, although the deep and shallow potentials do differ appreciably at this radius (-30 MeV and -9 MeV, respectively), this extensive set of data cannot distinguish between them. However, none of the potentials succeeded in reproducing the oscillatory structure seen at energies from 50 to 66 MeV. More complete measurements in this region confirmed this structure beautifully, for adjacent targets as well as ^{28}Si; further, it could be fitted (see Fig. 7) by using a 'surface-transparent' potential quite different from the ones just discussed ([36] and Dehnard in [23]). Then data became available for larger scattering angles, out to nearly 180° [37], showing that the cross

section does not continue to fall but rises to about 10^{-2} of the Rutherford value at 180°. The surface transparent potentials account qualitatively for these data also (see Fig. 8); better fits are obtained [36] with an L-dependent absorption.

I do not think that we have reached a final understanding of these data yet (there is extensive discussion of these and similar data in Ref. [23]). However, it is clear that they contain information about partial waves with L less than the grazing values and hence about the interaction at distances smaller than the strong absorption radius. This is illustrated in Fig. 9 (from Dehnard in [23]) which shows the S-matrix elements for various potentials. E-18 is the shallow (but, we see, 'strongly absorbing') one of Cramer et al. which fits the forward angle scattering but not the oscillations at larger angles (see Fig. 6) while the other three do reproduce these oscillations to various extents. The lower partial waves are not completely absorbed for these latter three potentials and their S-matrix elements show considerable structure as a function of L, especially around L = 20 at the energy shown. This structure can be related to interference between waves reflected from an outer potential barrier and those reflected from an inner, primarily centrifugal, barrier. For this to occur, the nuclear potential must be deep enough to produce 'pockets' in the curves for the total 'potential', Coulomb + nuclear + centrifugal. This is shown on the left side of Fig. 10, which is typical for the potentials that fit the data. These are still 'shallow' (V ~ 25 MeV), but sufficiently deeper than the earlier E-18 potential (V = 10 MeV, right side of Fig. 10) to produce pockets accessible at this energy for $L \lesssim 25$. These potentials are also remarkably like those deduced for lighter systems, such as $^{16}O + {}^{16}O$, both in their strengths and in the energy dependence found [38] (as in Eq. (35)). (It is also amusing that the very deep, ~ 600 MeV, folded potential can produce similar cross section behaviour with a suitable choice of imaginary potential, although not sufficient work has been done yet to see whether equally good fits to the data can be obtained.)

Of course, there must not be too much absorption for these important partial waves or else the inner reflected wave will be completely attenuated and produce no interference: hence, the requirement of surface transparency, at least. Figure 10 also indicates that different potential prescriptions result in quite different behaviours of the S_L for small L although those for

L ~ 20 are similar; apparently it is the latter that are required to fit the data in this case.

3.3. Barrier penetration and reflection

Whether we finally conclude that these particular phenomena are simply due to the particular form of an interaction potential or to some more complicated dynamical process, it is of interest that simple potentials can manifest this kind of behaviour. An illuminating discussion of these effects has been given by Brink and Takigawa [38], particularly for cases where the total potential has pockets for the important partial waves, as in the left side of Fig. 10. They use a generalization of the WKB approximation which is applicable to complex potentials and to energies which are either above or below the outer barrier of the pocket. This involves more than one turning point for each partial wave, and the turning points are complex (see also [3,4]). The result is that under certain circumstances the S-matrix can be written (see Appendix)

$$S_L \approx S_L^{(B)} + S_L^{(I)} \tag{36}$$

where B(barrier), I(interior) denote contributions from the outermost and innermost turning points, respectively; that is, reflection from the outer barrier and reflection from the inner, centrifugal barrier. $S_L^{(B)}$ includes effects due to penetration of the outer barrier. $S_L^{(I)}$ is affected by the absorption in the inner, pocket, region; if the absorption is strong enough, then the inner reflected wave is completely damped and $S_L^{(I)} \to 0$, while $S_L^{(B)}$ goes over to the simple WKB value for a single turning point. (Even when the total potential does not have pockets, such as the right side of Fig. 10, there is an inner, complex, turning point, but the inner contribution is completely damped out.)

Corresponding to Eq. (36), the total scattering amplitude can be written as a sum of two parts,

$$f(\theta) = f_B(\theta) + f_I(\theta). \tag{37}$$

The scattering of $\alpha + {}^{40}Ca$ at energies of ~ 30 MeV provides a good example of those effects. This case has become the prototype of so-called "anomalous large-angle scattering" (ALAS) because the cross section (in ratio to the Rutherford one) rises at large angles (in fact, as Fig. 11 shows, it rises to

~ 2 × $d\sigma_R$ at 180° at 29 MeV). Numerous explanations have been put forward for this ALAS, but recently it has been shown [39-42] to be explicable in terms of simple potential scattering provided (i) the absorption is relatively weak, (ii) the real potential is deep and has the appropriate shape (for example [39], like the Woods-Saxon form raised to the power 2.65 and with a depth ~ 300 MeV). Figure 12 shows the cross sections due to f_B and f_I separately, as well as their coherent sum. The outer barrier scattering, $\sigma_B = |f_B|^2$, has the usual characteristics of strong absorption scattering, while reflection at the inner barrier, $\sigma_I = |f_I|^2$, provides the large angle scattering. The latter is primarily due to the 'low' partial waves; Fig. 13 shows the scattering matrix elements for the two contributions. As expected, the inner amplitude is very sensitive to the absorptive potential; W = 16.6 MeV corresponds to Fig. 12, while increasing it to W = 26.6 MeV reduces $|S_L^{(I)}|$ by a factor of 5 but has almost no effect on $S_L^{(B)}$. We note also why we speak of 'relatively weak' absorption in these cases. Even with W = 16.6 which gives the so-called ALAS, $|S_L^{(I)}| \lesssim 0.07$ or the transmission (penetration) coefficients for the low partial waves are $T_L \gtrsim 0.995$. Only a small amplitude is needed for these waves in order to produce large effects. (Note also that plots of $d\sigma/d\sigma_R$ tend to exaggerate the magnitude of these effects; the actual cross section at 180° is about 6 mb/sr, which is, for example, only 1/20 times the cross section on the peak at about 35°.)

The mid-angle range (~ 90° here) where the two amplitudes interfere strongly is particularly sensitive to the real potential shape because this both affects the relative phase of the two terms and it affects the rate of decrease of $f_B(\theta)$ with angle. The latter is particularly sensitive to the surface diffuseness of the potential. The observed interference pattern (Fig. 11) favours a deep real potential with a large surface diffuseness [38] (which happen to be the characteristics of a folded potential -- see below).

The interference between $S_L^{(B)}$ and $S_L^{(I)}$ is also responsible for the structure in the total $|S_L|$ for L ~ 10 (Fig. 13). This is reminiscent of the structures seen in the heavy-ion cases we studied earlier (Figs. 5, 9). A recent analysis [43] implies that they have a similar origin for systems like $^{16}O + ^{16}O$, but in those cases they are associated with the shallow potentials like Eq. (35).

3.4. The systems $^{12}C + ^{12}C$ and $^{6}Li + ^{40}Ca$

Another system for which there are many data is $^{12}C + ^{12}C$, detailed angular distributions being available for various energies up to 127 MeV. Analyses [44] showed that while the shallow potentials introduced by the Yale group gave adequate fits to new 70-127 MeV data for angles less than about 45°, no good fit to the larger angles was found with such Woods-Saxon potentials. However, the use of deep (~ 400 MeV) folded potentials resulted in a marked improvement (Fig. 14). In this case the scattering was found to be sensitive to the potential for separations of the nuclear centers as small as 3 fm $\left[= 0.66\ (A_1^{1/3} + A_2^{1/3})\right]$ where ReU is well over 100 MeV deep, although the strong absorption radius is about 7 fm. The folded potential has a shape which cannot be closely matched by a Woods-Saxon form in this 3-7 fm region. On the other hand, as in the $\alpha + ^{40}Ca$ case, the folded potential is closer in shape to some power ($\gtrsim 2$) of the Woods-Saxon form; this form can also be used to fit the data and such fits also result in a deep potential. Consequently, we must conclude that, within the context of using simple potential wells, these $^{12}C + ^{12}C$ data require a deeper potential than had been thought previously.

A typical set of the S-matrix elements for this $^{12}C + ^{12}C$ scattering is shown in Fig. 15. In particular, the magnified section above shows that the differences between the shallow Woods-Saxon and deep folded potentials are manifested in the $|S_L|$ for low L values. One can visualize a decomposition of the $|S_L|$ for the deep potential into interior and barrier contributions [45] just as in Fig. 13. These low L waves play a rôle because of the relatively weak absorption combined with the depth of the real potential (though again it must be emphasised that there is very little penetration into the interior, strong overlap region. $T_L \gtrsim 0.9996$ for the low L and the radial wavefunctions plotted in Fig. 16 show that the probability of the system being in this region is small).

The system $^{16}O + ^{28}Si$ was discussed above. It is too early to say yet whether these data can also be fitted adequately by very deep potentials like that of the folding model, but clearly it is important to study the data further in that context. Another heavy-ion system showing similar large-angle behaviour is $^{6}Li + ^{40}Ca$ at 30 MeV; it has been shown [46] that these data can be fitted by a deep (but relatively weakly absorbing) potential of

the folded form (see Fig. 17). The corresponding S-matrix elements for low L are similar in form to the other cases discussed. Just as with the other systems, this behaviour goes away as the energy is increased (Fig. 1a) because the absorption needed increases and the scattering begins to appear like the standard strong absorption type.

3.5. Summary

In summary, although most heavy-ion systems at most energies exhibit strong absorption characteristics that only allow determination of the tail of the nucleus-nucleus potential there are some cases, especially for some lighter systems at lower energies, where the absorption is weaker. This allows low-L waves reflected from the interior centrifugal barrier to play a small but important rôle. These waves are sensitive to the potential at distances closer than the strong absorption radius. Consequently, although the information obtained may not be completely unambiguous [45], it does provide important constraints upon any model. In some cases, at least if we demand a simple potential model description, it is implied that the real potential should be 'deep'. There are also indications in these cases, as for recent work on alpha scattering [39-42,47], that the Woods-Saxon shape is not adequate; better agreement with experiment can be obtained with shapes like some power n ($n \gtrsim 2$) of the Woods-Saxon form. Further, in these cases, the potential can be related to 'realistic' effective nucleon-nucleon interactions through the folding model. In answer to objections that the potential can have no meaning at distances where two composite nuclei overlap appreciably, I can only say that I believe we are dealing with the potential U_{op} of Eq. (24) that describes only the ground-state component X_{oo} of the wavefunction (20) whereas one's intuition pictures the violent things that undoubtedly happen to the two nuclei. Quantally, there will always be a small $X_{oo}(\uparrow)$ even for small $\uparrow$. The $X(\uparrow)$ obtained from the optical potential descriptions is small, but whether it is small enough, I do not know.

4. Folded Potentials for Heavy- (and Light-) Ion Scattering

4.1. Definition of folded potentials

The idea of a folded potential has, of course, a long history. The electrostatic potential $U_c(\underset{\sim}{r})$, due to a charge distribution $\rho_{ch}(\underset{\sim}{r}')$, is given

by a single folding,

$$U_c(\underset{\sim}{r}) = \int \frac{\rho_{ch}(\underset{\sim}{r}')}{|\underset{\sim}{r}-\underset{\sim}{r}'|} d\underset{\sim}{r}', \tag{38}$$

while the electrostatic interaction between two charge distributions is given by a double folding,

$$U_c(\underset{\sim}{R}) = \iint \frac{\rho_{ch1}(\underset{\sim}{r}_1)\rho_{ch2}(\underset{\sim}{r}_2)}{r_{12}} d\underset{\sim}{r}_1 d\underset{\sim}{r}_2 \tag{39}$$

where $\underset{\sim}{r}_{12} = \underset{\sim}{R} + \underset{\sim}{r}_2 - \underset{\sim}{r}_1$ (see Fig. 18). In the nuclear case, the Coulomb interaction $1/r_{12}$ is replaced by a nucleon-nucleon (effective) interaction v_{12}. We discussed in Sect. 2.1 a formalism in which the first term $U_F(R)$ in Eq. (24) was identified as a folded potential,

$$U_F(R) = \iint \psi_o^*(\xi_1)\phi_o^*(\xi_2) \sum_{ij} v_{ij}\, \psi_o(\xi_1)\phi_o(\xi_2) d\xi_1 d\xi_2 \tag{40}$$

where nucleon i is in nucleus 1, nucleon j is in nucleus 2 and ξ_1, ξ_2 refer to the <u>internal</u> coordinates of these two nuclei, respectively. If v_{ij} is a local interaction, $v_{ij} = v(\underset{\sim}{r}_{ij})$, then the potential (40) may be reduced to the analogue of Eq. (39):

$$U_F(R) = \iint \rho_1(\underset{\sim}{r}_1)\rho_2(\underset{\sim}{r}_2)v(\underset{\sim}{r}_{12})d\underset{\sim}{r}_1 d\underset{\sim}{r}_2, \tag{41}$$

where $\rho_i(\underset{\sim}{r}_i)$ is the one-body density for the ith nucleus. This we call a <u>double-folded potential</u>.

We may break the double folding into two steps and rewrite Eq. (41):

$$U_F(R) = \int d\underset{\sim}{r}_1\, U_{2N}(\bar{\underset{\sim}{r}}_{12})\rho_1(\underset{\sim}{r}_1), \tag{42}$$

where

$$U_{2N}(\bar{\underset{\sim}{r}}_{12}) = \int d\underset{\sim}{r}_2\, \rho_2(\underset{\sim}{r}_2)v(\underset{\sim}{r}_{12}), \tag{43}$$

and $\bar{\underset{\sim}{r}}_{12} = \underset{\sim}{r}_{12} - \underset{\sim}{r}_2 = \underset{\sim}{R} - \underset{\sim}{r}_1$. Then U_{2N} is a folded potential for the interaction of nucleon 1 with nucleus 2 (analogous to Eq. (38)), which we shall return to later.

4.2. Single-folded potentials

The form of Eq. (42) has often been invoked but with the use of empirical, phenomenological nucleon-nucleus optical potentials in place of U_{2N}. This so-called single-folding model has invariably overestimated the strength of the real potential required by heavy-ion scattering data by a factor of about two [48].

This is puzzling at first sight, since we shall see that the folded U_{2N} of Eq. (43), which is an ingredient of the successful (see below) heavy-ion potential (42), is also moderately successful in reproducing nucleon scattering. Several explanations of this apparent paradox have been offered:

(i) When phenomenological nucleon potentials are used, they are generally taken to be of Woods-Saxon form. Now the long-range behaviour of $U_F(R)$ is sensitive to the surface features of the potential substituted for U_{2N} in Eq. (42), and the Woods-Saxon form may not be an adequate representation. For example, it has been shown [49] that the square of a Woods-Saxon shape may give equally good fits to the nucleon scattering data but can result in a considerable reduction in the strength of the tail of the single-folded heavy-ion potential.

(ii) In general, the interaction v is density-dependent; in the folding integral (41) it will depend upon the densities of both nuclei. A nucleon-nucleus empirical potential incorporates effects due to the density of one nucleus alone. When such a phenomenological potential is used in the single folding integral (42), the effects due to the density of the other nucleus are neglected, whereas the potential U_{2N} of Eq. (43) remains implicitly dependent upon the density of nucleus 1. This effect need not be negligible [50].

(iii) A phenomenological nucleon-nucleus potential includes the effects of coupling to other channels (ΔU in Eq. (24)) and these are likely to be quite different when the incident nucleon is bound in another nucleus compared to when it is free. Indeed, we shall see that the U_{2N}, constructed according to Eq. (43), has some deficiencies compared to phenomenological potentials; in particular, it has somewhat too short a range. This may be because the contributions to the real potential for nucleon-nucleus scattering from the ΔU terms are important. (In this same context, because the ΔU for nucleons and for heavy ions will be very different, we do not expect single folding with phenomenological nucleon-nucleus potentials to be of any use for predicting

the imaginary part of the heavy-ion potential.)

4.3. The interaction v

4.3.1. Effective interactions

The bare nucleon-nucleon interaction is too strong to be used as the v which appears in the double folding integral (41). It has been popular to use for v a simple potential, such as a Gaussian which fits low-energy nucleon-nucleon scattering. However, this has been shown [10.48] to overestimate the heavy-ion potential by roughly a factor of two. (It has also been shown [51] to predict (p,p') cross sections which are too large.)

We believe it is desirable to use an effective interaction v which is based upon a realistic nucleon-nucleon force, since one goal is to obtain a unified description of nucleon-nucleon, nucleon-nucleus and nucleus-nucleus scattering. As a consequence, our effective interaction is some kind of G-matrix. There is no guarantee of the existence of such a single, simple, effective interaction of this kind which may be used in a variety of physical circumstances. However, it is certainly worth seeing how far we can go with such a simple concept and to find what kind of corrections we may have to make in particular cases.

A 'high energy' approach to this problem was used by Dover and Vary [52]. In the high-energy limit (or impulse approximation) v would become the (complex) t-matrix for free space nucleon-nucleon scattering. However, for the low-energy ($\lesssim$ 20 MeV per nucleon) heavy-ion collisions that we are considering, there are large corrections to be made for the effects of the nuclear medium in which the two interacting nucleons are embedded (Pauli principle, off-shell propagation and Fermi motion of the nucleons). One 'low-energy' approach that we consider here [53] assumes that the effective interaction v is similar to the G-matrix for two nucleons bound near the Fermi surface. One consequence of this assumption is that v is real. More recent work on nucleon-nucleus scattering [54] has taken into account that the projectile nucleon is in the continuum above the Fermi sea. This yields a complex G-matrix; however, it seems probable that the absorptive processes in heavy-ion scattering are very different so that it may be preferable to treat the imaginary potential phenomenologically.

It is worth remarking that replacing the bare nucleon-nucleon potential by an effective or G-matrix interaction is a process analogous to the

derivation of the effective interaction U_{op} in Sec. 2.1. The G-matrix transformation itself incorporates some polarization effects, namely the short-range correlations between pairs of nucleons, and in principle allows us to use simpler nuclear wavefunctions such as those of the shell model. Then a full derivation of the operator U_{op} of Sec. 2.1. would go explicitly through this two-stage projection from the original many-body problem (see, for example, [55]).

From its origin as an effective interaction or G-matrix, it is clear that, in general, this v should be both energy dependent and density dependent. The usual way of handling the density dependence is to use the local density approximation. In this we assume that the effective interaction between two nucleons embedded in nuclear medium at some position where the density has a certain value is given by the G-matrix for infinite nuclear matter with the same density value. This ignores the effects on G of density gradients. Also, because the force has a finite range, two positions, $\underset{\sim}{r}_1$ and $\underset{\sim}{r}_2$, are involved; frequently one uses the density at the centre of gravity, $\frac{1}{2}(\underset{\sim}{r}_1 + \underset{\sim}{r}_2)$. This kind of uncertainty is further aggravated in heavy ion double folding because there are two densities, $\rho_1(\underset{\sim}{r}_1)$ and $\rho_2(\underset{\sim}{r}_2)$.

4.3.2. Spin- and isospin-dependence

The effective v also depends upon the spins and isospins of the two interacting nucleons. The central parts of v may be written in the form

$$v_{12} = v_{00}(r_{12}) + v_{01}(r_{12})\underset{\sim}{\tau}_1\cdot\underset{\sim}{\tau}_2 + v_{10}(r_{12})\underset{\sim}{\sigma}_1\cdot\underset{\sim}{\sigma}_2 + v_{11}(r_{12})\underset{\sim}{\sigma}_1\cdot\underset{\sim}{\sigma}_2\ \underset{\sim}{\tau}_1\cdot\underset{\sim}{\tau}_2. \qquad (44)$$

In general there will be spin-orbit and tensor terms as well. If neither the target nor the projectile has any spin, the ρ_i are spherically symmetric and U_F becomes a function only of the magnitude of $\underset{\sim}{R}$. Then the v_{ST} terms in Eq. (44) with S = 1 do not contribute. (Although there are dipole terms, from the expansion of $v_{1T}(r_{12})$ into products of spherical tensors in $\underset{\sim}{r}_1$ and $\underset{\sim}{r}_2$, which can be combined with the $\underset{\sim}{\sigma}$ operators to form monopole products, these are pseudoscalars of the form $\underset{\sim}{\sigma}\cdot\underset{\sim}{r}$ and have zero expectation value because of parity.)

More generally, U_F will be non-spherical and spin-dependent, but it seems that the spin terms usually have relatively small effects on the cross sections (although, of course, they are important for polarization phenomena). The non-spherical parts of U_F, which will result if one or both of the

densities ρ_i are non-spherical, can induce inelastic scattering to collective rotational or vibrational states [52]. They only affect the elastic scattering from spin-zero nuclei explicitly if we make coupled-channel calculations which include these excited states; I do not consider that here. The non-spherical parts may directly affect the scattering from odd-nuclei (which have non-zero spin), but one comparison [55] of ^{16}O from $^{59}Co(I^{\pi} = \frac{7}{2}^{-})$ and $^{60}Ni(I^{\pi} = 0^{+})$ showed negligible differences.

Equation (41) is oversimplified in that differences in interactions between like and unlike nucleons are ignored; that is, isospin is not referred to explicitly. If one or both nuclei have N = Z, and hence zero isospin, $\langle \underset{\sim}{\tau}_i \rangle = 0$ and only v_{ST} terms in Eq. (44) with T = 0 can contribute. However, even when $N \neq Z$ for both nuclei, explicit evaluation for typical cases shows the T=1 contributions to U_F to be negligible for 'realistic' interactions v.

These various considerations lead us to evaluate the folding integral (41) with spherical densities ρ_i and the central S=T=0 part, v_{00}, of the interaction (44).

4.3.3. Rôle of the long-range one-pion-exchange potential (OPEP)

The OPEP has a tail of Yukawa form with a range of about 1.4 fm; this is the component of the nucleon-nucleon force with the longest range. It is also a moderately weak component, and we expect it to reappear in a G-matrix essentially unchanged. Hence, the effective v will have an OPEP tail. However, the OPEP is proportional to $\underset{\sim}{\sigma}_1 \cdot \underset{\sim}{\sigma}_2 \; \underset{\sim}{\tau}_1 \cdot \underset{\sim}{\tau}_2$, that is, it has an S=T=1 character. So it does not contribute to v_{00}, and the longest range expected in v_{00} is at most that of two-pion exchange.

In an earlier approach [57] we used for v the long-range parts of the even-state Hamada-Johnston potential, in the sense of the Moszkowski-Scott separation method [58]. Although this gave moderately good results for nucleon scattering [51,57], it overestimated heavy-ion potentials by more than a factor of two [10,48]. Indeed, in some cases, it did not yield an adequate fit to the data and this discrepancy could be traced [10] to the long range of the OPEP component in the force. This is illustrated for the $^{16}O + {}^{60}Ni$ system in Fig. 19; the even-state OPEP term alone gives a large contribution to the potential near the strong absorption radius and has an unacceptably small slope. However, as we just remarked, this OPEP component must be spurious and arises because initially we took only the even-state interaction

and ignored the odd-state parts. In a correct approach, at least the OPEP should be included in odd states. Then in the combination [57] of even and odd parts which makes up v_{00},

$$v_{00} = \frac{3}{16} v_{\text{triplet even}} + \frac{3}{16} v_{\text{singlet even}} + \frac{9}{16} v_{\text{triplet odd}} + \frac{1}{16} v_{\text{singlet odd}} \tag{45}$$

the odd and even parts of the OPEP must cancel so that this long-range component does not contribute.

Another illustration that the range of the effective interaction is extremely important is shown in Fig. 20. Folding calculations were made for $^{40}Ca + {}^{40}Ca$ using either a single Gaussian or a single Yukawa for v but with various ranges. In each case the strength was adjusted to give a folded potential of 1.35 MeV at R = 10.6 fm, as appropriate for $^{40}Ca + {}^{40}Ca$ scattering. Figure 20 shows the resulting volume integral of v,

$$J = 4\pi \int v(r)\, r^2\, dr, \tag{46}$$

against its RMS radius. (The value J = -400 MeV fm^3 is roughly the value deduced from nucleon-nucleus scattering, as well as from realistic G-matrices [53,54].) For example, a zero-ranged force would require a value of J that is about five times larger than one with $\langle r^2\rangle^{1/2} = 2$ fm. Figure 20 also illustrates that, while J and $\langle r^2\rangle$ may be used to characterise the v fairly well, the choice of its shape is not entirely unimportant. This shape-dependence may be studied further by expanding in the radial moments of v,

$$U(R) = \int \rho_1(r_1)\rho_2(|\underset{\sim}{R}-\underset{\sim}{r}_1|)d\underset{\sim}{r}_1 - \frac{1}{6}\langle r^2\rangle \int \underset{\sim}{\nabla}\rho_1 \cdot \underset{\sim}{\nabla}\rho_2\, d\underset{\sim}{r}_1 + \ldots. \tag{47}$$

where $\langle r^2\rangle$ is the MS radius of v. In the tail regions of interest, both ρ_1 and ρ_2 are falling exponentially and for typical realistic values of $\langle r^2\rangle$ the two terms in Eq. (47) are comparable in magnitude. Then some higher-order terms are needed.

4.3.4. The M3Y interaction

I shall present here some results of using the effective interactions of Bertsch *et al.* [53] which are expressed as sums of three Yukawa terms; I call these M3Y. One Yukawa term is taken to be the OPEP; the second was chosen to

have a range of 0.4 fm which roughly simulates multiple pion exchange, and the third range of 0.25 fm was chosen for computational convenience. The strengths of the latter two terms for the even-state v were chosen to reproduce the G-matrix elements (in an oscillator basis) of the Reid soft-core potential. For the odd-state v, I use their fit to the "Sussex" matrix elements of Elliott et al. Full details are given by Bertsch et al. [53]. Then the v_{00} component of Eq. (44), which receives no contribution from the OPEP term, has the form

$$v_{00}(r) = \left[7999\,\frac{e^{-4r}}{4r} - 2134\,\frac{e^{-2.5r}}{2.5r}\right] \text{MeV}, \tag{48}$$

and a volume integral of $J_{00} = -146$ MeV fm^3. On the other hand, if we assume that only the OPEP force acts in odd-states, we get instead

$$v_{00}(r) = \left[6315\,\frac{e^{-4r}}{4r} - 1961\,\frac{e^{-2.5r}}{2.5r}\right] \text{MeV}, \tag{49}$$

with $J_{00} = -337$ MeV fm^3. It has been shown [59] that, in the folded potential, there is almost complete cancellation between the direct and exchange (see below) contributions arising from the short-range parts of the odd-state interaction which are included in Eq. (48). Consequently, the two interactions (48) and (49) are essentially equivalent for the construction of heavy-ion potentials (see Fig. 19). Except when otherwise indicated, the calculations reported here use the form (48).

The potentials (48) and (49) are not as short ranged as their component Yukawas might suggest. The form (48) has $\langle r^2 \rangle = 7.26$ fm^2, the same as a single Yukawa with a range of 1.10 fm or a Gaussian with a range of 2.20 fm, while the potential (49) has $\langle r^2 \rangle = 3.11$ fm^2. Further, Goldfarb [60] has shown that 50% of the folded potential near the strong absorption radius comes from v(r) of Eq. (49), with $r \geq 1.6$ fm.

Except for a slow dependence of the knock-on exchange terms (see below), the interactions (48) and (49) are independent of energy. Indeed, from their origin as fits to oscillator matrix elements, they represent an average over a certain range of energies. Further, these interactions are independent of the density of nuclear matter in which the two nucleons are embedded. Again, they represent an average of the interaction for densities ranging from zero

to normal nuclear matter; considering the oscillator matrix elements upon which they are based suggests that they are representative of an average density of about 1/3 of nuclear matter. This would seem not inappropriate for most direct scattering which largely occurs in the surface region of the nuclear density distribution. Even for the very peripheral heavy-ion scattering (see Fig. 3), the folding integral samples regions into where the nuclear density has almost its full value. This is illustrated by Fig. 21 which shows the variation of the potential for $^{84}Kr + ^{209}Bi$ at three separations R as the density $\rho(r)$ of each nucleus is cut off at some $r_{max} = na+c$ where a = 0.5 fm is the density diffuseness parameter and c is its half-density radius. (Simple Fermi shapes were assumed for the densities with c(Kr) = 4.83 fm, c(Bi) = 6.63 fm.) The strong absorption radius for this system is about R = 14.2 fm, when the half-density points are separated by 5.5 a. We see that at this separation, about 20% of the potential is still coming from where the tail of one density distribution is penetrating inside the half-density point of the other. To reach 1% accuracy for R = 14.2 fm, the cut-off must be displaced to where the density tail has fallen to 10^{-4} of the central value and this is probing the other nucleus into where its density has reached its full central value.

With such a wide range of densities being sampled, it might be feared that the kind of density average implied in the M3Y G-matrix would not be adequate and that an explicit density dependence should be considered. This was indeed done using a density-dependent G of Day et al. [61] which was also derived from the Reid potential. It turns out that this gives almost identical heavy-ion folded potentials. (Applications to light-ion inelastic scattering [62] do not show as close agreement, but the differences are not large.) Consequently, the averaging implicit in the M3Y G seems to be appropriate for this use.

4.4. Exchange

The expressions (25), (40) for the folding potential do not explicitly show any effects due to antisymmetrization between nucleons in different ions, although the individual nuclear wavefunctions ψ_o, ϕ_o are themselves assumed to be antisymmetric. As we have discussed above, the dominant contributions to the potential near the strong absorption radius come from the surface and tail regions of the nuclear densities and the two densities do not overlap

very much. Then exchange of one nucleon from each ion will be the leading corrections. Of these, the minimum rearrangement is needed if the two interacting nucleons are interchanged. (This has been called 'knock-on' exchange in nucleon-nucleus scattering [57,63].) This term is included formally in the double-folding integral (41) by replacing

$$v_{12} \to (1 - P_{12})v_{12}, \tag{50}$$

where P_{12} exchanges all the coordinates of nucleons 1 and 2. At least two groups [59,63,64] have estimated the importance of this exchange term for a common force and have found that it can be included quite accurately by replacing $-P_{12}v_{12}$ in Eq. (50) by the pseudopotential

$$\hat{J}(E)\delta(\underset{\sim}{r}_{12}). \tag{51}$$

The strength $\hat{J}$ depends strongly on the particular (S,T) component of the interaction (6), but it depends very weakly on the energy E for energies between about 5 and 20 MeV per nucleon. We have adopted the approximation (51) for the calculations reported here. The values of $\hat{J}$ were obtained by calibrating [63] against 'exact' DWBA calculations of this term in proton scattering. At E = 10 MeV, $\hat{J}_{00}$ = -262 MeV fm^3 for the interaction (48) or $\hat{J}_{00}$ = -81 MeV fm^3 for the interaction (49). These values change only by a few per cent between 5 and 20 MeV so their energy dependence can be neglected for our purpose.

Consequently, the M3Y effective interaction including exchange that is to be employed in the folding Eq. (41) is

$$v'_{00} = v_{00} + \hat{J}_{00}\,\delta(\underset{\sim}{r}_{12}). \tag{52}$$

With the v of Eq. (48), this v' has a volume integral of J'_{00} = 408 MeV fm^3 and mean square radius of $\langle r^2\rangle$ = 2.60 fm^2. Very similar values are obtained with a purely OPEP force in odd-states, v of Eq. (49); then we have J'_{00} = 418 MeV fm^3 and $\langle r^2\rangle$ = 2.51 fm^2. The former version was used for the results reported here.

4.5. Nuclear densities

The nuclear densities $\rho_i(r_i)$ are important ingredients in the folding integral. We learn something about proton distributions from electron scattering, but we do not have direct knowledge of the neutron densities

(although presently high-energy proton scattering is being used to deduce the total matter distribution in nuclei). Uncertainties about the neutrons is perhaps the largest uncertainty in any test of a folding model. However, since the folded potential is very sensitive to the extent of the matter distribution, this raises the possibility of learning about the neutron distribution from heavy-ion scattering, provided some interaction, together with the folding procedure, can be shown to be valid. An example is provided by the system $^{16}O + ^{208}Pb$. If we assume neutrons with $\rho_n = (N/Z)\rho_p$ instead of the Hartree-Fock neutron density (which has ρ_n extending slightly beyond ρ_p), the folded potential near the strong absorption radius is reduced by 35%. This has a large effect on the scattering.

The mean square radius (MSR) is a useful characteristic of the densities. Although the folded potential (near the strong absorption radius) does depend to some extent upon the detailed surface shape of the densities, it is largely determined by the MSR. This is illustrated for $^{16}O + ^{60}Ni$ in Fig. 22 which shows the potential obtained from a variety of prescriptions for the densities. Although there are fluctuations, the trend is to increase linearly with the sum of the MSR. (This is better understood in terms of Fourier transforms; only the small momentum components of the three factors in the integrand of the folding integral are important [60].)

4.6. Applications to scattering data

4.6.1. Nucleons

Although other G-matrix interactions [54] have been tested against elastic scattering, the M3Y effective interaction has mostly been applied to inelastic scattering, using transition densities from RPA calculations whose proton parts, at least, can be tested by electron scattering and B(EL) measurements. The overall agreement has been very satisfactory [53,62]. For completeness, Fig. 23 shows some elastic scattering comparisons. Only the real, central potential is calculated by folding; the phenomenological imaginary potentials of Becchetti and Greenlees were taken without change. The agreement is moderately good and could be improved by arbitrarily varying the imaginary and spin-orbit terms. However, a conventional Woods-Saxon potential can give better fits which have a χ^2 value which is a factor of two smaller. When we compare the potentials, we find that this implies that the folded potential has a mean square radius which is too small. We do not know

whether this is due to a deficiency in the interaction or in the treatment of exchange (Sec. 4.4) or to the neglect of the dynamic polarization term ΔU of Eq. (24).

Nonetheless, Fig. 23 indicates that the M3Y interaction is not grossly wrong for nucleon scattering.

4.6.2. Alphas

The M3Y interaction has not yet been applied extensively to alpha scattering. Figure 11 did show one example, $^{40}Ca + \alpha$. In this case the folded potential is remarkably close [41] to the phenomenological one deduced earlier by Michel and Vanderpoorten [39], and hence also describes the large angle scattering.

The folded potential for $\alpha + \alpha$ with M3Y is equally close to the phenomenological potential found [65] to fit $\alpha + \alpha$ scattering phase shifts up to an energy of 40 MeV.

4.6.3. The Li ions

The one exception to the general success of folding with the M3Y interaction that has been noted [66] so far is for the scattering of ^{6}Li ions. The model consistently overestimates the ^{6}Li-nucleus potential by almost a factor of two. As examples, Figs. 1(a) and 17 show that good fits to data can be obtained but only if the real potential is reduced by a factor of about 0.6. It is natural to associate this discrepancy with the polarization and break-up of the ^{6}Li in the field of the target nucleus, but no theory based upon this has yet appeared.

Very little analysis of ^{7}Li scattering has been done with folded potentials, but preliminary results do <u>not</u> indicate any similar anomaly for this ion.

4.6.4. Heavier ions

A variety of systems have been studied ([67]; see also [10,18,44,46,56]). The Hartree-Fock densities of Negele [68] were used for the closed-shell nuclei $^{40,48}Ca$, ^{90}Zr and ^{208}Pb. Shell-model densities were constructed for the other nuclei with the constraints that (i) the proton radii must be in agreement with electron scattering measurements, and (ii) the least-bound nucleons should have the observed separation energies. When N = Z, it was assumed that protons and neutrons had the same distribution. The real, folded

potential was multiplied by a normalizing factor N and the value of N was varied to optimize the fit to the data. If this gives $N \approx 1$, it means that the model is successful. The imaginary potential was taken to be of Woods-Saxon shape and the minimum parameter variation which resulted in good fits to the data was allowed. In most cases the radius could be fixed at $1.3(A_1^{1/3} + A_2^{1/3})$ fm; often the diffuseness could be fixed at a = 0.6 fm.

The results are summarized in Table 1. Some of the fits are shown in Figs. 1(a), 1(b), 2, 6, 14, and 17. Figure 24 shows some of the light systems which exhibit a 'Fraunhofer' type of diffraction pattern. Figure 25 shows a heavier system, $^{40}Ca + ^{40}Ca$, in which the data at 143.6 MeV were fitted and the same potential used at the other energies. Figure 26 shows an intermediate system, $^{16}O + ^{40}Ca$, at energies from 40 MeV to 214 MeV; in this case, the 74-MeV data were fit and the same potential used at the other energies.

Table 1 indicates optimum values of N which are close to unity but which tend to be a little larger than one; the unweighted average value and RMS deviation is 1.09 ± 0.13. This deviation from 1.0 might be due to an underestimate of the exchange contribution (Sec. 4.4); an alternative approximation [61] which uses the Slater approximation to the one-body mixed density predicts larger exchange terms than the pseudopotential (51). Some of the fluctuations in the N values are undoubtedly due to errors in the density distributions that have been used. Other fluctuations will be due to idiosyncracies in the data that affect the fitting procedure. Still others may represent true physical effects. An interesting case is $^{16}O + ^{40}Ca$ at 56 MeV [14]. Figure 26 shows that the data at 40 MeV, 74 MeV and higher energies are nicely fit by a single potential, but that at 56 MeV this potential does not predict a large enough oscillation about the Rutherford cross section at small angles. This was emphasised in Fig. 2(b) which shows the 56-MeV cross sections plotted linearly. The oscillation at small angles would indicate $N \gtrsim 1.5$, while the optimum fit to all angles gives N = 1.27 (Table 1), compared to the value at 74 MeV of $N = 1.14$ used in Fig. 26.

4.7. Summary

In summary, the M3Y interaction in a folding model is quite successful (with the exception of ^6Li) in predicting the real parts of nucleus-nucleus potentials. Further, it shows promise of giving a reasonable description of

nucleon and alpha scattering. It may be that we need a better treatment of the exchange terms. It would also be more satisfactory to use an explicitly density- and energy-dependent effective interaction [54] instead of the M3Y averaged one. Nonetheless, I believe that this work indicates that it is worthwhile to pursue the goal of a simple, unified description of these scattering processes.

Appendix: Barrier Penetration and Reflection Effects

The WKB treatment of potential scattering can be expressed in terms of radial action integrals of the type

$$S(r_1,r_2) = \int_{r_1}^{r_2} \left[\frac{2\mu}{\hbar^2}\left\{E-U_{tot}(r)\right\}\right]^{1/2} dr, \tag{A.1}$$

where $U_{tot} = U_N + U_c + U_L$ is the sum of nuclear, Coulomb and centrifugal potentials and r_1, r_2 are zeros of the integrand (i.e., the classical turning points); r_2 may also be 'infinity' (i.e., some value of r for which U_N becomes negligible). The simplest WKB approximation describes reflection from the outermost turning point at $r = r_B$, giving a nuclear phase shift for this partial wave

$$\delta^{(o)} = S(r_B,\infty) - S_c(r_B,\infty) \tag{A.2}$$

where the Coulomb S_c is obtained by putting $U_N = 0$. (For simplicity, we do not label the partial wave L explicitly.) The S-matrix element is given by $\eta = e^{2i\delta}$. (Here we use the notation η instead of S to avoid confusion with the action integral.)

Near the top of the barrier, quantal penetration effects become important and modify the expression (A.2). They can be included in a factor N [38] so that for example the S-matrix element for reflection from the outer barrier can be written

$$\eta \simeq \frac{e^{2i\delta^{(o)}}}{N}. \tag{A.3}$$

When the total $U_{tot}(r)$ has a 'pocket' (like Fig. 10) and E is below the top of the outer barrier but above the bottom of the pocket, there are three turning points for real potentials. If U_N is complex, the WKB theory may be generalized by analytically continuing into the complex plane; then there are always 3 or more turning points r_i which are complex. The expressions for the S-matrix become more complicated but can be written in the physically transparent form

$$\eta = \eta_B + \eta_I. \tag{A.4}$$

Here η_B can be identified as the amplitude of the wave reflected from the outermost turning point (B = barrier), while η_I is the amplitude of the wave resulting from reflection at the innermost turning point associated with the centrifugal barrier (I = internal). The barrier wave amplitude η_B can be written in the form (A.3). The internal wave amplitude η_I is affected by the degree of penetration through the outer barrier, the amount of absorption in the interior and the possibility of multiple reflections (and quasi-bound states) within any pocket in U_{tot}.

If the absorption is very weak and there is a potential pocket, multiple reflections will occur for E below the outer barrier and above the bottom of the pocket. If the energy is such that the internal wave just 'fits' into the pocket, a resonance occurs. It has been suggested [69] that this is seen in $^{16}O + ^{12}C$ scattering. Mostly the absorption is too strong and multiple reflections do not occur [43]. At the other extreme, if the absorption is strong, the inner wave is completely damped out, $\eta_I \to 0$ and $\eta \approx \eta_B$. The magnitude of η_I for low partial waves may be estimated from mean free path arguments. For example, for the S-wave we have

$$|\eta_I| \approx e^{-R/\Lambda} \tag{A.5}$$

where R is a measure of the size of the absorptive region and Λ is the local mean free path,

$$\Lambda = \frac{\hbar^2 K}{2\mu W} \quad , \quad K^2 = \frac{2\mu}{\hbar^2}\,[E-\mathrm{Re}U_N(0)-U_c(0)]. \tag{A.6}$$

Here K is the local wavenumber at r = 0 and W is the imaginary potential strength. If further the absorption is strong enough at the outer barrier itself, $N \to 1$ and $\eta_B \to \eta_B^{(o)}$, the simple WKB value from Eq. (A.2). There are intermediate situations in which both η_B and η_I play a rôle; some were discussed in the text; even small values of η_I can produce relatively large effects at large angles, $\theta \sim \pi$ (for example, see Figs. 12 and 13).

We may distinguish two kinds of this intermediate situation. In one, η_I is significant for all the low-L partial waves ('low-L' meaning L values less than the grazing value); the $\alpha + ^{40}Ca$ case of Fig. 13 is an example. In the other kind of situation we have a kind of 'surface transparency'; a group of partial waves with L around and just below the grazing value are weakly absorbed, while those with small L are strongly absorbed. Then $|\eta_I(L)|$ is

peaked near the grazing L. This behaviour is somewhat like that of a Regge pole.

Surface transparency can be obtained in two ways, although the underlying physics is quite different [43,69]. In one way, we restrict the radial extent of the imaginary potential by letting it have a smaller radius and/or diffuseness than the real potential, but keep the imaginary strength large enough to strongly absorb any waves penetrating it. Then $|\eta_I| \approx 0$ for small L. In this case the η_I arise primarily from reflection at the surface of the imaginary potential which is now inside the barrier due to the real potential.

The other way is to use an L-dependent imaginary potential, for example

$$\mathrm{Im}U(r,L) = -\frac{W_o(r)}{1 + \exp\left(\frac{L-L_c}{\Delta}\right)}, \tag{A.7}$$

where usually the cut-off L_c is near or just below the grazing value. This also reduces the absorption of the surface waves compared to the lower-L waves. However, the surface waves are now exposed to a weakly absorbing potential over all r, not just in the surface, so that now η_I for these waves <u>does</u> come from reflection at the inner, centrifugal, barrier. We still have $\eta_I \approx 0$ for the lower-L waves.

References

[1] K. W. Ford and J. A. Wheeler, Ann. Phys. 7 (1959) 259.

[2] R. A. Broglia, S. Landowne, R. A. Malfliet, V. Rostokin, and A. Winther, Phys. Repts. 11C (1974) 1.

[3] T. Koeling and R. A. Malfliet, Phys. Repts. 22C (1975) 181.

[4] J. Knoll and R. Schaeffer, Ann. Phys. 97 (1976) 307.

[5] S. Landowne, C. H. Dasso, B. S. Nilsson, R. A. Broglia, and A. Winther, Nucl. Phys. A259 (1976) 99.

[6] K. W. McVoy, Notas de fisica (Universidad Nacional Autonoma de Mexico) 1 (1978) No. 4.

[7] W. E. Frahn and D. H. E. Gross, Ann. Phys. 101 (1976) 520.

[8] W. E. Frahn and K. E. Rehm, Phys. Repts. 37C (1978) 1.

[9] S. K. Kauffmann, Z. Physik A282 (1977) 163; W. E. Frahn, to be published.

[10] J. B. Ball, et al., Nucl. Phys. A252 (1975) 208.

[11] H. Rebel, et al., to be published.

[12] D. A. Goldberg, S. M. Smith, and G. F. Bardzik, Phys. Rev. C10 (1974) 1362.

[13] D. A. Goldberg and S. M. Smith, Phys. Rev. Lett. 33 (1974) 715; see also Goldberg in [23].

[14] D. G. Kovar, Proc. Sym. on Macroscopic Features of Heavy-Ion Collisions, Hakone, Japan (1977).

[15] W. U. Schroder and J. R. Huizenga, Ann. Revs. Nucl. Sci. 27 (1977) 465.

[16] P. R. Christensen and A. Winther, Phys. Lett. 65B (1977) 19.

[17] D. A. Goldberg, Phys. Lett. 55B (1975) 59; A. Budzanowski, et al., Phys. Rev. C17 (1978) 951.

[18] G. R. Satchler, Nucl. Phys. A279 (1977) 493.

[19] G. R. Satchler, Proc. Conf. on Reactions between Complex Nuclei, Nashville, Tn., 1974 (North-Holland Publishing Co., 1974).

[20] W. Henning, et al., Phys. Rev. C15 (1977) 292; H. Wojciechowski, et al., Phys. Rev. C17 (1978) 2126.

[21] J. Blocki, J. Randrup, W. J. Swiatecki, and C. F. Tsang, Ann. Phys. 105 (1977) 427.

[22] D. M. Brink, European Conf. on Nucl. Phys. with Heavy Ions, Caen, 1976, J. de Phys. C-5 (1976) 47.

[23] R. M. DeVries, editor: Proc. Sym. Heavy Ion Elastic Scattering,

University of Rochester (1977).

[24] H. Feshbach, Ann. Phys. 19 (1967) 287.

[25] J. Fleckner and U. Mosel, Nucl. Phys. A277 (1977) 170.

[26] U. Mosel, Particles & Nuclei 3 (1972) 297.

[27] W. G. Love, T. Terasawa, and G. R. Satchler, Nucl. Phys. A291 (1977) 183.

[28] C. Ngô, et al., Nucl. Phys. A252 (1975) 237; D. M. Brink and Fl. Stancu, Nucl. Phys. A299 (1978) 321.

[29] J. Fleckner and U. Mosel, Nucl. Phys. A277 (1977) 170.

[30] J. R. Birkelund and J. R. Huizenga, Phys. Rev. C17 (1978) 126.

[31] R. Bass, Nucl. Phys. A231 (1974) 45; K. Siwek-Wilczynska and J. Wilczynski, Phys. Lett. 74B (1978) 313.

[32] H. J. Krappe, in Proc. Intern. Workshop on Gross Properties of Nuclei VI, Hirschegg, Austria, 1978 (Publication AED-Conf 78-007-014).

[33] R. H. Siemssen, in Nuclear Spectroscopy and Reactions, Part B (Academic Press, New York, 1974); R. H. Siemssen, in Proc. Int. Conf. on Resonances in Heavy-Ion Reactions, Hvar, Yugoslavia, 1977 (North-Holland Publishing Co., to be published).

[34] J. G. Cramer, et al., Phys. Rev. C14 (1976) 2158.

[35] G. R. Satchler, Nucl. Phys. A279 (1977) 493.

[36] V. Shkolnik, et al., Phys. Lett. 74B (1978) 195.

[37] P. Braun-Munzinger, et al., Phys. Rev. Lett. 38 (1977) 944.

[38] D. M. Brink and N. Takigawa, Nucl. Phys. A279 (1977) 159; N. Takigawa and S. Y. Lee, Nucl. Phys. A292 (1977) 173.

[39] F. Michel and R. Vanderpoorten, Phys. Rev. C16 (1977) 142.

[40] H. P. Gubler, et al., Phys. Lett. 74B (1978) 202.

[41] W. G. Love, Phys. Rev. C17 (1978) 1876.

[42] Th. Delhar, et al., Phys. Rev. C (Sept., 1978).

[43] S. Y. Lee, N. Takigawa, and C. Marty, "Semiclassical Study of Heavy-Ion Optical Potentials", submitted to Nucl. Phys. A.

[44] R. M. Wieland, et al., Phys. Rev. Lett. 37 (1976) 1458, and to be published.

[45] N. Rowley, H. Doubre, and C. Marty, "Low Partial Waves in $^{12}C + ^{12}C$ Elastic Scattering", to be published.

[46] G. R. Satchler and W. G. Love, Phys. Lett. 76B (1978) 23.

[47] D. A. Goldberg, Phys. Lett. 55B (1975) 59;

A. Budzanowski, et al., Phys. Rev. C17 (1978) 951.

[48] G. R. Satchler, Phys. Lett. 59B (1975) 121.

[49] L. D. Rickertsen and G. R. Satchler, Phys. Lett. 66B (1977) 9.

[50] W. G. Love, Phys. Lett. 72B (1977) 4; F. Petrovich, D. Stanley, and J. J. Bevelacqua, Phys. Lett. 71B (1977) 259.

[51] E. C. Halbert and G. R. Satchler, Nucl. Phys. A233 (1974) 265; G. R. Satchler, Zeit. f. Physik 260 (1973) 209.

[52] P. J. Moffa, C. B. Dover, and J. P. Vary, Phys. Rev. C16 (1977) 1857.

[53] G. Bertsch, et al., Nucl. Phys. A284 (1977) 399.

[54] J. P. Jeukenne, A. Lejeune, and C. Mahaux, Phys. Rev. C16 (1977) 80; F. A. Brieva and J. R. Rook, Nucl. Phys. A291 (1977) 317.

[55] V. A. Madsen, in Nuclear Spectroscopy and Reactions, Part D (Academic Press, New York, 1975).

[56] G. R. Satchler, et al., Nucl. Phys. A298 (1978) 313.

[57] W. G. Love and G. R. Satchler, Nucl. Phys. A159 (1970) 1.

[58] G. E. Brown, Unified Theory of Nuclear Models and Forces (North-Holland Publishing Co., 1967).

[59] G. R. Satchler and W. G. Love, Phys. Lett. 65B (1976) 415.

[60] L. J. B. Goldfarb, Nucl. Phys. A301 (1978) 497.

[61] Y. Eisen and B. Day, Phys. Lett. 63B (1976) 253.

[62] D. E. Bainum, et al., Phys. Rev. C16 (1977) 1377; W. G. Love, Phys. Rev. C15 (1977) 1261.

[63] W. G. Love and L. W. Owen, Nucl. Phys. A239 (1975) 74.

[64] M. Golin, F. Petrovich, and D. Robson, Phys. Lett. 64B (1976) 253.

[65] B. Buck, H. Friedrich, and C. Wheatley, Nucl. Phys. A275 (1977) 246.

[66] G. R. Satchler and W. G. Love, Phys. Lett. 76B (1978) 23.

[67] W. G. Love and G. R. Satchler, to be published.

[68] J. W. Negele, Phys. Rev. C1 (1970) 1260; C9 (1974) 1054.

[69] N. Takigawa, S. Y. Lee, and C. Marty, Phys. Lett. 76B (1978) 187.

[70] R. Bass, Phys. Rev. Lett. 39 (1977) 265.

[71] U Mosel, in Heavy Ion Collisions (ed. R. Bock: North Holland Publishing Co., Amsterdam, 1978).

Table 1. Heavy-ion scattering using a folded real potential based upon the M3Y interaction. The potential is multiplied by N and N is varied to optimise the fit to the data.

System	Energy (MeV)	N	System	Energy (MeV)	N
$^{40}Ca + ^{40}Ca$	130-240	1.32	$^{16}O + ^{28}Si$	142	0.91
$^{32}S + ^{48}Ca$	83	1.09	$^{16}O + ^{28}Si$	215	0.76
$^{32}S + ^{40}Ca$	100	1.26	$^{16}O + ^{28}Si$	81	1.00
$^{32}S + ^{32}S$	91	1.22	$^{16}O + ^{28}Si$	72	1.00
$^{32}S + ^{27}Al$	100	1.06	$^{16}O + ^{28}Si$	66	1.01
$^{16}O + ^{208}Pb$	313	1.05	$^{16}O + ^{28}Si$	60	1.01
$^{16}O + ^{208}Pb$	192	0.95	$^{16}O + ^{28}Si$	53	1.00
$^{16}O + ^{208}Pb$	130	1.16	$^{16}O + ^{28}Si$	38	1.01
$^{16}O + ^{88}Sr$	59	1.22	$^{16}O + ^{12}C$	168	1.11
$^{16}O + ^{88}Sr$	56	1.21	$^{15}N + ^{89}Y$	50	1.18
$^{16}O + ^{88}Sr$	52	1.19	$^{14}N + ^{16}O$	154	1.30
$^{16}O + ^{88}Sr$	48	1.36	$^{14}N + ^{12}C$	156	1.03
$^{16}O + ^{60}Ni$	142	1.00	$^{13}C + ^{207}Pb$	86	1.27
$^{16}O + ^{60}Ni$	61	1.04	$^{12}C + ^{208}Pb$	116	1.26
$^{16}O + ^{59}Co$	142	1.00	$^{12}C + ^{208}Pb$	96	1.25
$^{16}O + ^{59}Co$	56	1.00	$^{12}C + ^{142}Nd$	70	1.15
$^{16}O + ^{59}Co$	52	0.99	$^{12}C + ^{90}Zr$	98	0.98
$^{16}O + ^{59}Co$	49	1.10	$^{12}C + ^{40}Ca$	45	1.14
$^{16}O + ^{59}Co$	46	0.87	$^{12}C + ^{28}Si$	132, 186	0.97
$^{16}O + ^{59}Co$	40	0.98	$^{12}C + ^{28}Si$	40	1.02
$^{16}O + ^{48}Ca$	56	0.98	$^{12}C + ^{12}C$	70-126	1.01-1.13
$^{16}O + ^{40}Ca$	214	1.05	$^{11}B + ^{209}Bi$	75	1.45
$^{16}O + ^{40}Ca$	140	1.23	$^{11}B + ^{208}Pb$	72	1.26
$^{16}O + ^{40}Ca$	104	0.99	$^{10}B + ^{16}O$	99	1.04
$^{16}O + ^{40}Ca$	74	1.14			
$^{16}O + ^{40}Ca$	56	1.27	Average		1.09 ± 0.13

Figure Captions

Fig. 1. Some typical angular distributions for strong absorption elastic scattering: (a) a Fraunhofer-like diffraction pattern [11] (b) a Fresnel-like diffraction pattern [10], (c) scattering of 140-MeV alphas from several targets [12].

Fig. 2. Sensitivity of Fresnel-type angular distributions to (a) the imaginary potential [10] and (b) the real potential [67]. (In (b), N multiplies a folded real potential; see text.)

Fig. 3. Overlap of the nuclei at the critical or strong absorption radius (here about 12.5 fm) [10]. (a) Densities along the line joining the nuclear centers. (b) Nuclear (U_N), Coulomb (U_c) and centrifugal (U_L) potentials. The U_N is the folded potential used for Fig. 1(b). Also shown is U_N flattened for $r \leq 11$ fm; the scattering for this potential is also shown in Fig. 1(b).

Fig. 4. Interaction energy of $^{90}Zr + ^{208}Pb$ calculated using an energy-density approach and a Skyrme force [28] (solid curve). The points are the proximity potential, Eqs. (27)-(29). The crosses are for a modified proximity form.

Fig. 5. Magnitudes of the S-matrix elements for $^{16}O + ^{18}O$ at several c.m. energies. The solid curves fit the data, the dashed curves are for a strongly absorbing potential [33]. (S_L is here denoted η_L.)

Fig. 6. Potential fits to $^{16}O + ^{28}Si$ data, one shallow Woods-Saxon [34] and one deep folded potential [35], both strongly absorbing.

Fig. 7. Showing the forward angle oscillations in ^{16}O + Si isotopes and potential fits ([36] and Dehnard in [23]).

Fig. 8. Large-angle oscillations in $^{16}O + ^{28}Si$ [37] and a simple potential fit (Dehnard in [23]).

Fig. 9. Typical S-matrix elements for potential scattering. (E-18 is the potential used in Fig. 6.)

Fig. 10. Total real potential (sum of nuclear, Coulomb and centrifugal) for 'shallow' E-18 and for a deeper potential which fits the large-angle data (Dehnard in [23]).

Fig. 11. Large angle scattering for $\alpha + ^{40}Ca$. The solid curve is for a

phenomenological (Woods-Saxon)$^{2.65}$ potential [39], the dashed curve for a folded potential [41].

Fig. 12. Separate cross sections for reflection from outer (σ_B) and inner (σ_I) barriers and their combined effect (σ_{sc}) [38].

Fig. 13. S-matrix elements corresponding to Fig. 12 [38]. (Here $S_\ell = \eta_\ell$).

Fig. 14. Fits to $^{12}C + ^{12}C$ elastic scattering using a folded potential [44].

Fig. 15. Typical S-matrix elements corresponding to Fig. 14 [44] (here $S_L = \eta_L$).

Fig. 16. Some typical wave functions corresponding to Fig. 15 (solid curves) [44]. (Dashed curves are for a shallow Woods-Saxon potential which only fits the small-angle data.)

Fig. 17. Large-angle oscillations for $^{6}Li + ^{40}Ca$. The curves are for a folded potential, renormalized by N [66].

Fig. 18. Coordinates used in folding calculations.

Fig. 19. Folded potentials, using the M3Y interactions (a) from Eq. (48) and (b) from Eq. (49), near the strong absorption radius (here about 9.6 fm). The dots are obtained from scattering data. D stands for 'direct', E stands for 'exchange' (the contribution from the pseudopotential (51)), and D+E is their sum. (D+E is the same for the two potentials [59].)

Fig. 20. Combinations of volume integral and range needed to give a potential of -1.35 MeV at $D_{1/2}$ = 10.6 fm (Love in [23]).

Fig. 21. Folded potential at various separations R for Kr + Bi as the nuclear densities are cut off at na beyond the half-density points [67].

Fig. 22. Folded potential at 9.7 fm for various choices of density distributions for ^{16}O and ^{60}Ni plotted against the sum of their mean square radii [67].

Fig. 23. Scattering predicted using real folded potential (and M3Y interaction) plus Becchetti-Greenlees imaginary and spin-orbit terms [67].

Fig. 24. Some light heavy-ion scattering with the folded potential normalized as in Table 1 [67].

Fig. 25. Folded potential for $^{40}Ca + ^{40}Ca$ normalized as in Table 1 and obtained by fitting the data at 143.6 MeV [67].

Fig. 26. Folded potential for $^{16}O + ^{40}Ca$ obtained by fitting the data at 74 MeV (with N = 1.14) [67].

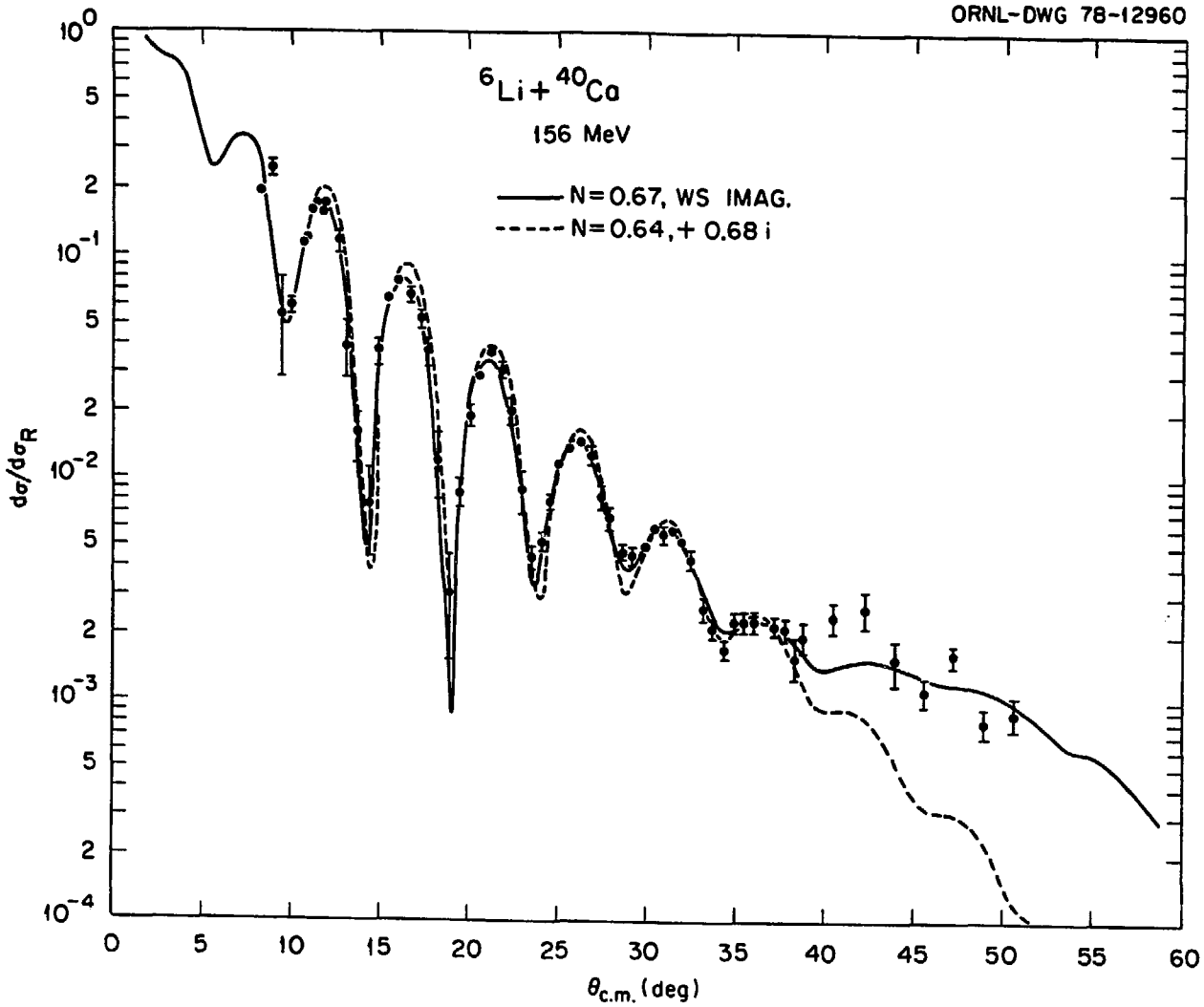
ORNL-DWG 78-12960
$^6Li + ^{40}Ca$
156 MeV
N=0.67, WS IMAG.
N=0.64, + 0.68 i
$d\sigma/d\sigma_R$
$\theta_{c.m.}$ (deg)

Fig. 1a

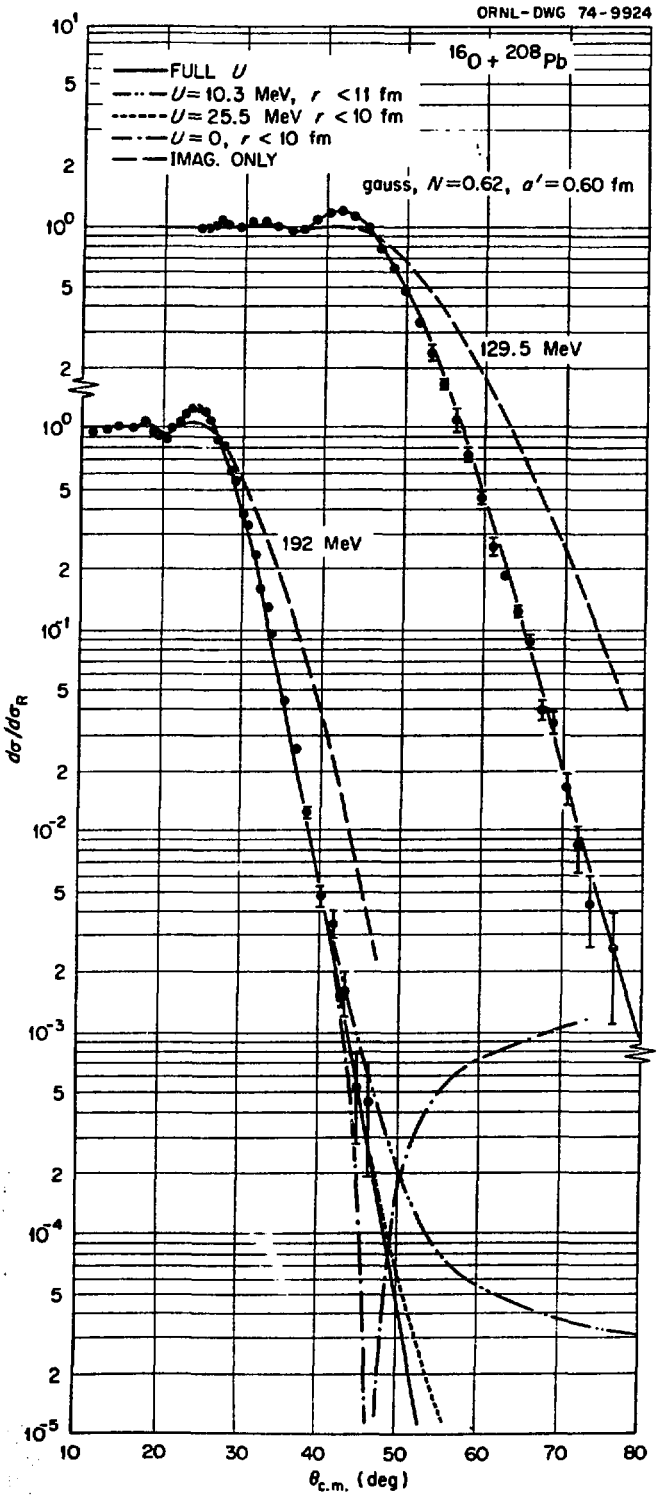
ORNL-DWG 74-9924
$^{16}O + ^{208}Pb$
FULL U
U = 10.3 MeV, r < 11 fm
U = 25.5 MeV r < 10 fm
U = 0, r < 10 fm
IMAG. ONLY
gauss, N = 0.62, a' = 0.60 fm
129.5 MeV
192 MeV
dσ/dσ_R
θ_c.m. (deg)

Fig. 1b

ORNL-DWG 78-17463

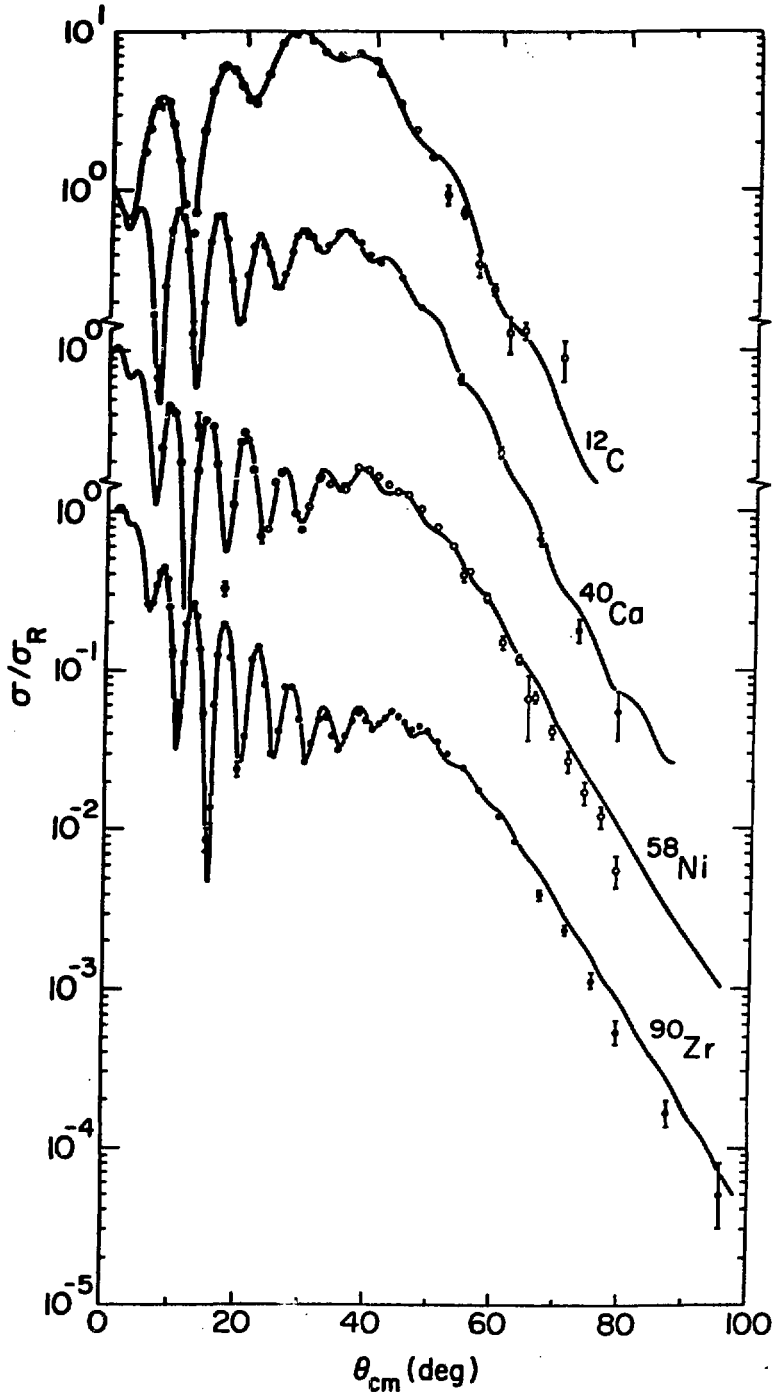

Fig. 1c

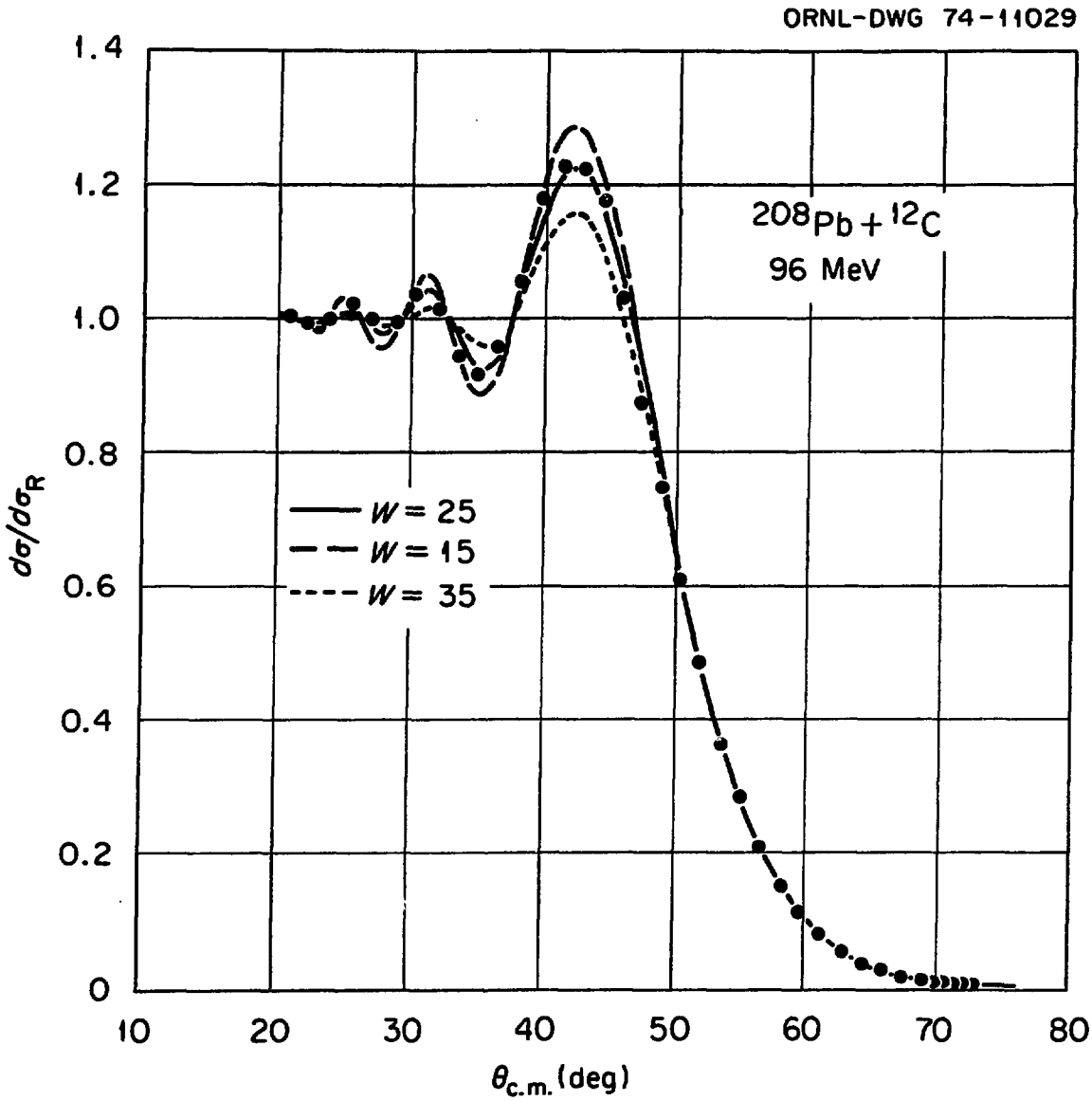
ORNL-DWG 74-11029
1.4
1.2
1.0
0.8
0.6
0.4
0.2
0
$d\sigma/d\sigma_R$
10
20
30
40
50
60
70
80
$\theta_{c.m.}$ (deg)
$^{208}Pb + ^{12}C$
96 MeV
W = 25
W = 15
W = 35

Fig. 2a

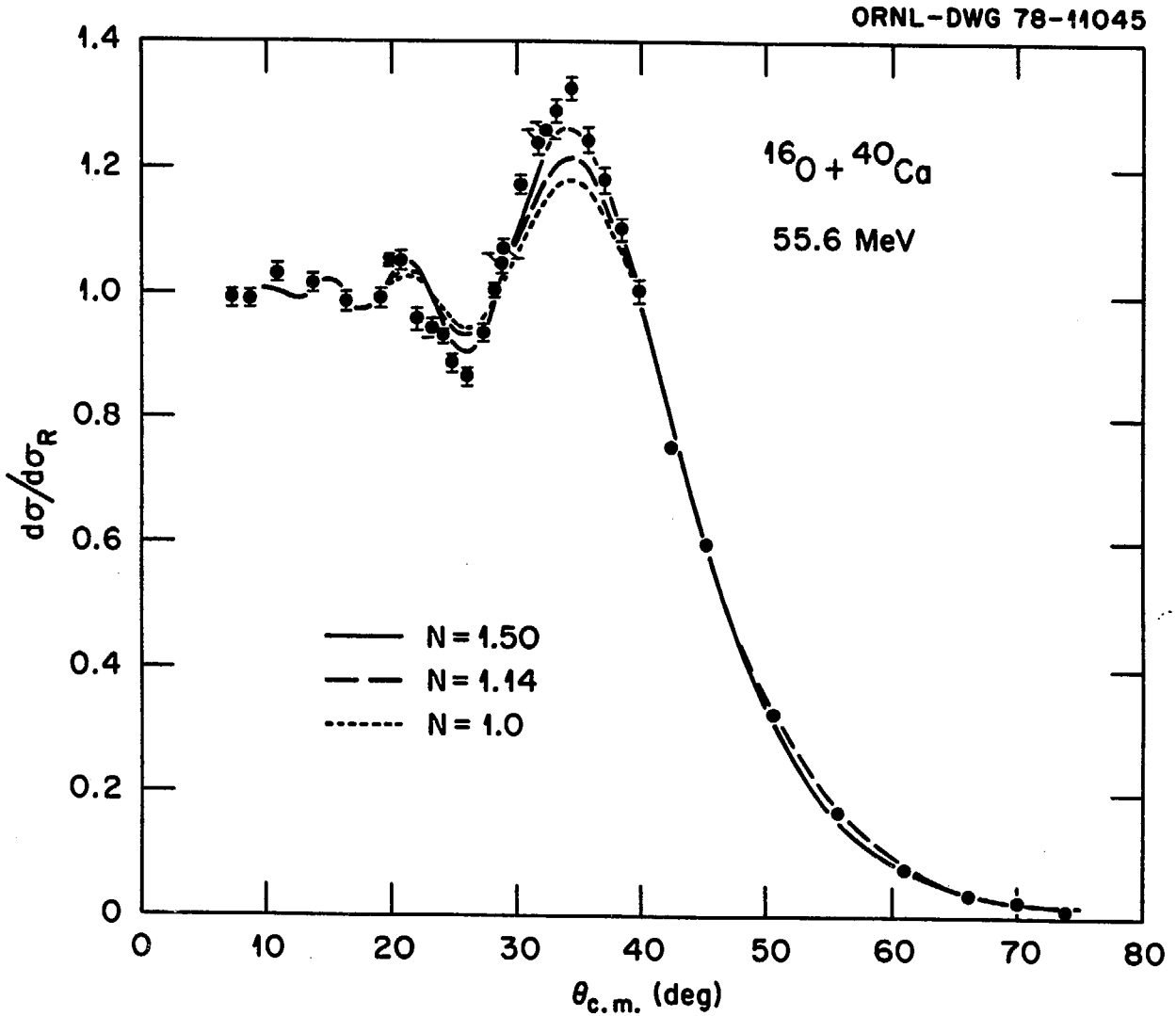
ORNL-DWG 78-11045
$^{16}O + ^{40}Ca$
55.6 MeV
N = 1.50
N = 1.14
N = 1.0
$d\sigma/d\sigma_R$
$\theta_{c.m.}$ (deg)
0
0.2
0.4
0.6
0.8
1.0
1.2
1.4
0
10
20
30
40
50
60
70
80

Fig. 2b

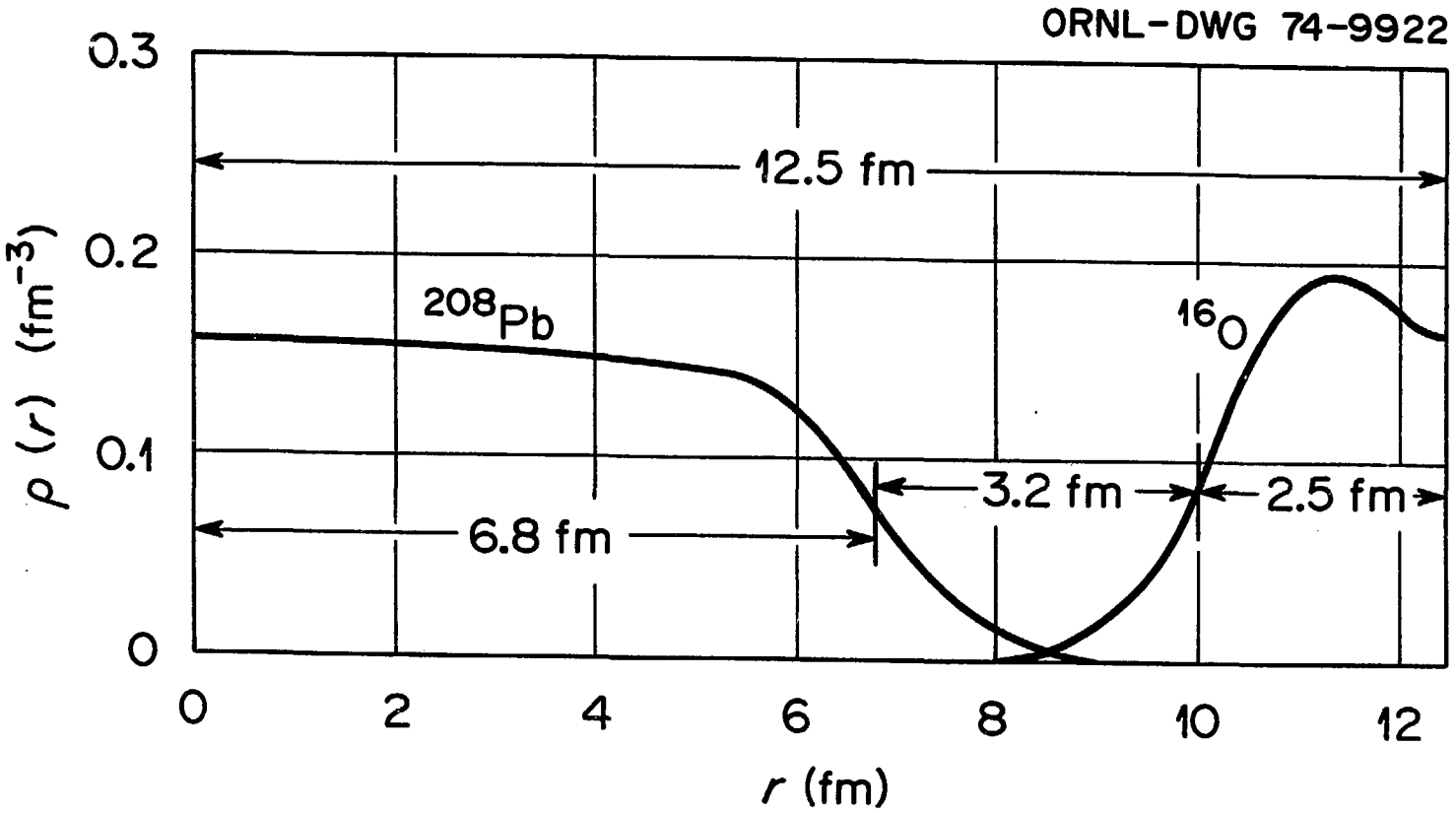
ORNL-DWG 74-9922
0.3
0.2
0.1
0
ρ (r) (fm⁻³)
12.5 fm
208Pb
16O
3.2 fm
2.5 fm
6.8 fm
0
2
4
6
8
10
12
r (fm)

Fig. 3a

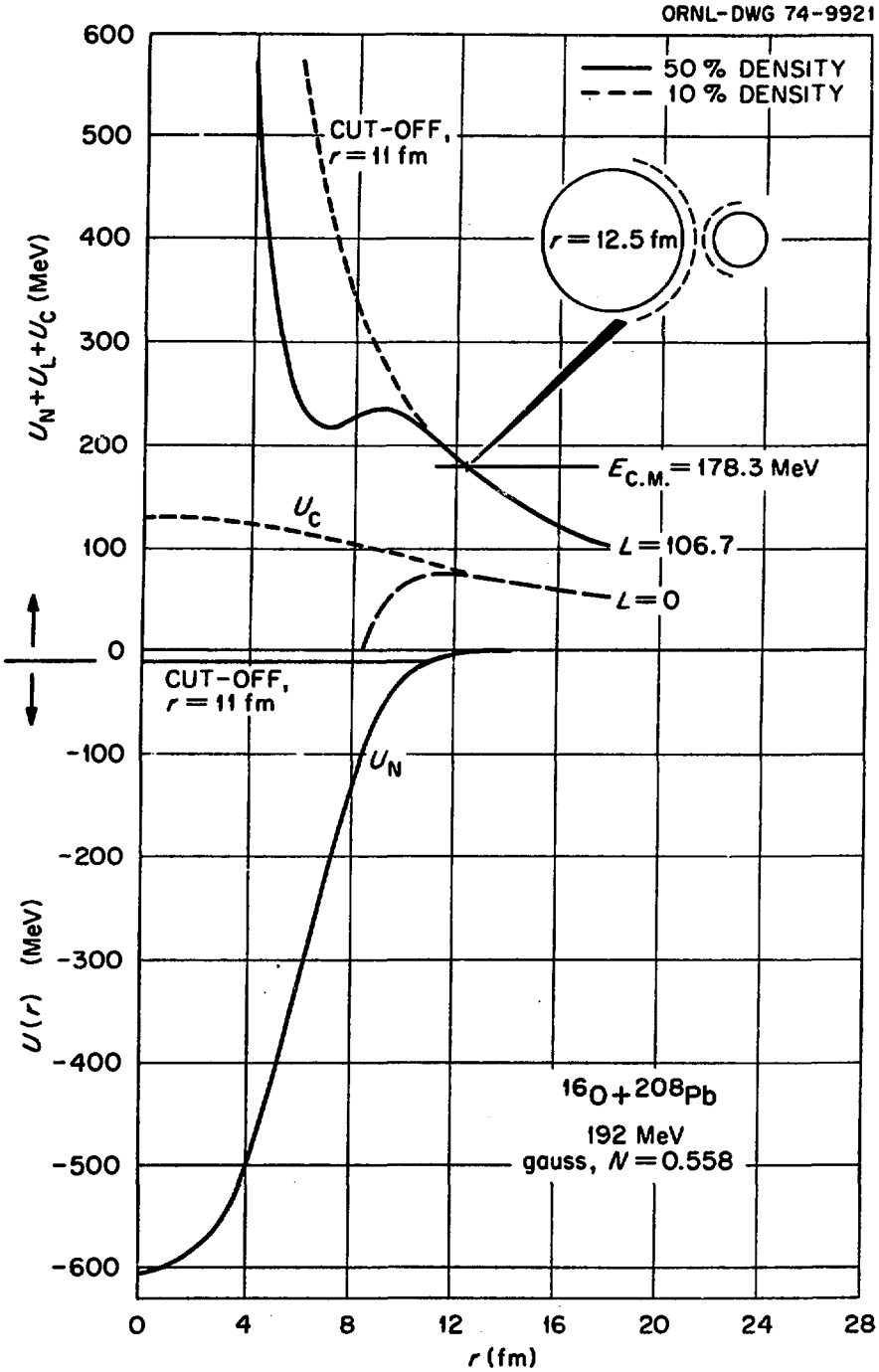
ORNL-DWG 74-9921
50 % DENSITY
10 % DENSITY
CUT-OFF, r = 11 fm
r = 12.5 fm
E C.M. = 178.3 MeV
U C
L = 106.7
L = 0
CUT-OFF, r = 11 fm
U N
16O + 208Pb
192 MeV
gauss, N = 0.558
U N + U L + U C (MeV)
U (r) (MeV)
r (fm)
600
500
400
300
200
100
0
-100
-200
-300
-400
-500
-600
0
4
8
12
16
20
24
28

Fig. 3b

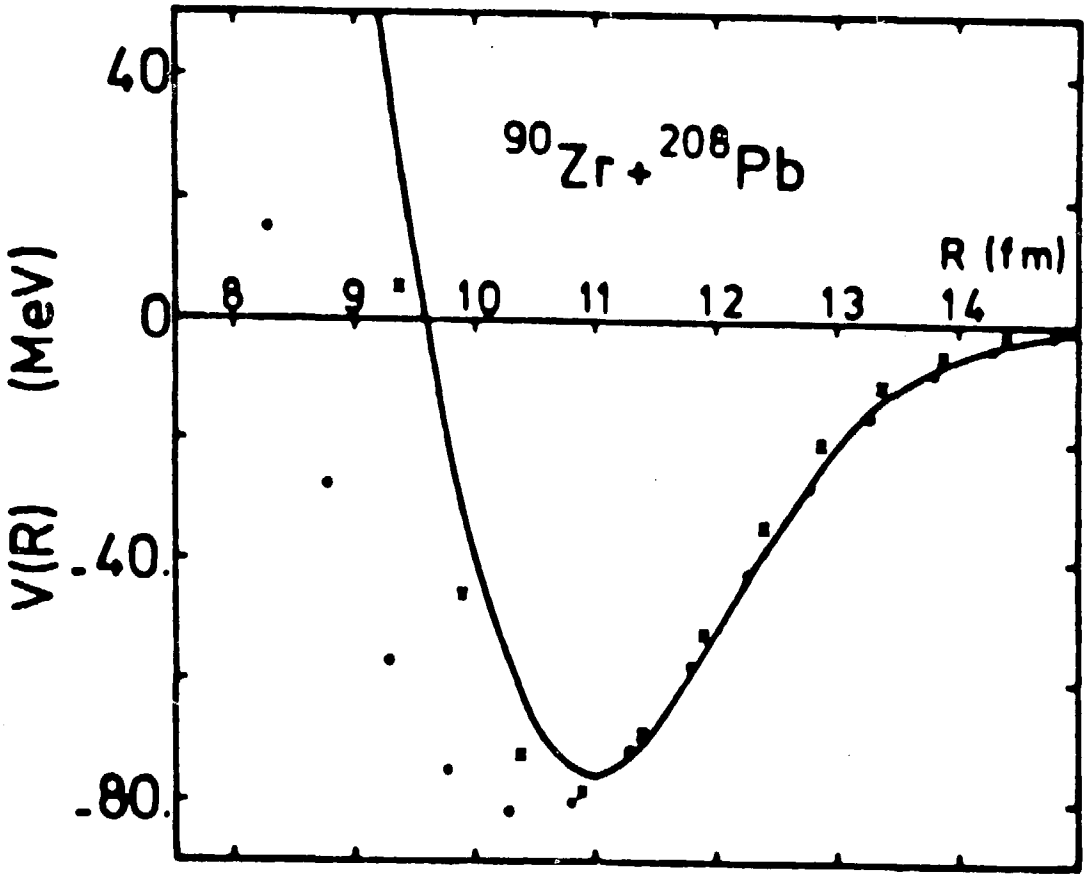

Fig. 4

ORNL-DWG 78-17465

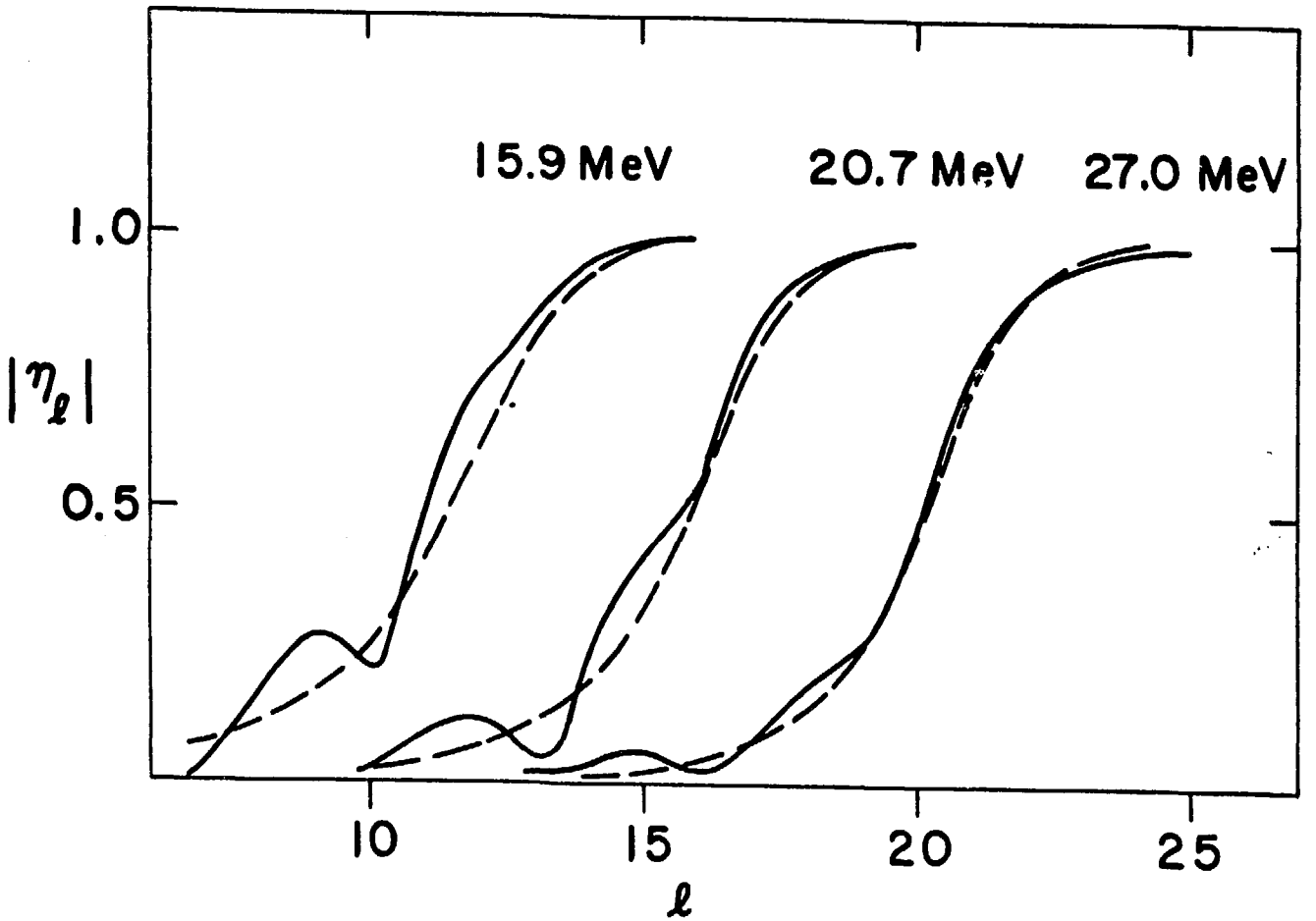

Fig. 5

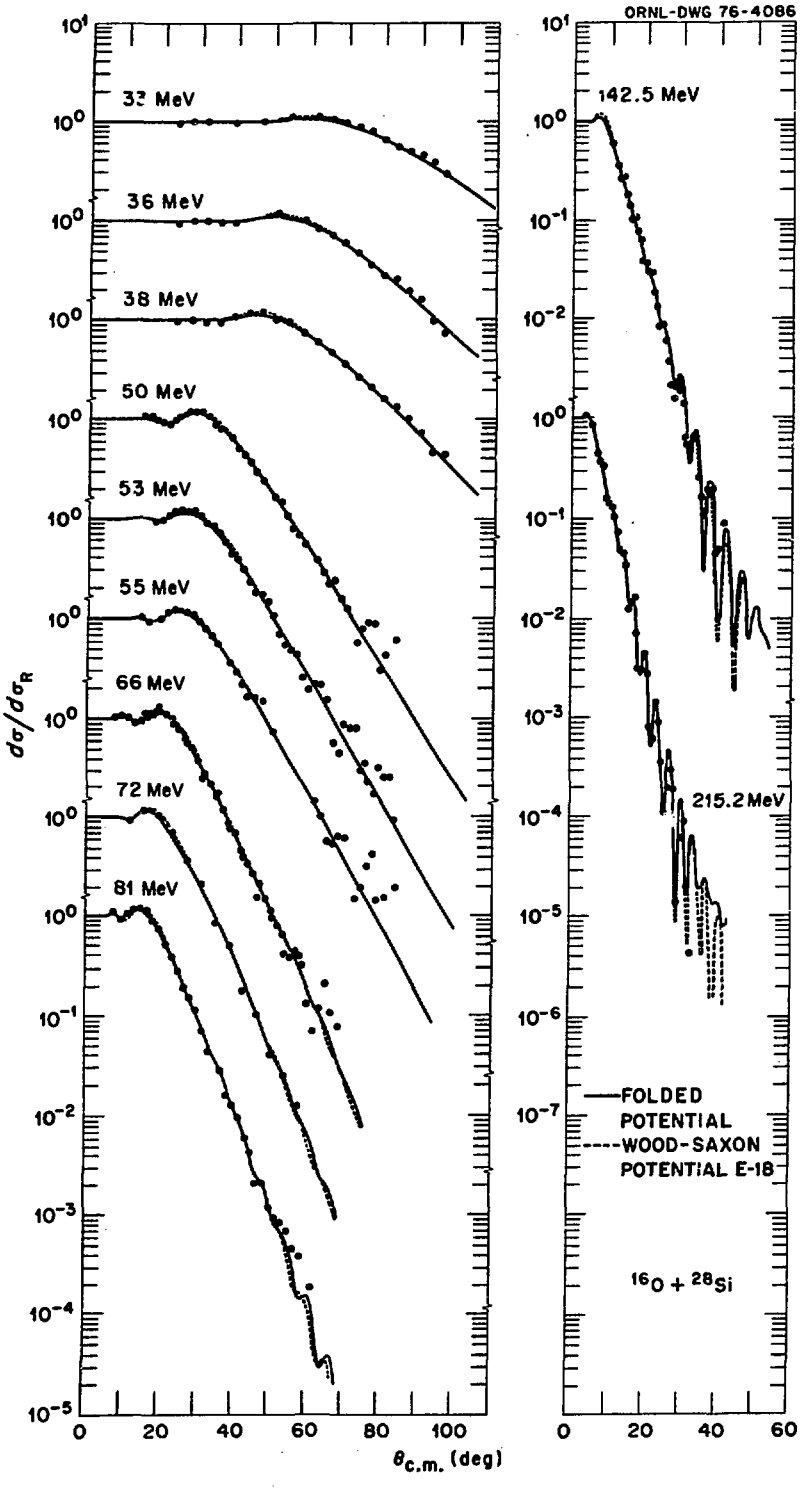
ORNL-DWG 76-4086
32 MeV
36 MeV
38 MeV
50 MeV
53 MeV
55 MeV
66 MeV
72 MeV
81 MeV
142.5 MeV
215.2 MeV
$d\sigma/d\sigma_R$
$\theta_{c.m.}$ (deg)
FOLDED POTENTIAL
WOOD-SAXON POTENTIAL E-18
$^{16}O + ^{28}Si$

Fig. 6

ORNL-DWG 78-17466

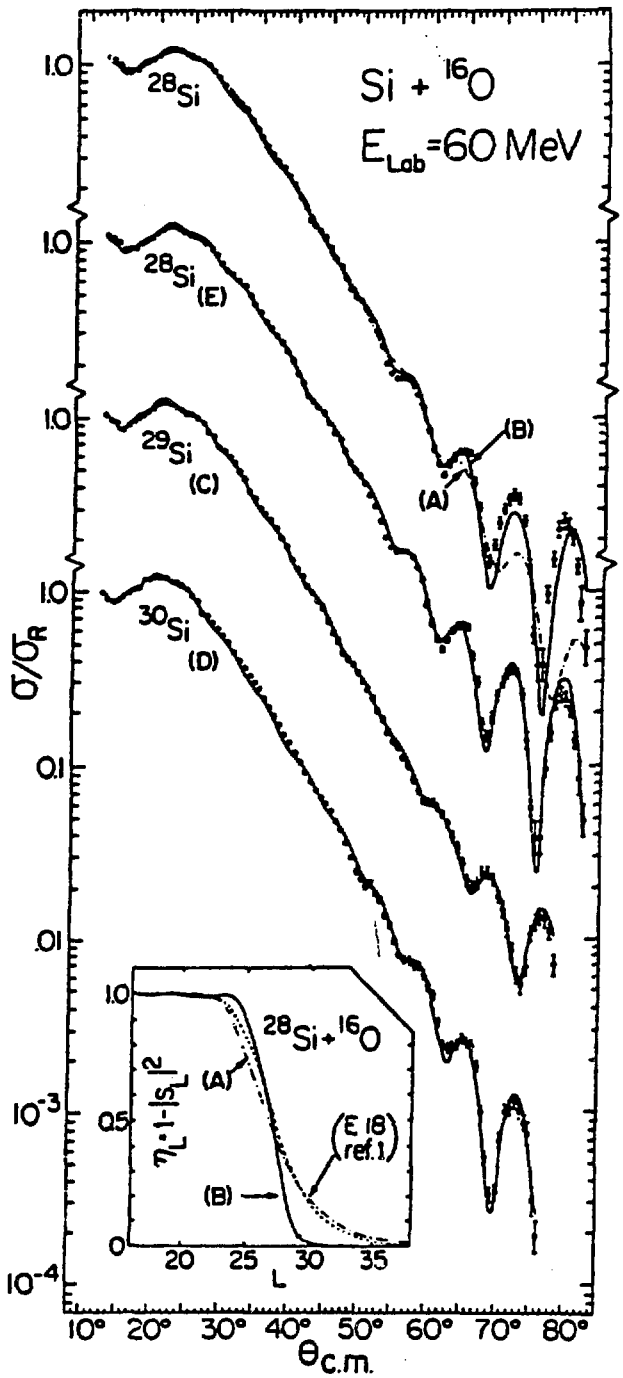

Fig. 7

ORNL-DWG 78-17467

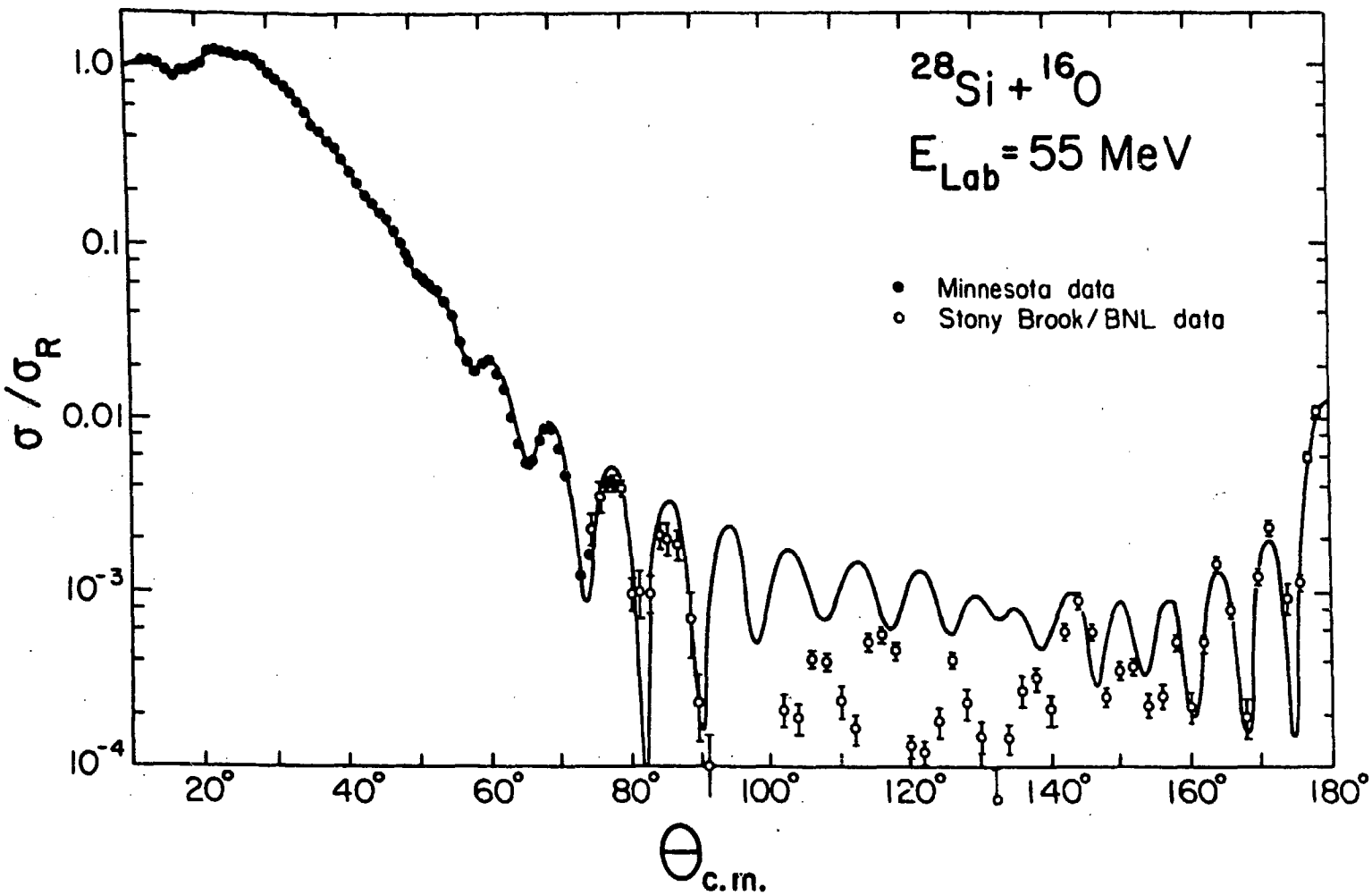

Fig. 8

ORNL-DWG 78-17468

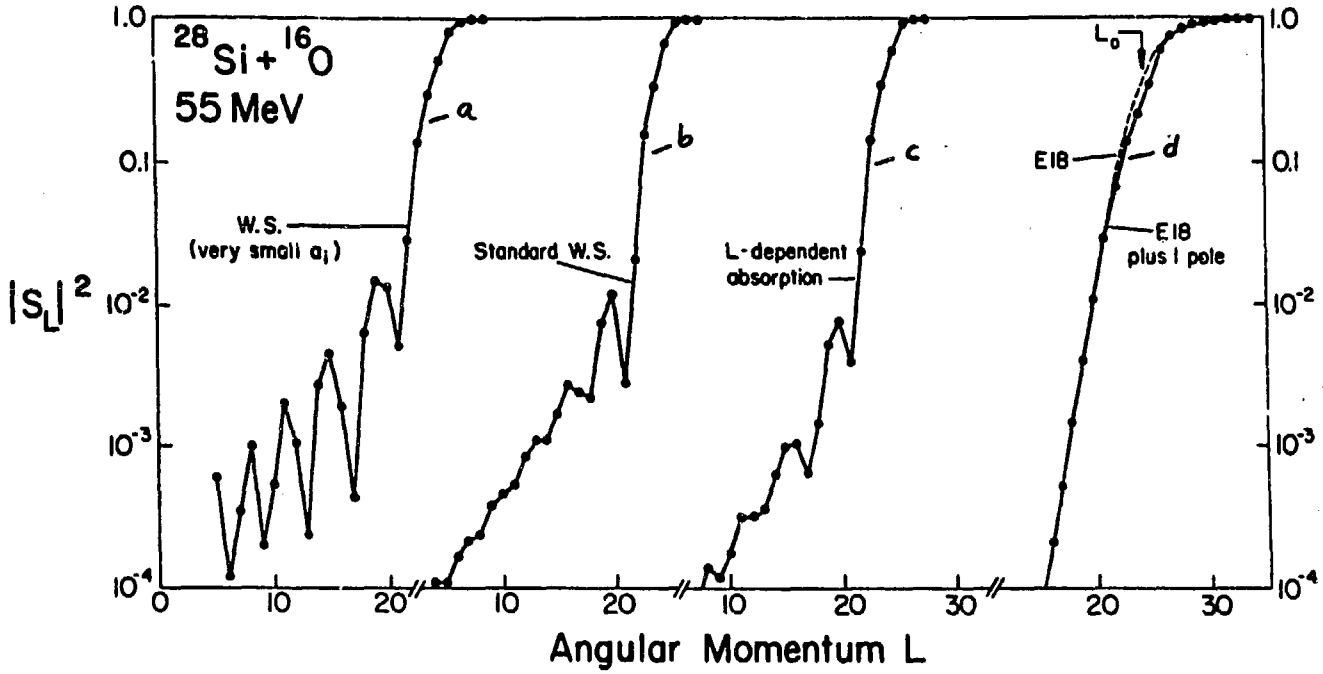

Fig. 9

ORNL-DWG 78-17469

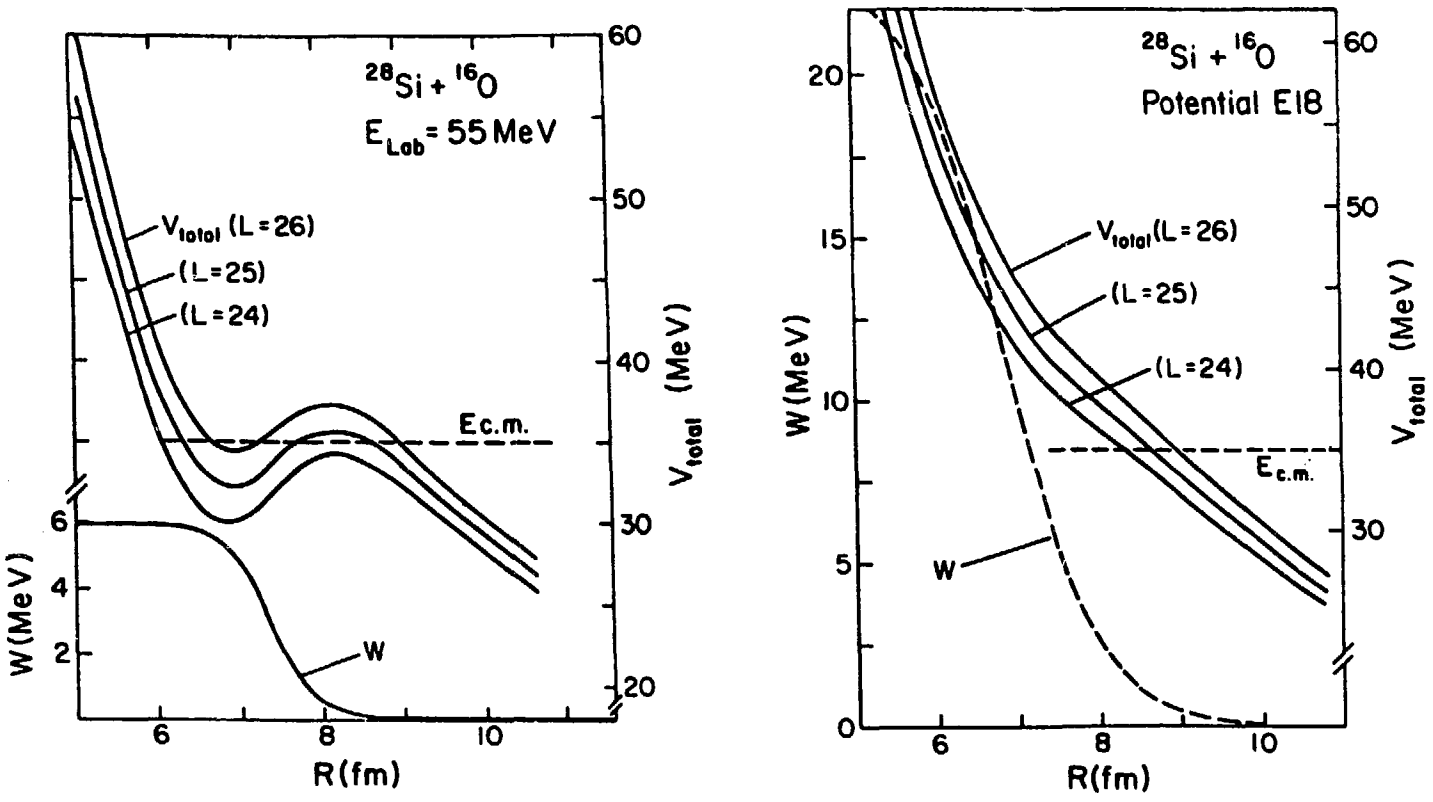

Fig. 10

ORNL-DWG 78-17470

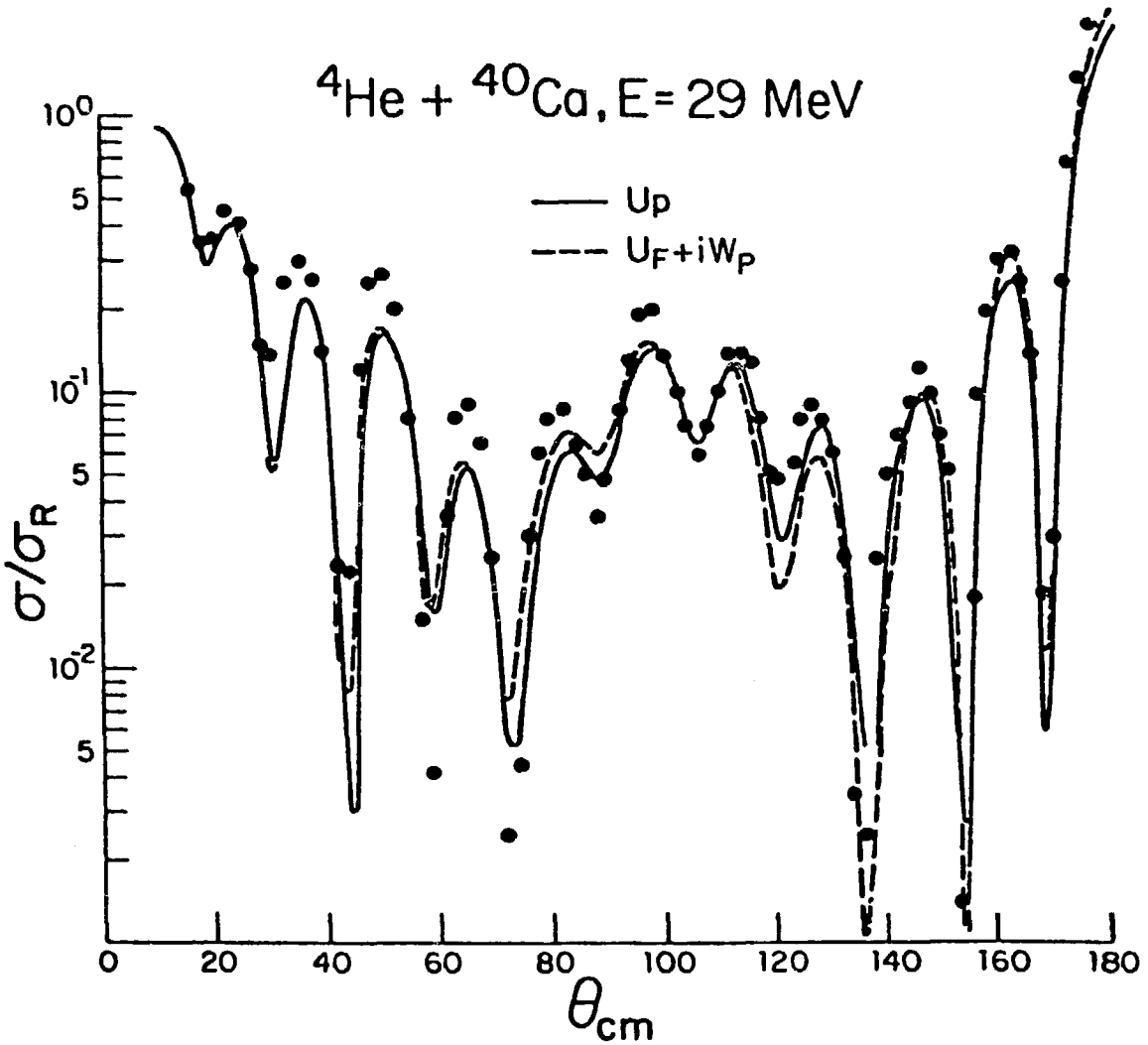

Fig. 11

ORNL-DWG 78-17472

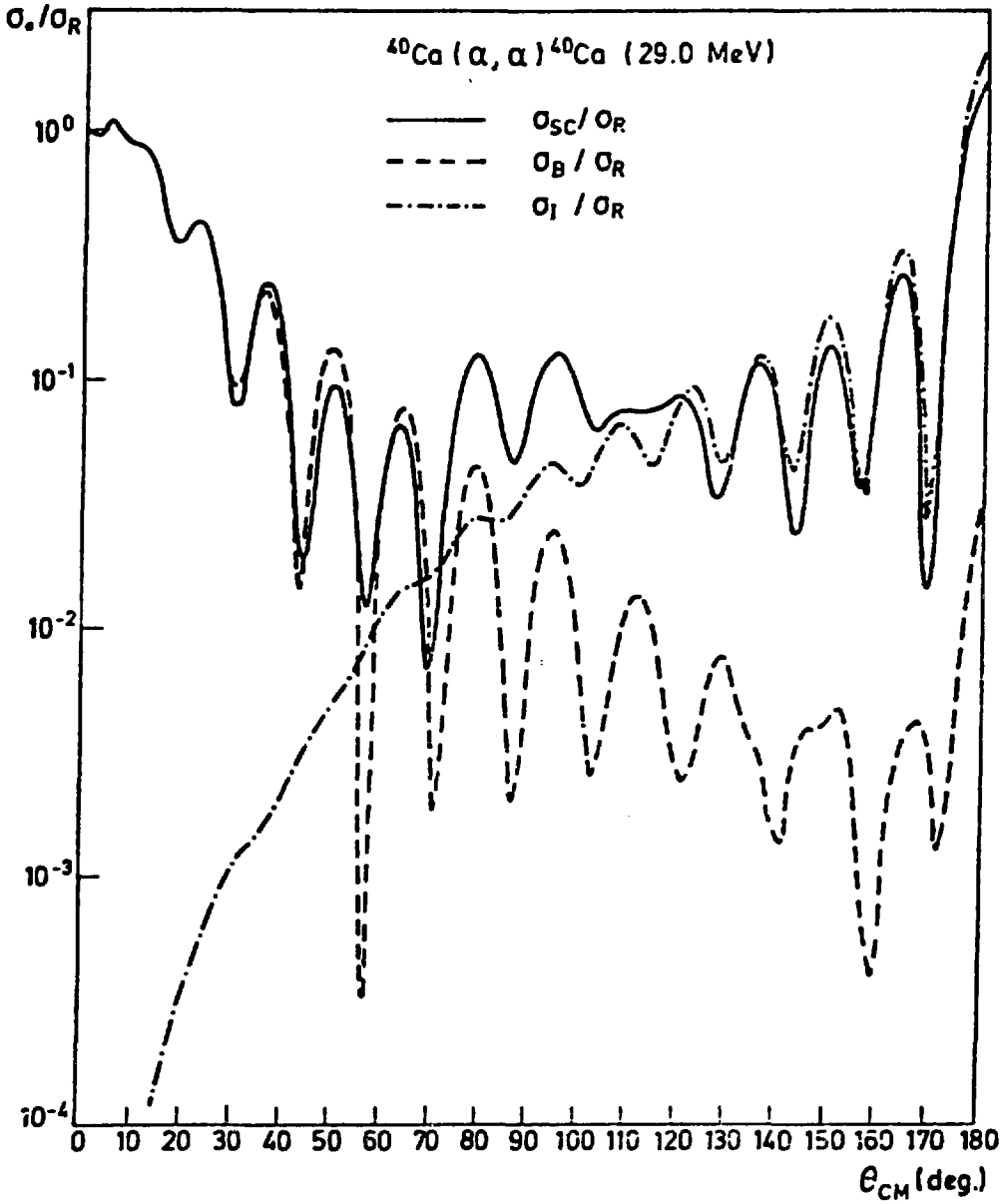

Fig. 12

ORNL-DWG 78-17471

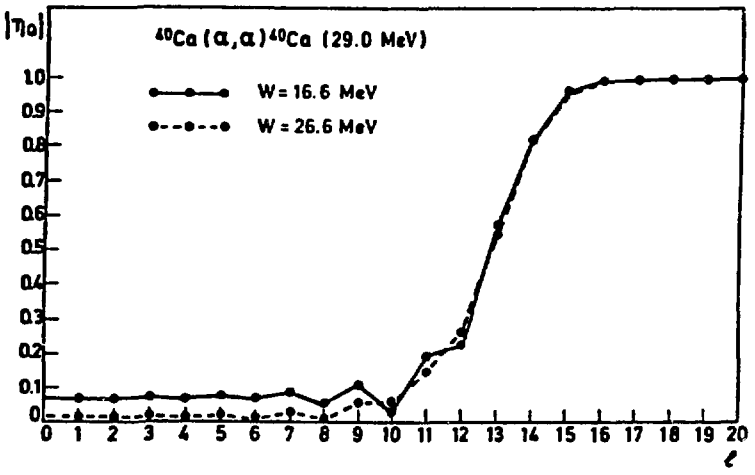

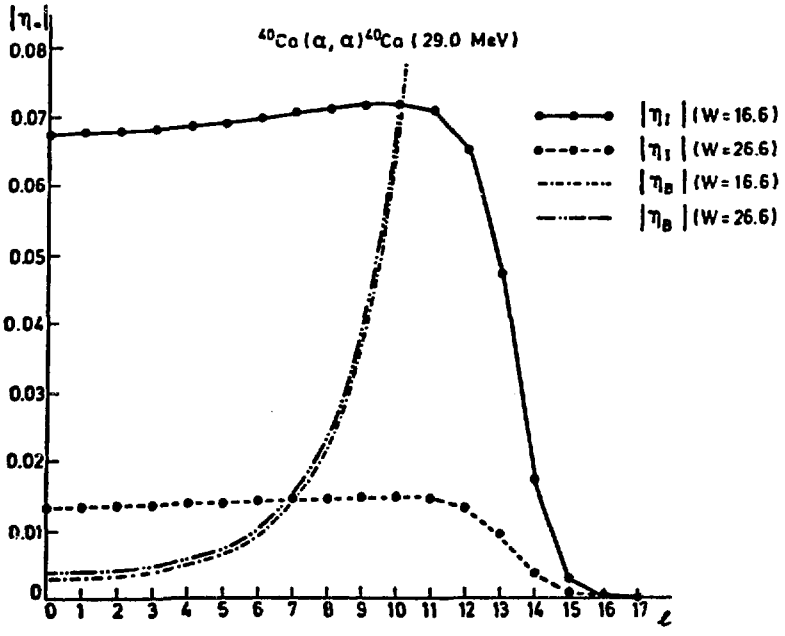

Fig. 13

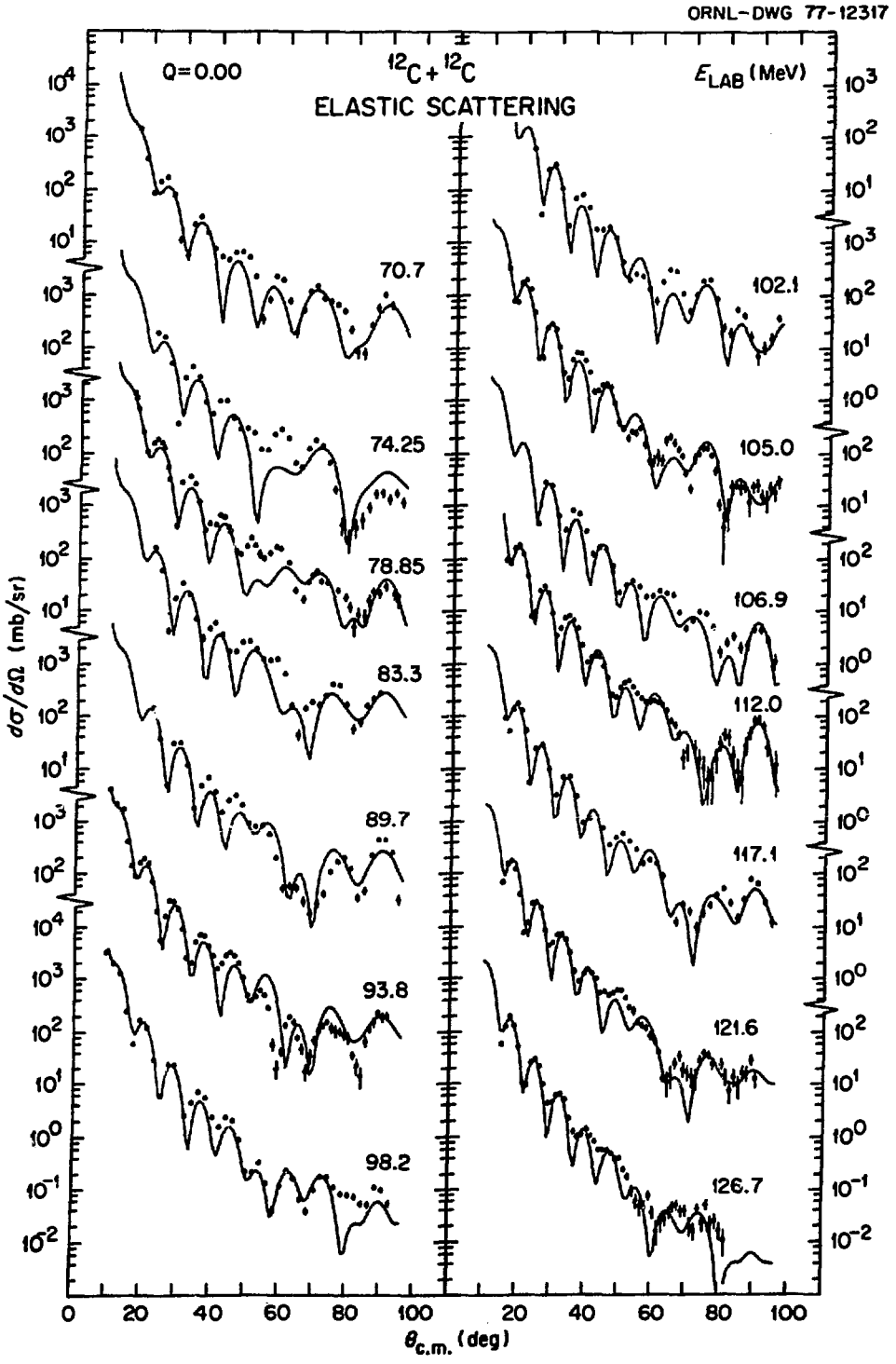
ORNL-DWG 77-12317
Q=0.00
$^{12}C + ^{12}C$
ELASTIC SCATTERING
E_{LAB} (MeV)
70.7
74.25
78.85
83.3
89.7
93.8
98.2
102.1
105.0
106.9
112.0
117.1
121.6
126.7
$d\sigma/d\Omega$ (mb/sr)
$\theta_{c.m.}$ (deg)

Fig. 14

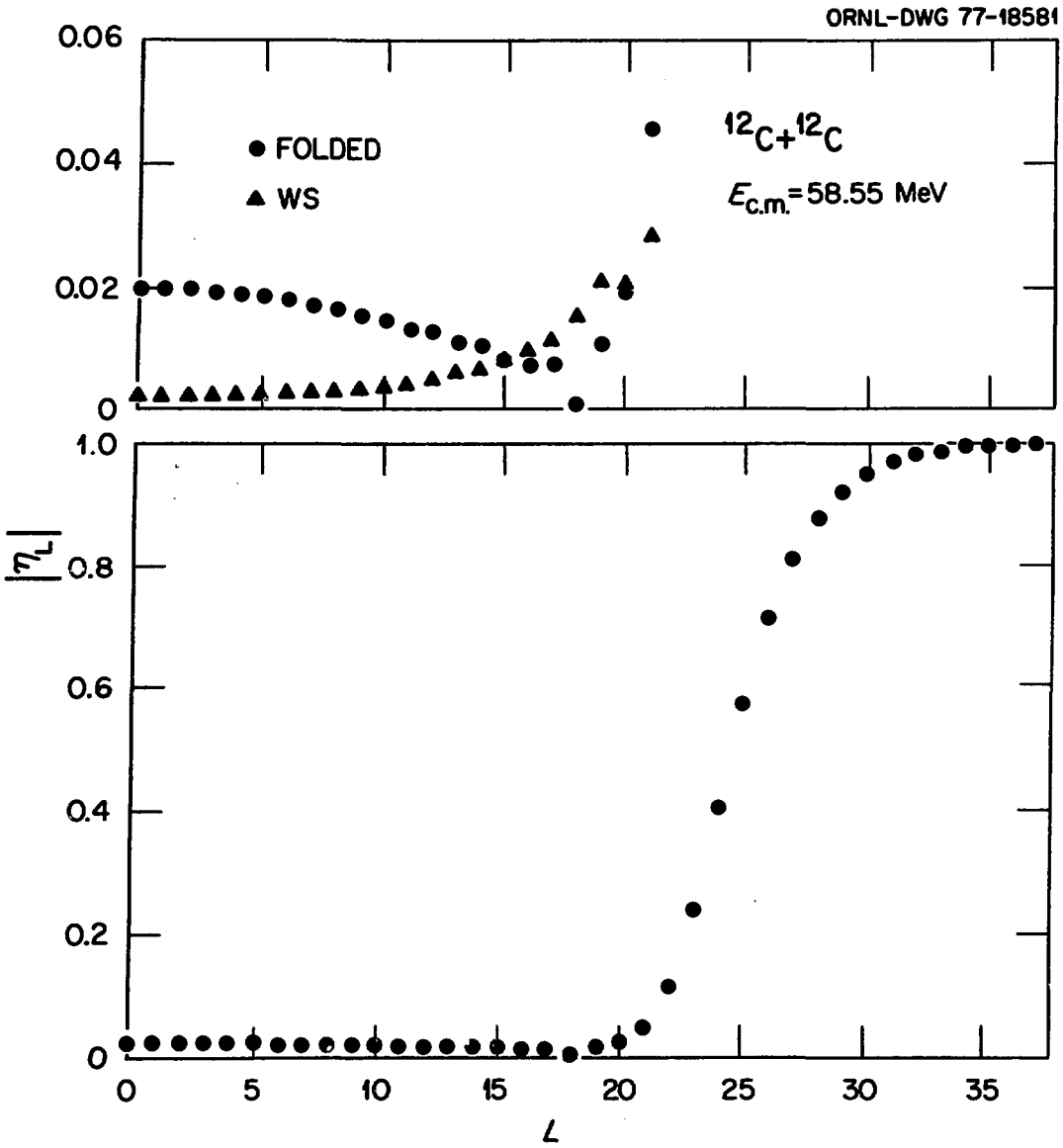
ORNL-DWG 77-18581
0.06
0.04
0.02
0
FOLDED
WS
$^{12}C+^{12}C$
$E_{c.m.}$=58.55 MeV
1.0
0.8
0.6
0.4
0.2
0
$|\eta_L|$
0
5
10
15
20
25
30
35
L

Fig. 15

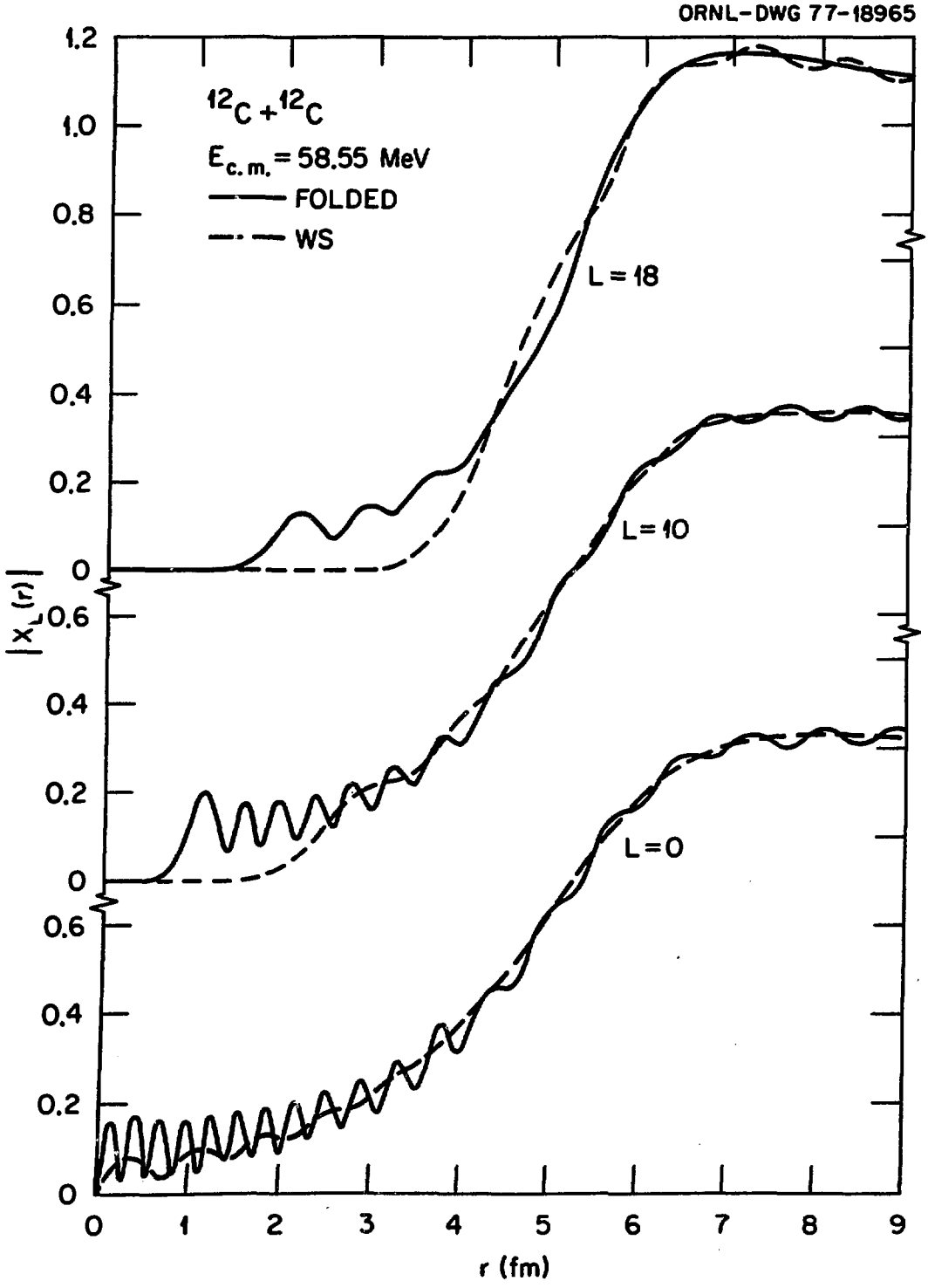
ORNL-DWG 77-18965
$^{12}C + ^{12}C$
$E_{c.m.} = 58.55$ MeV
FOLDED
WS
L = 18
L = 10
L = 0
$|\chi_L(r)|$
r (fm)
1.2
1.0
0.8
0.6
0.4
0.2
0
0
1
2
3
4
5
6
7
8
9

Fig. 16

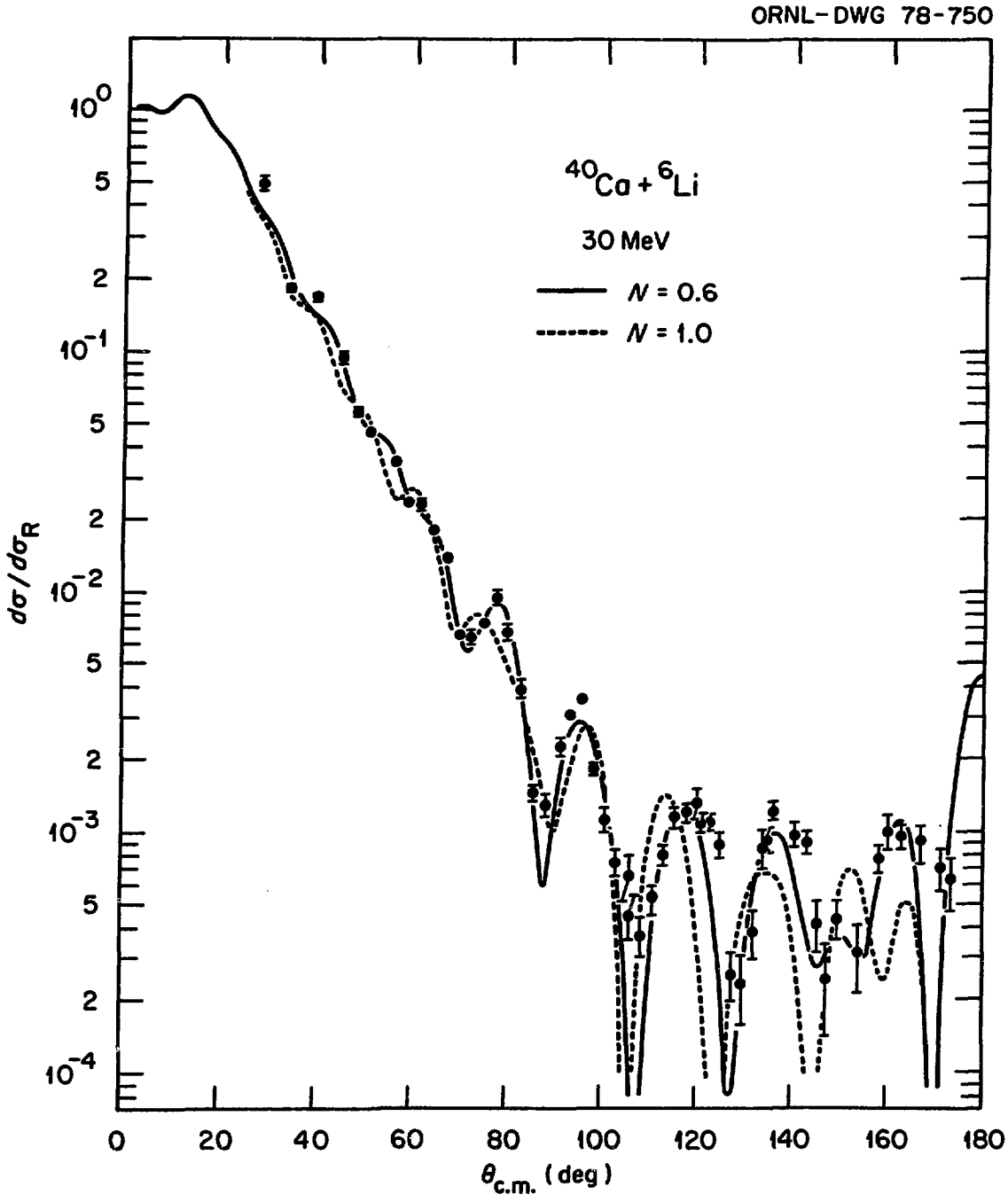
ORNL-DWG 78-750
$^{40}Ca + ^{6}Li$
30 MeV
N = 0.6
N = 1.0
$d\sigma/d\sigma_R$
$\theta_{c.m.}$ (deg)
10^0
5
2
10^{-1}
5
2
10^{-2}
5
2
10^{-3}
5
2
10^{-4}
0
20
40
60
80
100
120
140
160
180

Fig. 17

ORNL-DWG 78-17473

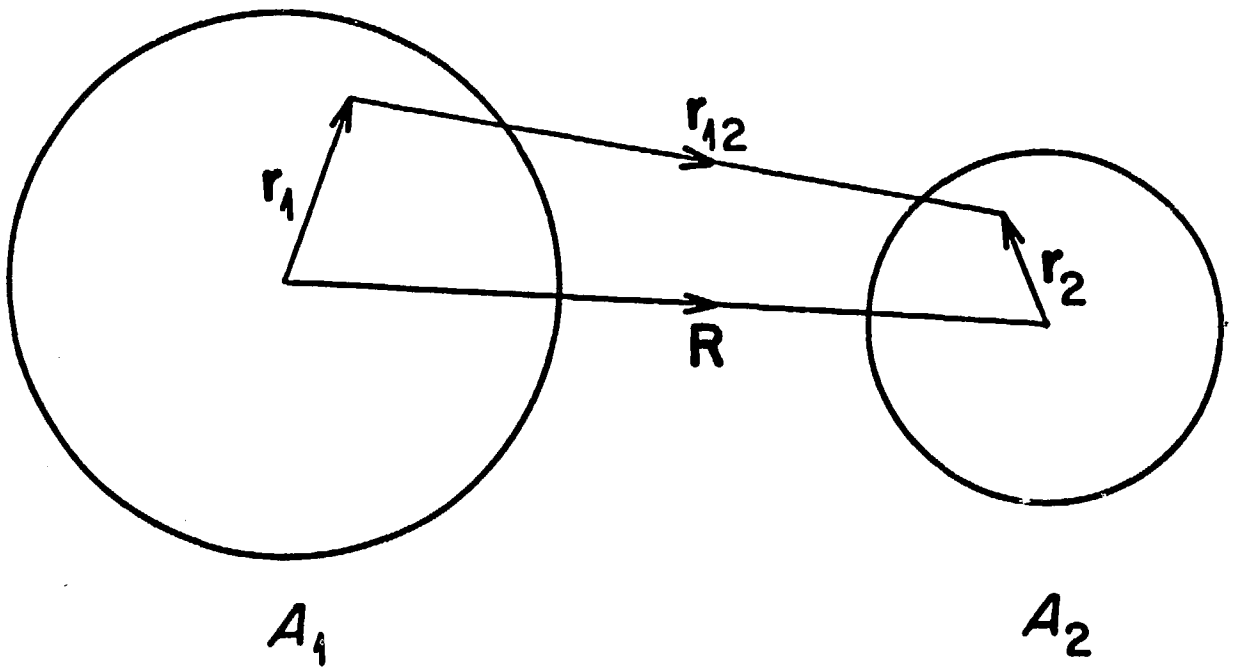

Fig. 18

ORNL-DWG 78-17474

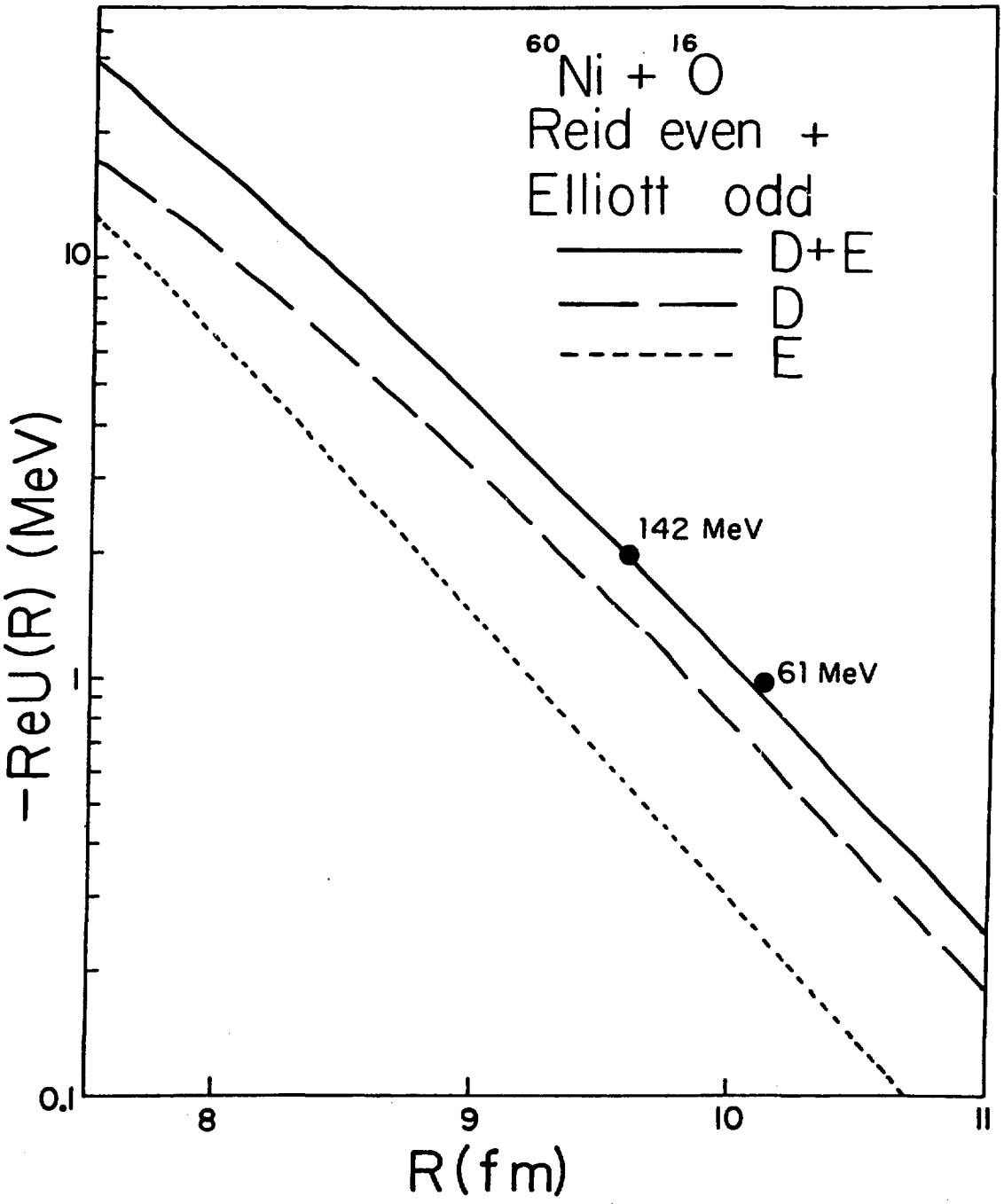

Fig. 19a

ORNL-DWG 78-17475

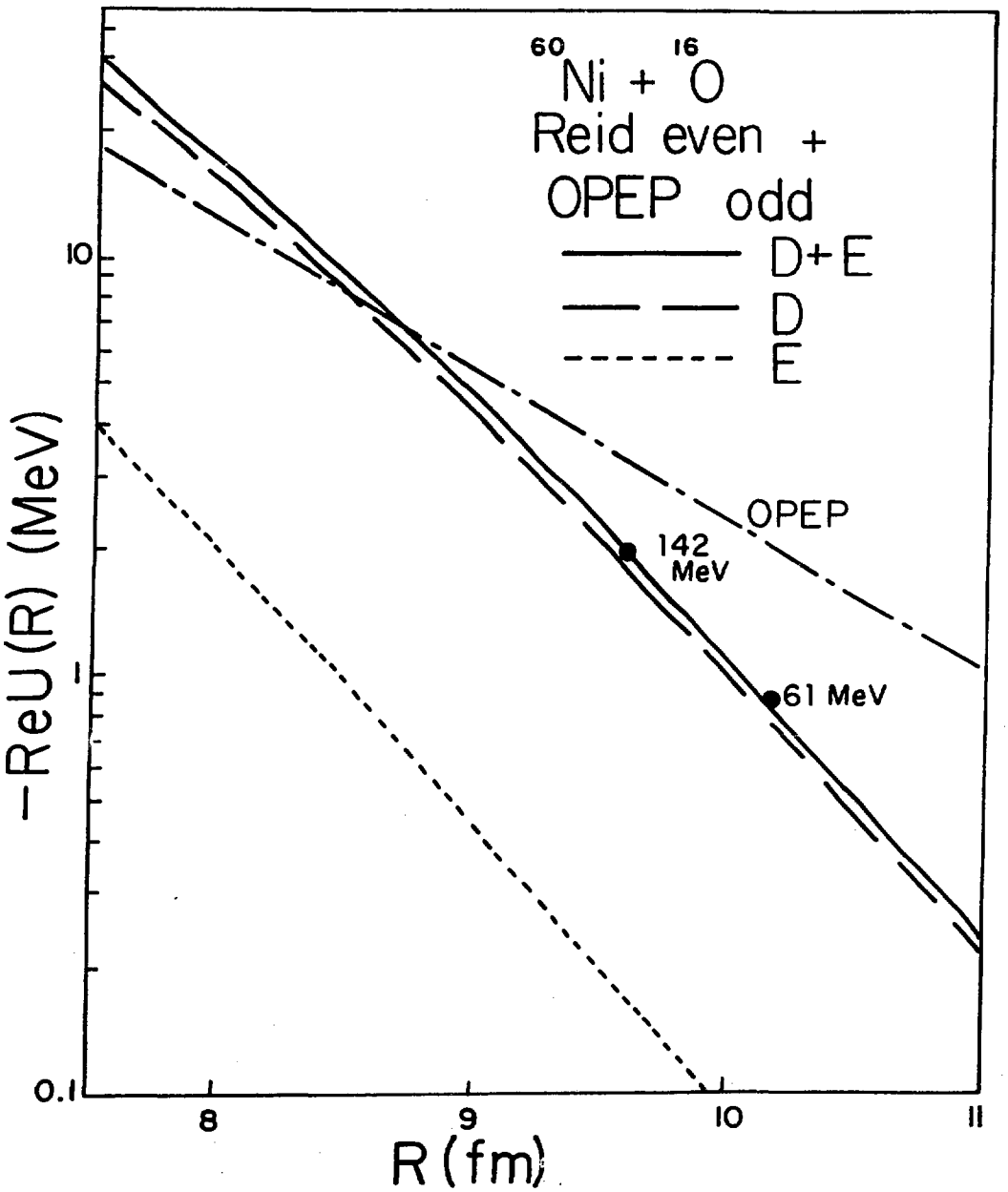

Fig. 19b

ORNL-DWG 78-17476

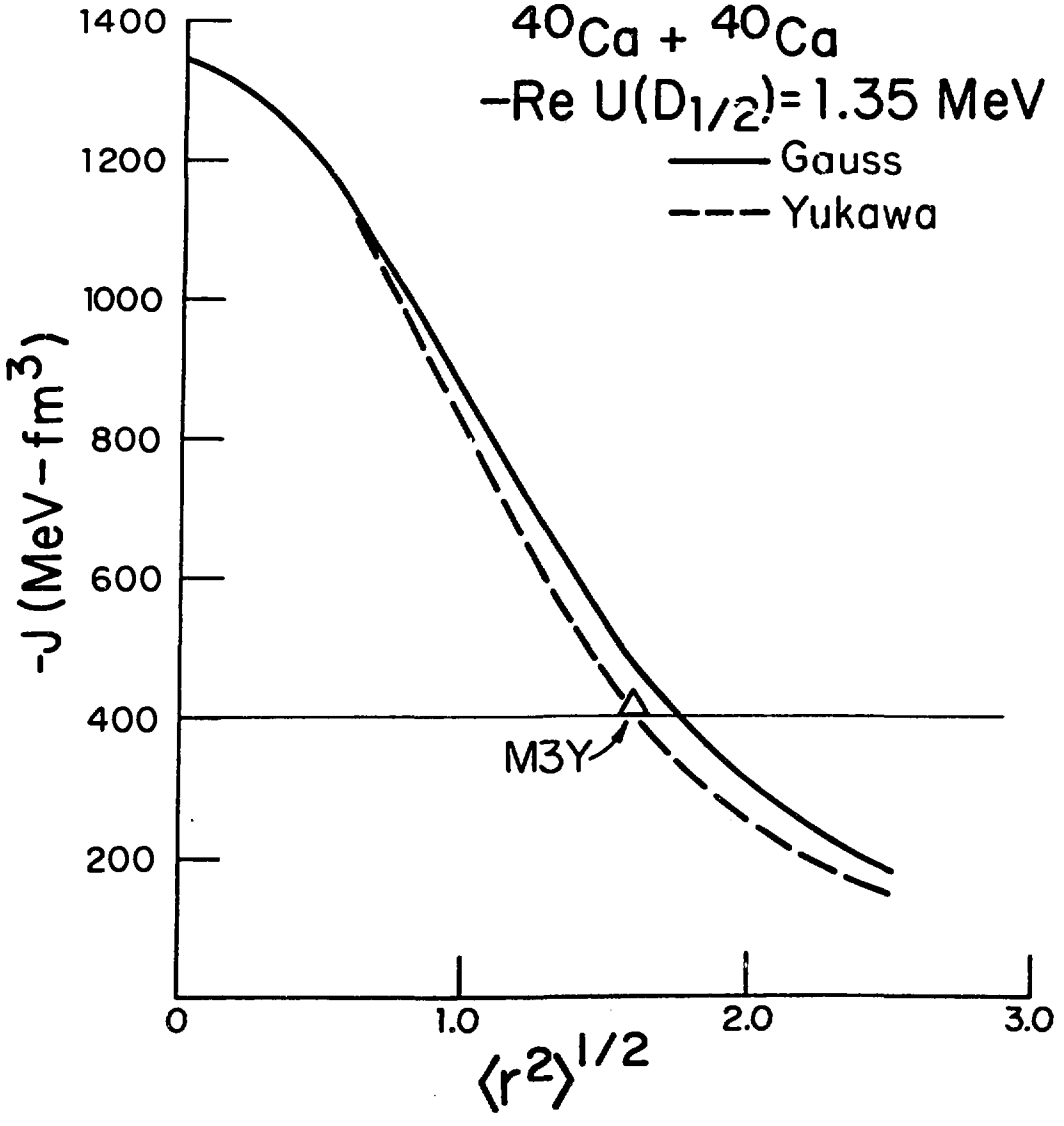

Fig. 20

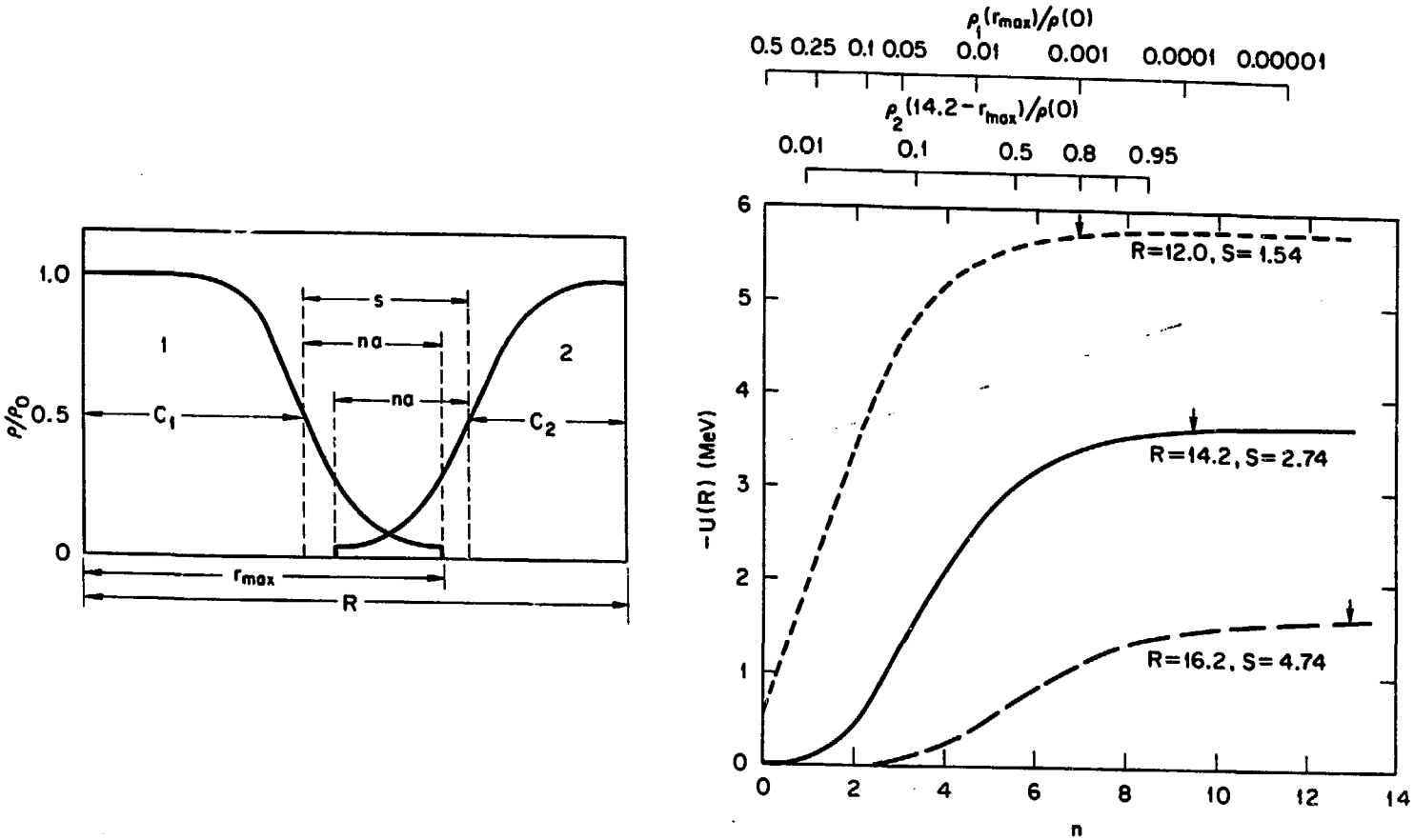
1.0
0.5
0
ρ/ρ0
1
2
C1
C2
s
na
na
rmax
R
ρ1(rmax)/ρ(0)
0.5 0.25 0.1 0.05 0.01 0.001 0.0001 0.00001
ρ2(14.2−rmax)/ρ(0)
0.01 0.1 0.5 0.8 0.95
R=12.0, S=1.54
R=14.2, S=2.74
R=16.2, S=4.74
-U(R) (MeV)
n
0 2 4 6 8 10 12 14
0 1 2 3 4 5 6

Fig. 21

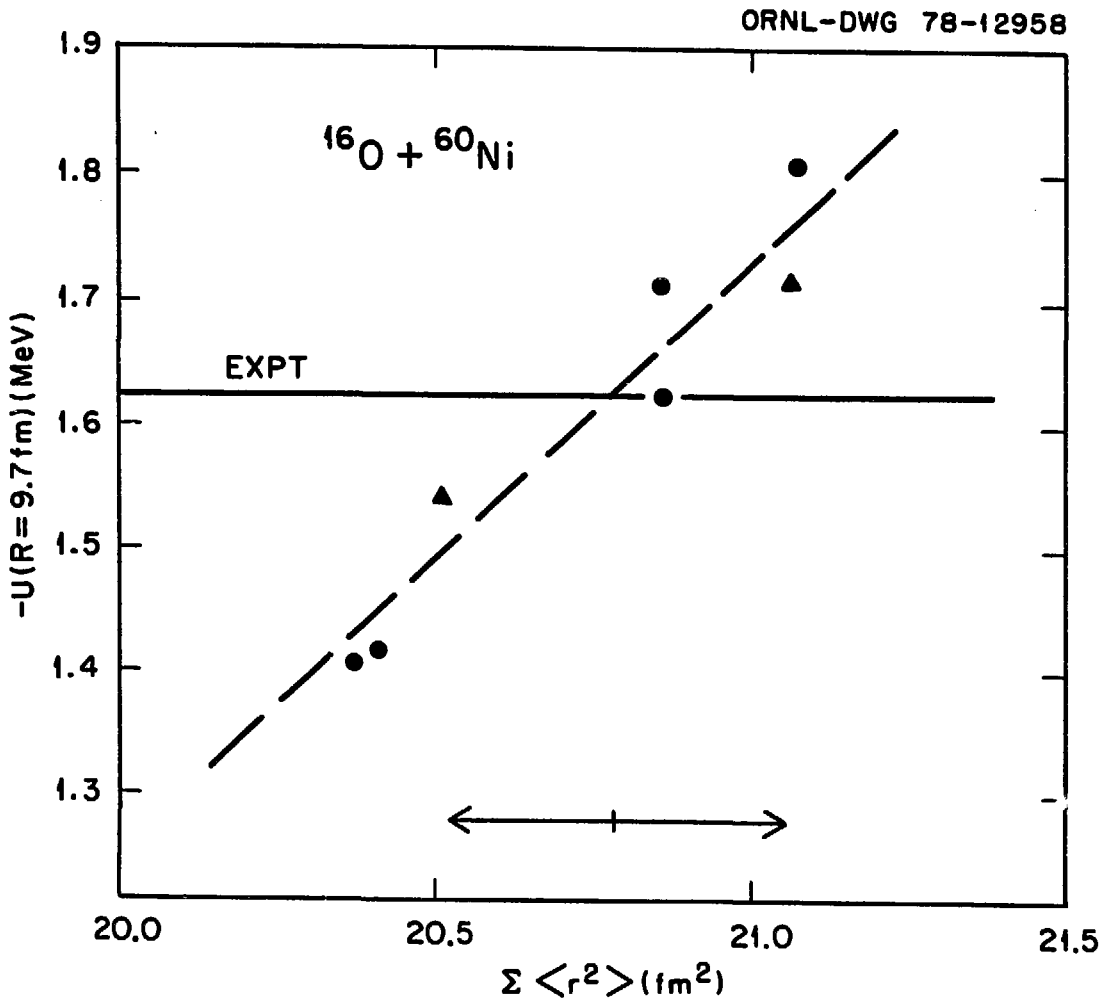
ORNL-DWG 78-12958
$^{16}O + ^{60}Ni$
EXPT
-U(R=9.7fm)(MeV)
1.9
1.8
1.7
1.6
1.5
1.4
1.3
20.0
20.5
21.0
21.5
$\Sigma \langle r^2 \rangle (fm^2)$

Fig. 22

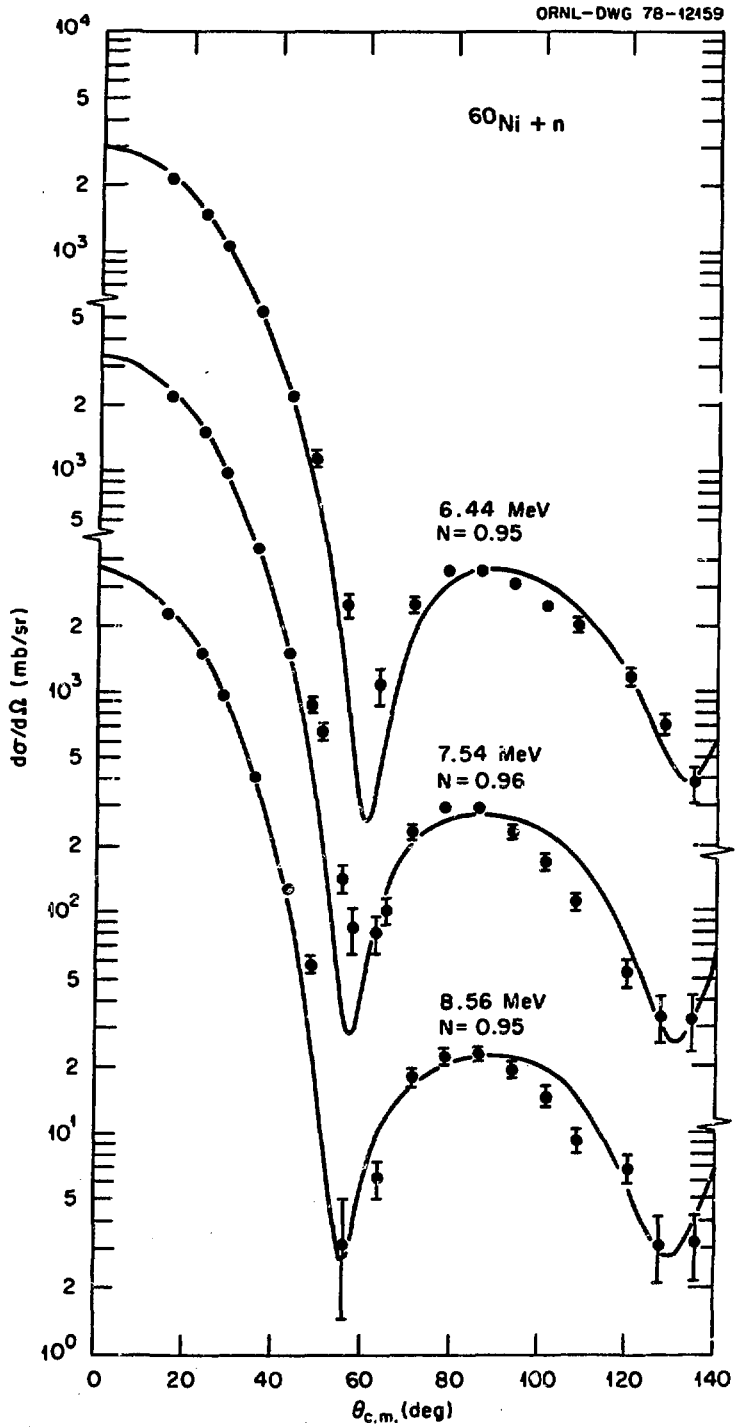
ORNL-DWG 78-12159
^{60}Ni + n
6.44 MeV
N = 0.95
7.54 MeV
N = 0.96
8.56 MeV
N = 0.95
dσ/dΩ (mb/sr)
θc.m. (deg)

Fig. 23a

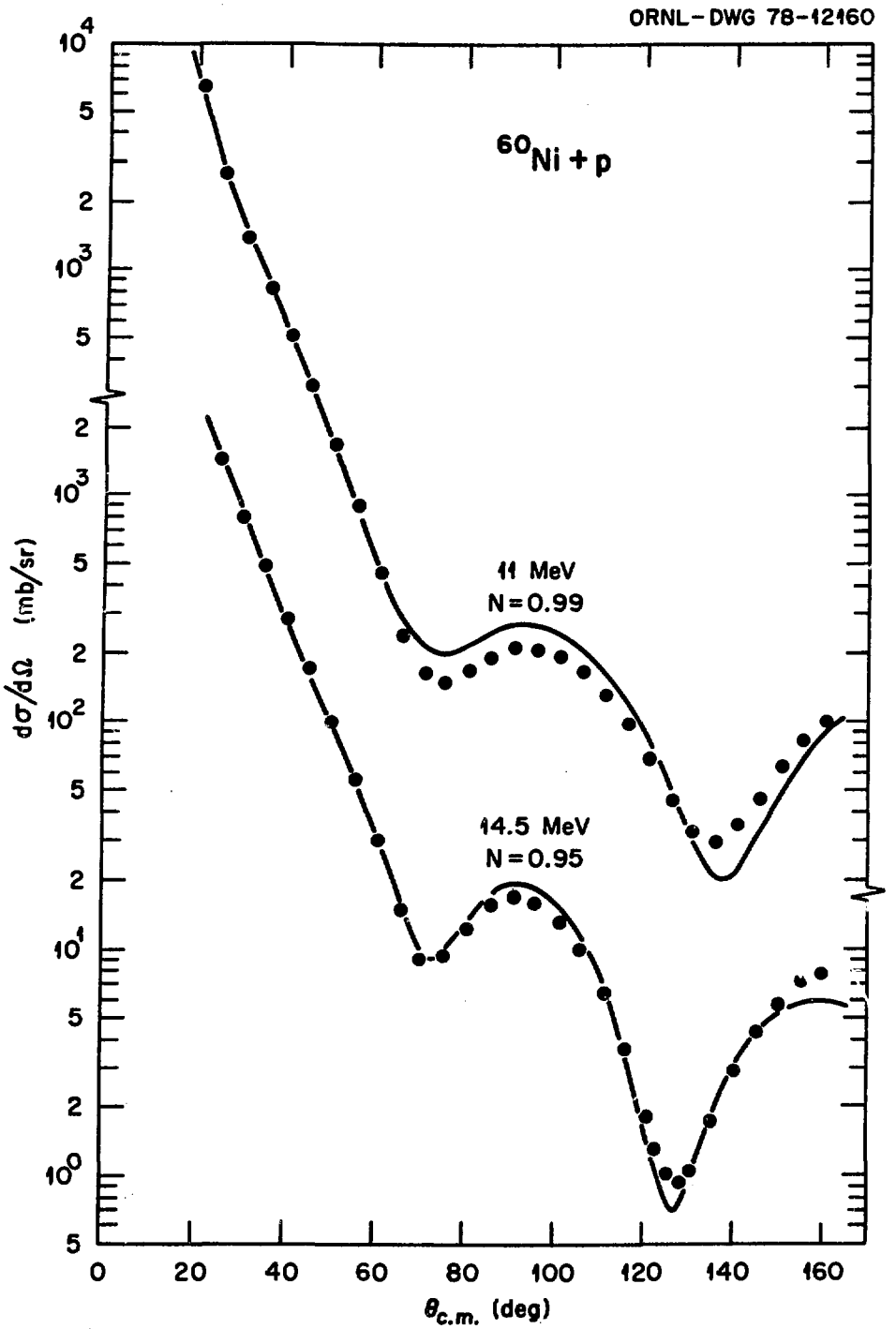
ORNL-DWG 78-12160
^{60}Ni + p
11 MeV
N=0.99
14.5 MeV
N=0.95
dσ/dΩ (mb/sr)
θc.m. (deg)

Fig. 23b

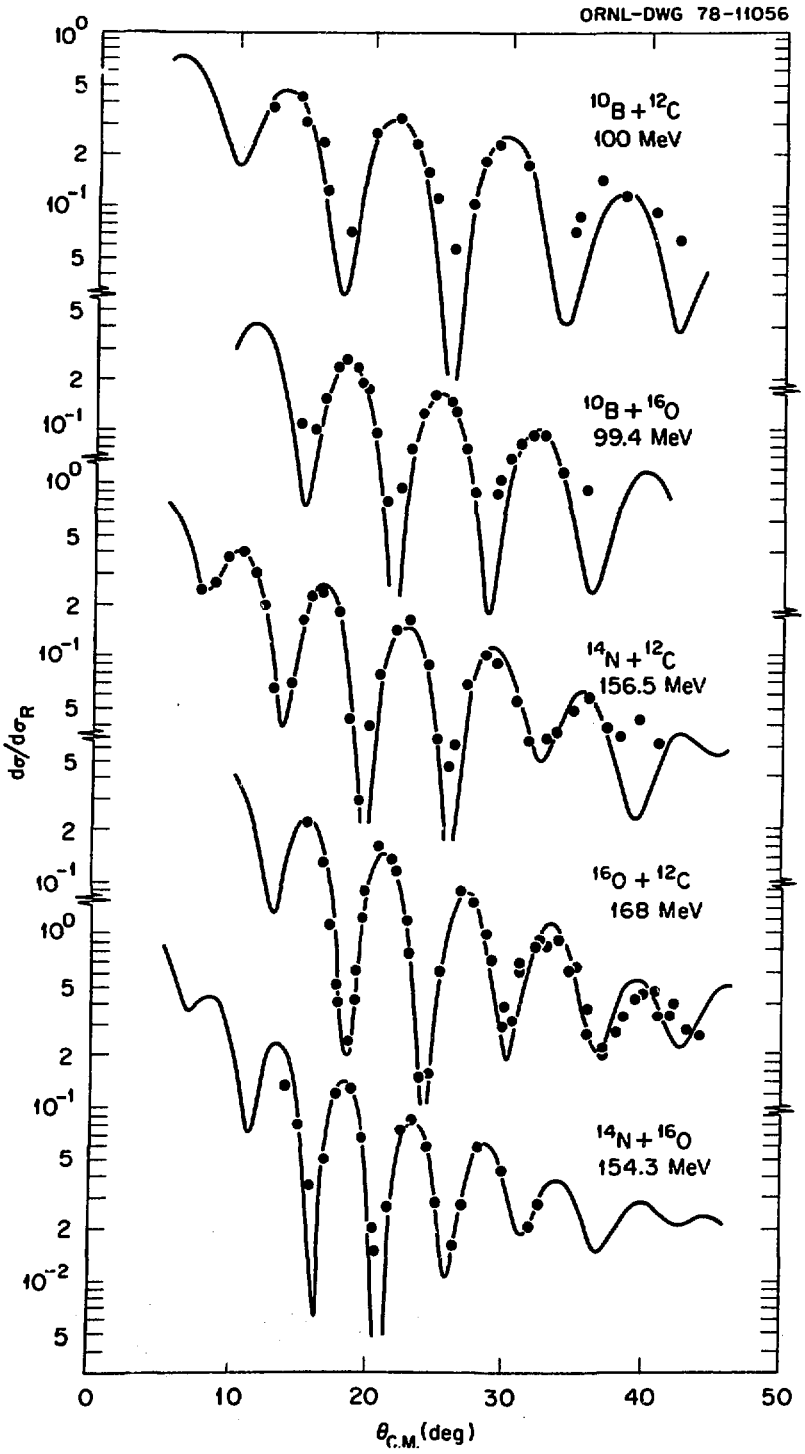
ORNL-DWG 78-11056
$^{10}B + ^{12}C$
100 MeV
$^{10}B + ^{16}O$
99.4 MeV
$^{14}N + ^{12}C$
156.5 MeV
$^{16}O + ^{12}C$
168 MeV
$^{14}N + ^{16}O$
154.3 MeV
$d\sigma/d\sigma_R$
$\theta_{C.M.}$ (deg)

Fig. 24

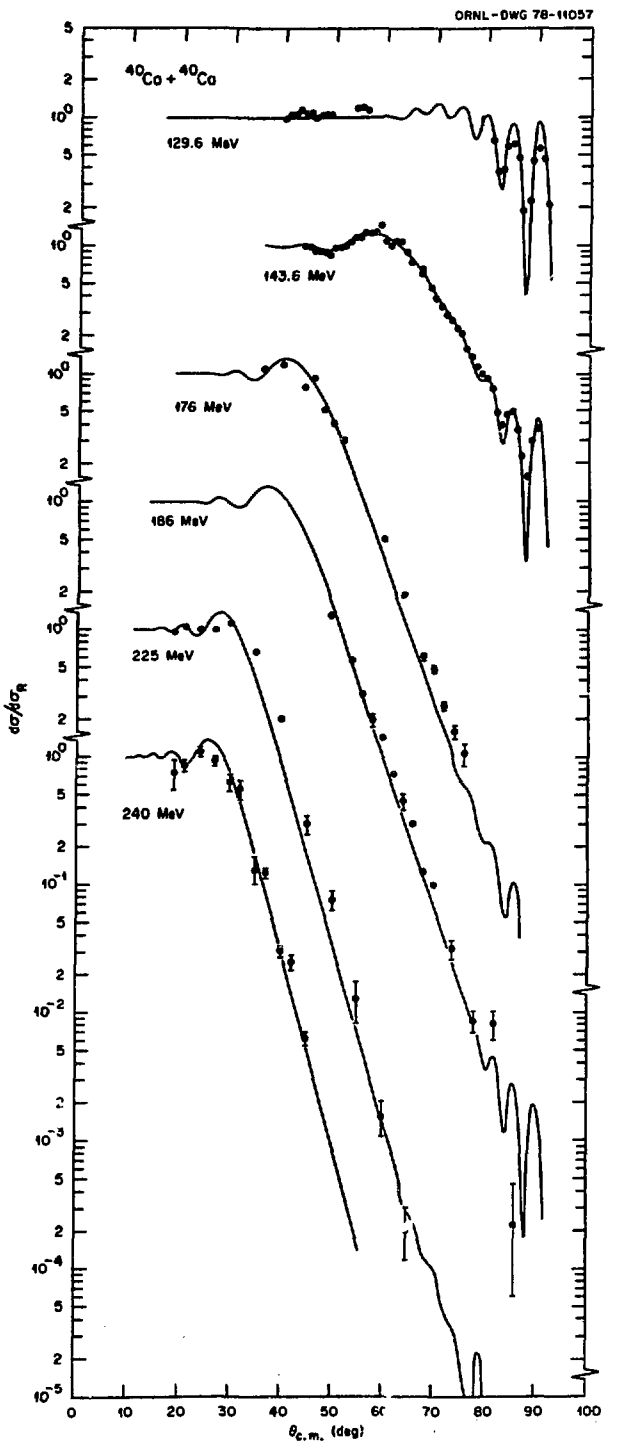
ORNL-DWG 78-11057
$^{40}Ca + ^{40}Ca$
129.6 MeV
143.6 MeV
176 MeV
186 MeV
225 MeV
240 MeV
$d\sigma/d\sigma_R$
$\theta_{c.m.}$ (deg)

Fig. 25

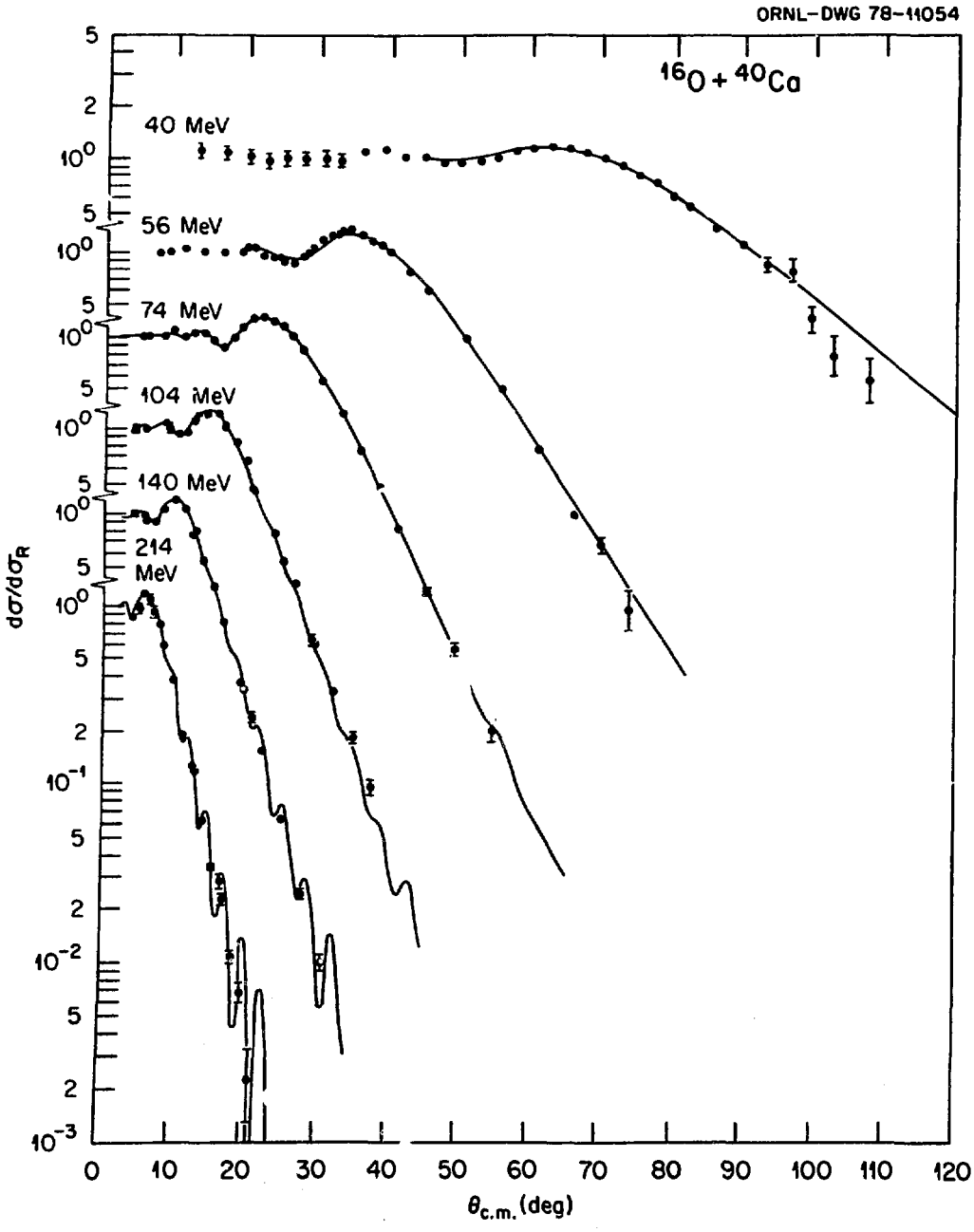
ORNL-DWG 78-11054
$^{16}O + ^{40}Ca$
40 MeV
56 MeV
74 MeV
104 MeV
140 MeV
214 MeV
$d\sigma/d\sigma_R$
$\theta_{c.m.}$(deg)

Fig. 26